INSTITUT FÜR KERNPHYSIK

Master-Thesis

Automated Test Stand Setup and Signal Reconstruction for the CBM-TRD

Johannes Beckhoff

First Supervisor: Prof. Dr. Anton Andronic
Second Supervisor: PD Dr. Christian Klein-Bösing

— August 2018 —

Contents

Introduction

Since the beginning of mankind people feel the need to explore the smallest structures of the universe. In many fields the particle physics tries to find answers to those questions. In order to explain the behavior of the ingredients of matter, the Quantum ChromoDynamics (QCD) describes the theory of the strong interaction of quarks and gluons. At normal temperatures the quarks are confined in composite states (hadrons) whereas at higher temperatures or densities this confinement does not longer apply and the quarks and gluons interact as quasi-free particles. While the QCD itself is well understood, the behavior of strongly interacting particles at these conditions is still under investigations.
The Compressed Baryonic Matter (CBM) experiment at FAIR (Facility for Antiproton and Ion Research) is designed to probe matter at high baryon densities with heavy-ion interaction rates up to 10 MHz. Such a high interaction rate allows the observation of properties of rare probes like multi-strange hyperons or charmed particles. The CBM experiment is a fixed target experiment consisting of seven individual detectors including a Transition Radiation Detector (TRD) in favor of e.g. electron or hardron identification. Due to the high interaction rate the Multi-Wire Proportional Chambers (MWPC) of the TRD face particle rates up to 120 $\mathrm{kHz\,cm^{-2}}$ and hence require high rate capability of the readout electronics.
The detector development, including the MWPC, the electronic readout chain as well as the firmware, is almost completed since the final concepts are already designed and only the last details have to be fixed. Hence, the existing setup has to be tested regarding its functionality and performance. Furthermore, ensuring reliable measurements in the final experiment setup requires extensive tests in advance. Therefore, an automated test stand was constructed within the framework of this work.
Even though the front-end electronics already select single measured events and digitizes them, additional event reconstruction mechanisms are necessary to fully determine the physical properties of a measured particle, e.g. the charge and location. Right now this takes place in a yet not completely implemented offline analysis software. Determining a particle's charge requires a calibration of the whole system and thus an energy spectrum to obtain information about the gas gain of the MWPC. Furthermore, the signal reconstruction of events, where several particles hit the same detector region at the same time (multihits), is not realized yet and will be investigated later in this thesis.

1. Theoretical Background

The CBM-TRD is a Multi Wire Proportional Chamber (MWPC) which detects ionizing radiation.
Hence, the interaction of particles with the detector gas as well as gas characteristics and gas amplification mechanisms are described in this chapter.

1.1. Interactions of Photons with Matter

Mainly three different mechanisms occur when photons interact with matter: the photoelectrical effect, dominant at photon energies up to 0.5 MeV, the Compton effect, mainly appearing from 0.5 MeV to 5.0 MeV and the pair production dominating at higher energies.

- The photoelectrical effect describes the absorption of a photon by an electron:

$$\gamma + A \rightarrow A^+ + e^-. \tag{1.1}$$

  The energy of the photon, which is completely transferred to the electron, has to be at least as high as the electron binding energy.

- Compton scattering is the scattering of a photon on an electron from an outer atomic shell, releasing the electron from the atom:

$$\gamma + A \rightarrow A^+ + e^- + \gamma'. \tag{1.2}$$

  Taking energy and momentum conversation into account, the electron energy after the process is a continuous function of the scattering angel ϑ:

$$E_e = \hbar\omega \frac{\frac{\hbar\omega}{m_e c^2}(1 - \cos\vartheta)}{1 + \frac{\hbar\omega}{m_e c^2}(1 - \cos\vartheta)}. \tag{1.3}$$

- With a photon energy greater than twice the electron rest energy ($\hbar\omega \geq 2m_e c^2 = 1.022\,\text{MeV}$), the photon can be annihilated under the creation of a particle-antiparticle pair (e^--e^+-pair). For this process, a third particle, in general a nucleus receiving some of the momentum, is needed to fulfill the momentum conversation.

In the photoelectrical and Compton effect an electron is released from an atom leaving an unoccupied state which is filled by another more slightly bounded electron. This transition can cause the radiation of characteristic X-rays, called K_α, L_β etc. where the capital letter describes the atomic shell of the primarily released electron, while the index specifys the difference of the atomic shells of the two electrons. These X-rays have element specific energies of the difference of the two electron binding energies.
In another scenario the released energy of the electron transition can knock a third electron out of the shell (Auger electron) with the energy
$E_{Auger} = E_{hole} - E_{B1} - E_{B2}$. E_{hole} depicts the energy of the resulting unoccupied state and $E_{B1/2}$ the binding energies of the two initial electrons. [Wes15]

1.2. Interactions of Charged Particles

In contrast to photons, charged particles do not interact at one single point but continuously with matter most likely via interactions with electrons in atomic shells. Thus, it is useful to describe the mean energy loss per path, dependent on the medium properties and the velocity of the particle.
If a heavy particle with the mass $M \gg m_e$, the charge $Z \cdot e$ and the velocity v passes a free bounded and resting shell electron in a medium, the particle can be assumed to just drift a little from its track. A following derivation leads to Bohr's classical formula describing the energy loss, enhanced by Bethe and Bloch to the Bethe-Bloch formula taking quantum mechanical effects into account:

$$-\frac{\mathrm{d}E}{\mathrm{d}x} = 2\pi N_A r_e^2 m_e c^2 \rho \frac{Z}{A}\frac{z^2}{\beta^2}\left[\ln\left(\frac{2m_e c^2 v^2 \gamma^2 \Delta T_{max}}{I^2}\right) - 2\beta^2 - \delta - 2\frac{C}{Z}\right] \quad (1.4)$$

with the parameters

- N_A: Avogadro number
- r_e: classical electron radius; m_e: electron mass
- Z, A, ρ: atomic number, mass number and density of the medium
- z, v: charge number and velocity of the passing particle with $\beta = v/c$ and $\gamma^2 = 1 - \beta^2$
- $I \approx 16 \cdot Z^{0.9}$ eV: effective ionization potential of the atoms of the medium
- ΔT_{max}: maximum energy transfer to an electron in a central collision
- δ: density correction at high energies
  C: shell correction at low energies.

The energy loss of heavy charged particles is dominated by ionization processes, whereas electromagnetic radiation (bremsstrahlung) is another important effect in the case of electrons and positrons because of their small mass. The overall stopping power of a particle can be written as

$$\left(\frac{\mathrm{d}E}{\mathrm{d}x}\right)_{total} = \left(\frac{\mathrm{d}E}{\mathrm{d}x}\right)_{ion} + \left(\frac{\mathrm{d}E}{\mathrm{d}x}\right)_{rad} . \tag{1.5}$$

As pictured in figure 1.1, the ionization process captures the major amount of the energy loss up to an electron energy of a few MeV and is dominated by the bremsstrahlung loss above a critical energy.

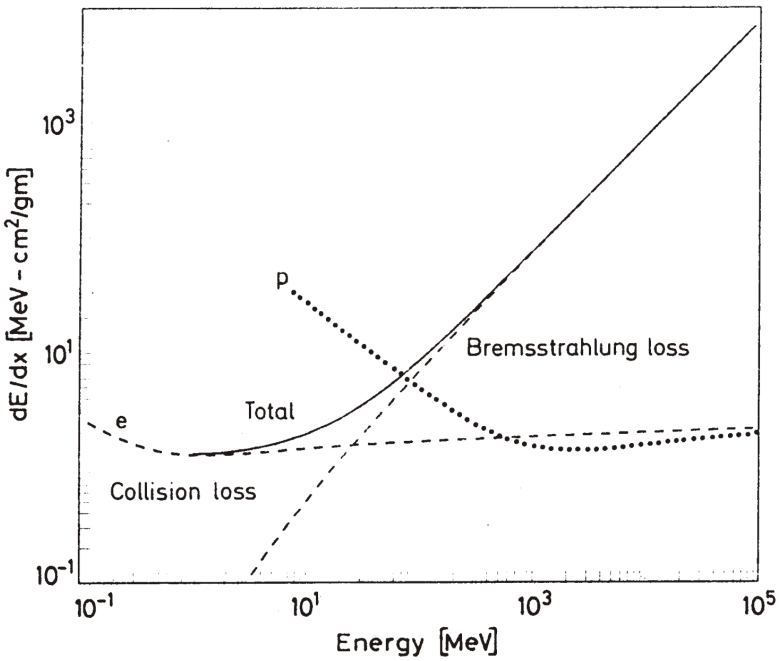

Figure 1.1.: This diagram shows the total energy loss $\mathrm{d}E/\mathrm{d}x$ of an electron in matter in dependence of its energy. In addition, the energy losses due to two different processes, collisions with other atoms and bremsstrahlung, are shown. [zN06]

Ionization Process

In order to calculate the energy loss caused by ionization, the same assumption as for the Bethe-Bloch formula can be made with two exceptions. Due to the small electron mass, the traversing particle does not stay on its track but is deflected by the collisions. Furthermore, this case describes the interaction between two identical particles whose indistinguishability has to be considered in the calculation.

Bremsstrahlung

The interaction of the traversing electron with the nuclei Coulomb fields causes an acceleration of the electron leading to electromagnetic radiation, called bremsstrahlung. The corresponding energy loss can be written as

$$-\left(\frac{\mathrm{d}E}{\mathrm{d}x}\right)_{rad} = -\frac{E_0}{x_0} \tag{1.6}$$

with the initial electron energy E_0 and the medium dependent radiation length x_0, after which the electron energy decreases to E_0/e.
x_0 can approximately be expressed as

$$\frac{1}{x_0} = 4\alpha r_e^2 Z(Z+1)\frac{N_A\rho}{A}\ln\left(\frac{183}{Z^{1/3}}\right).$$

The two explained processes have different dependencies on the particle energy and the atomic number:

$$\text{Ionization} \sim Z \cdot \ln E$$
$$\text{Bremsstrahlung} \sim Z^2 \cdot E.$$

Thus, a critical energy $E_c \approx 600\,\mathrm{MeV}/Z$ (102 MeV for air) exists at which the the two energy losses are equal. [zN06]

Minimum Ionizing Particles

Figure 1.2 pictures the stopping power in dependence of a positive muons' energy in copper. A minimum of the energy loss in the Bethe-Bloch region, where the particle loses most of its energy due to inelastic scattering with electrons, is visible. This minimum describes the minimal energy deposit a charged particle can lose in a medium. Such particles are called minimum ionizing particles (MIP). [zN06]

1.3. Radioactive Decays

The decay of a radioactive nucleus is a statistical event and not predictable for a single atom. However, the number of many nuclei at a time t has the exponential decrease

$$N(t) = N_0 \cdot \mathrm{e}^{-t/\tau} \tag{1.7}$$

with the initial number of nuclei N_0 and the mean lifetime τ. After the half-life $t_{1/2} = \ln 2 \cdot \tau$, the number of nuclei halves themselves. The most important kind of decays of radioactive isotopes are the α, β and γ decays.

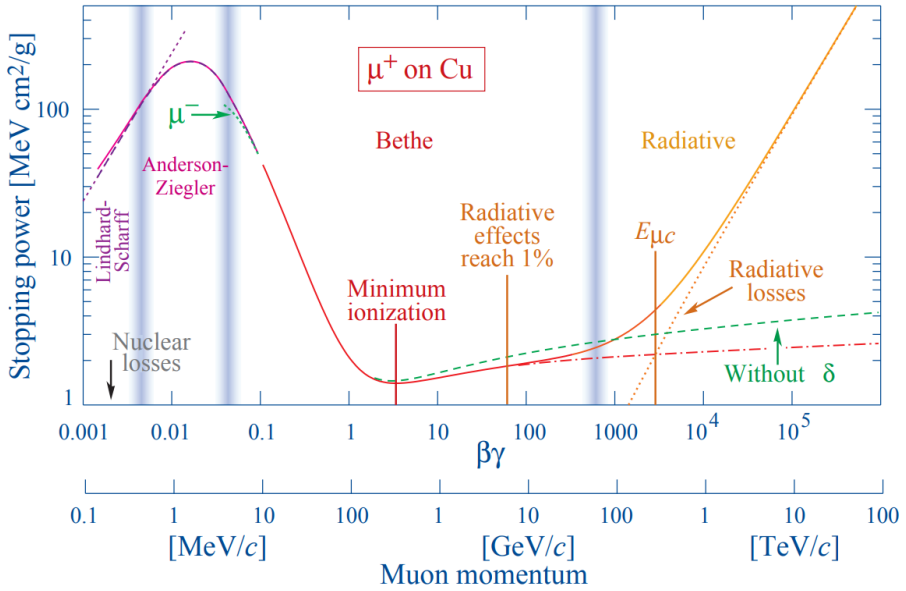

Figure 1.2.: This plot presents the stopping power $\mathrm{d}E/\mathrm{d}x$ (solid curve) of a μ^+ in copper in dependence of the particle momentum. The grey vertical lines indicate regions where different types of processes have a dominant contribution to the energy loss. A minimum is reached within the Bethe-Bloch region. This minimum depicts the point of minimum ionization, at which the particle loses the minimal energy in the medium. [eaP13]

α Decay

By emitting an α particle with two protons and two neutrons the nucleus' mass number decrements by four and the atomic number by two:

$$ {}^{A}_{Z}\mathrm{X}_N \rightarrow {}^{A-4}_{Z-2}\mathrm{X}_{N-2} + {}^{4}_{2}\mathrm{He}_2. \tag{1.8} $$

With a decay energy of about 5.5 MeV the α particle should not be able to conquer the Coulomb wall $V \approx 30\,\mathrm{MeV}$ of the nucleus. Nevertheless, the α particle has a possibility to be emitted due to quantum mechanical tunnel effects.

β Decay

The β decay describes the conversion of a nucleus into an isotope of a neighboring element. This process can take place in different ways by a neutron decaying into a proton under the emission of an electron, a proton decaying into a neutron under the emission of a positron or by a proton capturing a shell electron and decaying into a neutron. In those scenarios, all three decays would violate the momentum conversation. This is the reason, why the emission of a third particle, the electron neutrino ν_e or the electron anti neutrino $\bar{\nu}_e$ is required:

1. β^- decay

$$\begin{aligned} & n \rightarrow p + e^- + \bar{\nu}_e \\ \text{energy}: \quad & Q(\beta^-) = B(Z+1, A) - B(Z, A) + \underbrace{(m_n - m_p - m_{e^-})c^2}_{+0.78\,\mathrm{MeV/c^2}} \end{aligned} \tag{1.9}$$

2. β^+ decay

$$\begin{aligned} & p \rightarrow n + e^+ + \nu_e \\ \text{energy}: \quad & Q(\beta^+) = B(Z-1, A) - B(Z, A) + \underbrace{(m_p - m_n - m_{e^+})c^2}_{-1.8\,\mathrm{MeV/c^2}} \end{aligned} \tag{1.10}$$

3. electron capture (EC)

$$\begin{aligned} & p + e^- \rightarrow n + \nu_e \\ \text{energy}: \quad & Q(EC) = B(Z-1, A) - B(Z, A) + \underbrace{(m_p + m_{e^-} - m_n)c^2}_{-0.78\,\mathrm{MeV/c^2}} \end{aligned} \tag{1.11}$$

The respective energy balance of the decays is specified by the Bethe-Weizsäcker equation. Based on this, the β^- decay appears to be the only one occurring without any energy supply while the other two decays require additional energy.

Electromagnetic Transitions

The α and β decay leave the nucleus in an excited state releasing energy by returning into the ground state which can cause the emission of a photon or a conversion electron in the shell. In the latter case an unpopulated state remains in the atomic shell which is then occupied by another electron resulting in the emission of characteristic X-rays or Auger electrons as explained in chapter 1.1. Furthermore, exceeding $2m_e$, the excitation energy can also be converted into an electron positron pair which is emitted out of the nucleus. [Wes15]

1.4. Working Principle of a MWPC

A MWPC enlarges the principal of a proportional counter onto a larger area enabling spatially and energetically resolved measurements.

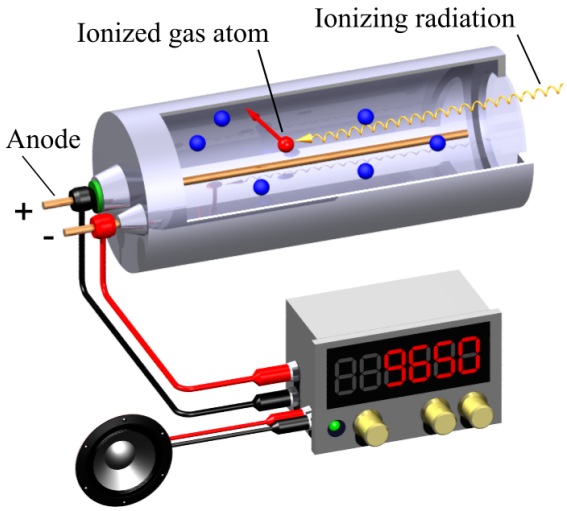

Figure 1.3.: This figure shows the scheme of an ionization chamber. A high voltage is applied on a cylindrical tube with a wire in its middle. The tube is filled with an inert gas, so ionizing radiation can ionize the gas atom. The arising free electrons move towards the anode wire creating an electrical current pulse which can be measured. [Svj15]

Proportional Counter

A proportional counter can be realized by filling a cylindrical metallic tube with a wire in the axis of the cylinder, containing an inert gas like neon, xenon or argon (see figure 1.3). By applying a high voltage on the tube, the outer cylinder acts as a cathode and the wire as an anode. If a particle enters the tube via an entrance window, it ionizes the gas causing an acceleration of the gas atoms towards the cathode and an acceleration of the electrons towards the anode. Arriving at the anode wire, the electrons produce an electric current pulse which for example can be measured via a resistor. If the applied voltage is high enough, the drifting electrons reach an area with a high electric field ($10^4 - 10^5\,\mathrm{V/cm}$) and gain so much energy between two collisions that they can ionize additional atoms on their way. Hence, the primary ionization electrons create an avalanche of secondary electrons resulting in a larger current pulse. The measured voltage can be written as

$$\Delta U = -G\frac{Ne}{C} \tag{1.12}$$

where N is the number of primary electrons, e the electron charge, C the anode capacity and G the gas gain factor. The functionality of an ionization chamber depends on this gain factor and thus on the applied anode voltage U_A. Figure 1.4 shows the different detector regions with the proportional counting region, where the measured current pulse is proportional to the

primary ionization enabling energetically resolved measurements.
The operating gas of proportional counters is most likely an inert gas (e.g. argon, xenon) producing fast pulses because they can not produce any negative charged ions which move to the anode much slower than the electrons. Additionally, a quenching gas (e.g. CO_2) is filled into the detector to absorb photons which are created inside the detector. [zN06] [BRR08]

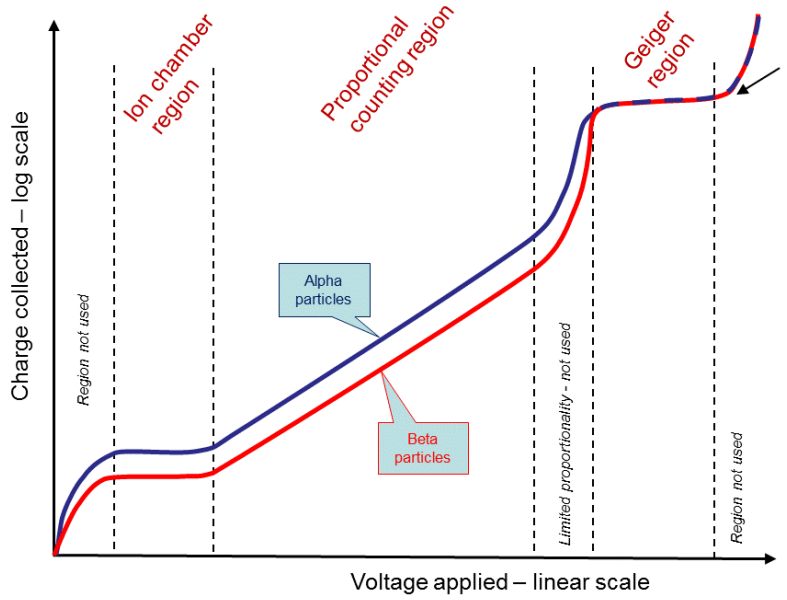

Figure 1.4.: The gas gain (collected charge by the anode wire) of an ionization chamber in dependence of the operating voltage reveals different regions: At very low voltages no signal can be measured due to the recombination of the created electron ion pairs. In the next region, the ion chamber region, the primary generated ions and electrons create an ionization current proportional to the incident particle energy without any gas amplification effects. Increasing the anode voltage (proportional counting region) leads to avalanche effects inside the gas resulting in a rise of the measured current which is still proportional to the particle energy. At even higher voltages the gas amplification saturates the whole inert gas (Geiger region). Thus, every particle ionizes the complete gas and creates the same electric current, so no statement about the measured energy can be made. α and β particles create different charges due to different ionizing effects, but show the same characteristics. [Sim12]

MWPC

Figure 1.5 illustrates a simplified principle of a MWPC with many anode wires arranged parallel between cathode planes. Just as in a proportional counter an incoming particle ionizes the gas producing electrons drifting towards the next anode wire. Due to a high electric field near the wires the drifting primary electrons create electron avalanches near the anode. With the individual readout of every anode wire the position of the particle can be distinguished. The lateral resolution can be improved up to some μm by segmenting the cathode plane into small pads directed orthogonal to the anode wires. The electrons at the anode induce a charge on these cathode pads which can be read out.

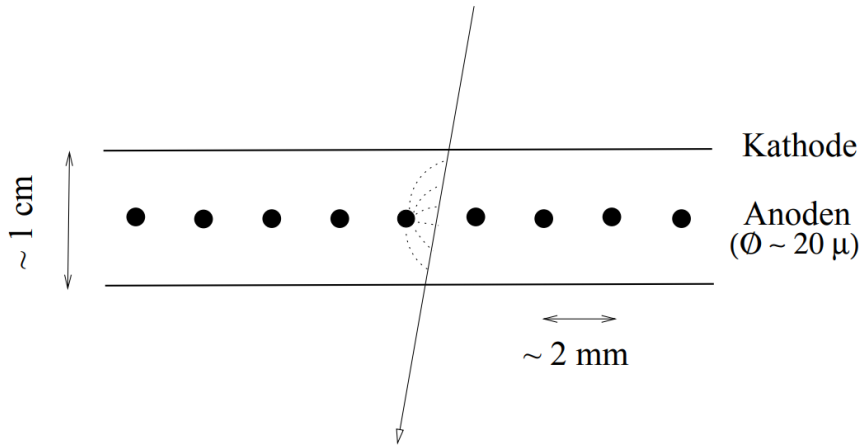

Figure 1.5.: This figure pictures a drawing of the working principle of a MWPC. Several anode wires are aligned parallel between two cathode planes. An incident particle ionizes the gas in the MWPC so the created electrons drift towards the nearest anode wire. An individual readout of every wire provides spatial resolved measurements. [zN06]

Escape Peaks MWPCs provide energetically and spatial resolved measurements. In addition to the energy spectrum of the measured source, other characteristics can appear in a measured spectrum including the escape peaks of the fill gas. These occur due to the ionization of an inner shell of the fill gas atoms by incoming particles. The remaining hole is filled by a higher shell electron leading to the emission of characteristic X-rays (see chapter 1.1) which are measured by the detector as well. [zN06]

2. Experimental Setup

This chapter explains both the construction of the test stand and the function of single components of the read out chain, which are important for later data analysis.

2.1. Automated Test Stand

Figure 2.1(a) pictures the front of the test stand including the beamtable with a MWPC (yellow) and the precision table mounted in front of it. 2.1(b) is a closer look from the side showing the source mounting element of the table with the ^{55}Fe source being directly installed in front of the MWPC.

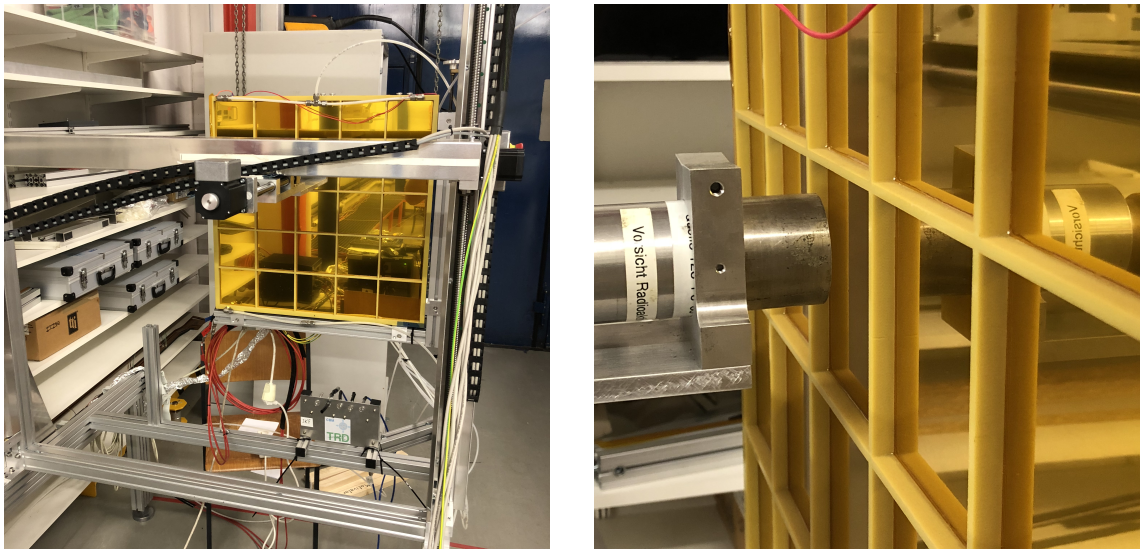

(a) (b)

Figure 2.1.: These two pictures show two views of the experimental setup of the test stand used for the measurements in this thesis. (a) pictures a front view of the precision table mounted in front of the MWPC (yellow). The side view in (b) shows the ^{55}Fe source mounted in front of the MWPC.

The precision table includes four stepper motors, controlled via a serial interface: two running synchronously in the x-axis whereas the other move the y- and z-axis. The control software was programmed as a part of this work using the Python module *pySerial*. Hence, the source can be moved freely across the MWPC by entering a total position into the graphical user interface or by selecting a default programmed pad pattern and moving the source to a selected pad. Furthermore, predefined motion patterns, such as the successive movement over several pads, can be realized.
The MWPC is operating with the Argon-CO_2 mixture Sagox (Ar/CO_2 82/18) with a gas flow of about $3\,l\,h^{-1}$ controlled via a flow regulator and measured by a flow meter. The oxygen concentration in the chamber is monitored by a gas analysis station designed by Felix Fidorra. Before conducting any measurements or applying a high voltage on the MWPC, the TRD chamber has to be flushed for a few days in order to decrease the oxygen concentration down to below 100 ppm. Both, the high voltages (anode and drift voltage) and the low voltages running the readout electronics, are regulated via a MPOD crate, which is also able to measure the overall anode current.

2.2. The CBM-TRD MWPC

Figure 2.2 shows an exposure view of the different layers of a CBM-TRD MWPC. An incoming particle enters the chamber from the right side via a Kapton foil entrance window. The inner part contains two wire planes, a cathode and an anode wire plane, and a segmented pad plane on the back.
Primary ionization electrons drift towards the cathode without any avalanche effects or considerable secondary ionizations and enter a much higher electric field in the amplification region afterwards. The detector dimensions of a 5.0 mm drift region and a 3.5 mm + 3.5 mm amplification region are pictured in figure 2.3. The drift voltage is about -500 V, whereas the anode voltage is in the order of 2000 V resulting in an overall drift field of 1 kV/cm and a field of ~ 2.8 kV/cm in the area around the anode wires where the major amplification takes place. The signal is measured via the induced charge on the pad plane by the charge around the anode wires. [Coled]

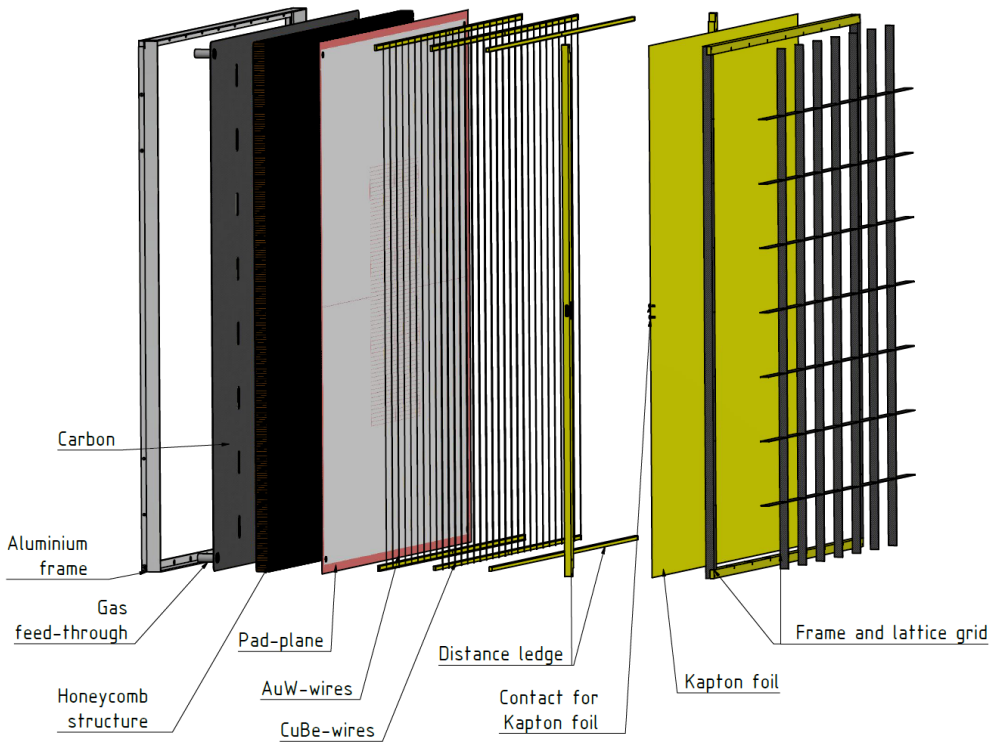

Figure 2.2.: An exposure view of a CBM-TRD MWPC is shown. A particle enters the detector from the right side through a Kapton foil entrance window into the inner part with two wire planes. A following pad plane is mounted on the back. [Coled]

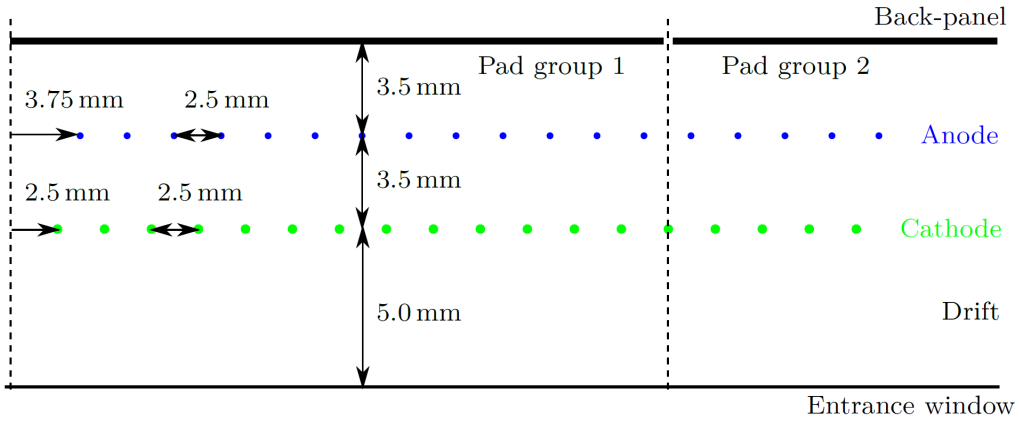

Figure 2.3.: The dimensions of the inner part of the MWPC picture the entrance window followed by a 5.0 mm drift region and afterwards by a 3.5 mm + 3.5 mm amplification region, seperated by a cathode wire plane. [Coled]

Pad Response Function The measured charge on the pad plane is concentrated around the location where the detected particle traversed the MWPC, characterized by the charge density distribution by Mathieson [Mat]

$$\rho(d/h) = q_a \frac{\frac{\pi}{2}\left(1-\frac{\sqrt{K_3}}{2}\right)\sqrt{K_3}}{4\arctan\sqrt{K_3}} \cdot \frac{1-\tanh^2\left(\frac{\pi}{2}\left(1-\frac{\sqrt{K_3}}{2}\right)\frac{d}{h}\right)}{1+K_3\tanh^2\left(\frac{\pi}{2}\left(1-\frac{\sqrt{K_3}}{2}\right)\frac{d}{h}\right)}, \tag{2.1}$$

where q_a is the charge deposition of the particle, K_3 a geometry factor of the MWPC, h the distance from the pad plane to the anode wires and d (displacement) the distance from the particle to the nearest pad center. This function, also called Pad Response Function (PRF), is pictured in figure 2.4.

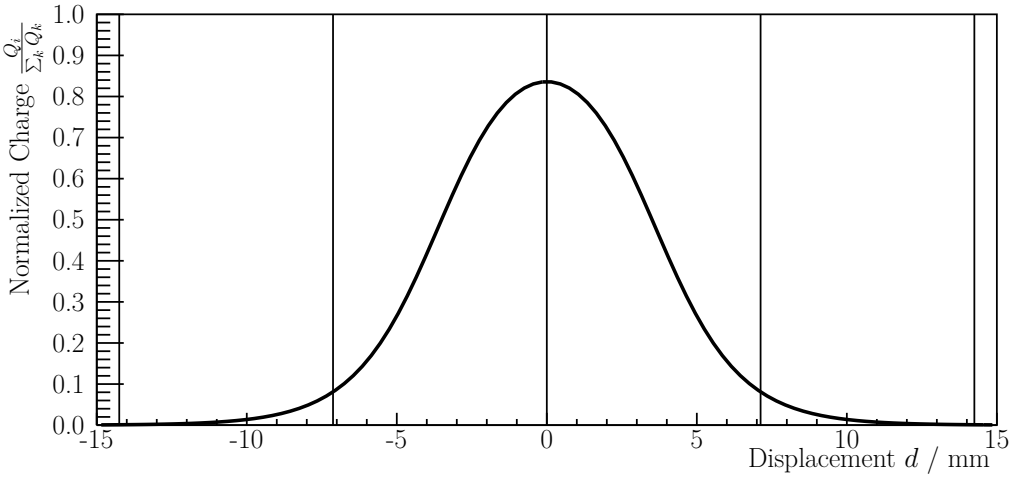

Figure 2.4.: This graph presents a PRF as the function of the normalized charge dependent on the displacement for the paremeters $K_3 = 0.38$ and the pad width $W = 7.125\,\text{mm}$. The vertical lines indicate the measurement points of a readout pad, which is one point of the PRF. By measuring several adjacent pads, the PRF can be sampled and hence later reconstructed. [Mun16][edited]

In the case of the measurement via a pad plane the charge distribution is not measured continuously but by discrete pads measuring the integrated charge over a decent area. Thus, by measuring clusters of pads around the location where the particle hits the detector, the PRF is sampled where each pad

and its measured charge represent one sample. A single pad charge can be calculated via the integral of equation 2.1 over the pad width W

$$\mathrm{PRF}(d/h) = \int_{d/h-W/2}^{d/h+W/2} \rho(d'/h)d(d'/h)\mathrm{d}d' \tag{2.2}$$

$$= -\frac{\arctan\left(\sqrt{K_3}\tanh\left(\pi\left(\sqrt{K_3}-2\right)\frac{W-2d}{8h}\right)\right)}{2\arctan\sqrt{K_3}} \tag{2.3}$$

$$-\frac{\arctan\left(\sqrt{K_3}\tanh\left(\pi\left(\sqrt{K_3}-2\right)\frac{W+2d}{8h}\right)\right)}{2\arctan\sqrt{K_3}}. \tag{2.4}$$

For later analyses the pad charge q and its displacement d have to be calculated for every readout cathode pad to reconstruct the PRF of detected hits. In favor of a convenient implementation, the PRF can be assumed nearly Gaussian so in case of three pad clusters the displacement of the pad i is calculated by

$$d = \frac{W}{2}\cdot\frac{\ln\left(\frac{q_2}{q_0}\right)}{\ln\left(\frac{q_1^2}{q_2 q_0}\right)} - W(i-2) \tag{2.5}$$

with the left pad 0, the middle pad 1 and the right pad 2 of the cluster. The charge of pad i is normalized to the whole charge of a cluster of n pads

$$q = \frac{q_i}{\sum_i^n q_i}. \tag{2.6}$$

2.3. DAQ Chain

The key part of the TRD readout chain is the SPADIC (Self-triggered Pulse Amplificateion and Digitization ASIC), integrated on the FEB (Front-End Board), which is installed on the back of the MWPC. After this front-end setup the data is sent to the ROB (ReadOut Board) multiplexing the e-links of the different SPADICs into one transmission. The resulting data stream is handed to a receiver card (Common Readout Interface (CRI)) based on a FPGA also acting as Data Processing Board (DPB). After this data pre-processing the data is sent to the FLIB/FLES (First Level Event Selection) for storage and later analysis.
In the frame of this work the SPADIC is not connected to the ROB but directly to an AFCK functioning as receiver card.

SPADIC The SPADIC chip contains 32 input channels on two chips with 16 channels. Thus, it is able to readout, amplify and digitize 32 MWPC pads at the same time. Since the SPADIC is a self-triggered device, it does not

continuously send data but decides on its own whether a signal is read out and processed. As pictured in figure 2.5 each channel is provided with a charge sensitive amplifier (CSA), an ADC followed by a programmable digital filter (DSP) and the hit detection logic.

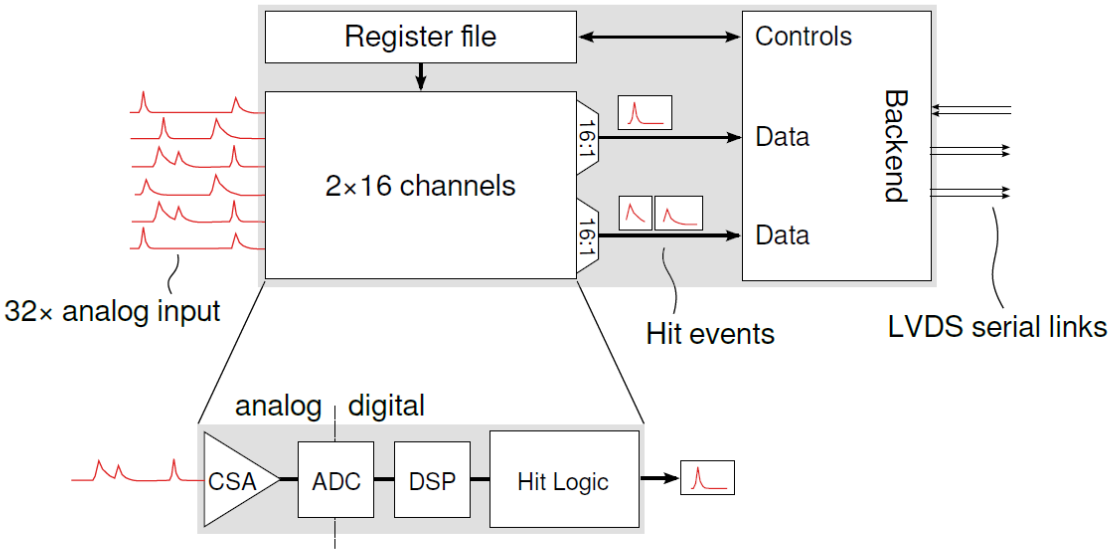

Figure 2.5.: This drawing pictures the principle of the SPADIC. The analog signal from the chamber is readout by 32 channels, each containing an amplifier (CSA), an ADC, a digital filter (DSP) and a hit detection logic. This structure digitalizes and filters the current pulse and decides whether it is recorded and further handled. Afterwards, the generated hit events are forwarded to the backend and further to the AFCK. [Coled]

The CSA is an amplifier and shaper so an incoming electric current from the detector is first amplified whereupon noise is filtered by a lowpass and a highpass. The CSA outputs a pulse of the shape

$$f(t) = A \cdot \frac{t}{\tau} \cdot \exp\left(-\frac{t}{\tau}\right) \tag{2.7}$$

proportional to the amplitude of the measured signal. τ is the peaking time of 240 ns in the case of the SPADIC 2.0.
Afterwards, the pulse is digitalized in the continuously sampling 9-Bit ADC with a sampling frequency of 16 MHz. Thus, every 62.5 ns a sample in an ADC range from -256 to 255 is created which is handled to the hit detection logic deciding whether the signal is read out and stored or not. Therefore, different trigger modes can be applied which have to be fulfilled by subsequent samples

of the ADC. Two thresholds t_1 and t_2 can be adjusted so three successive samples a, b, c have to fulfill the condition

$$t = [(a \leq t_1) \vee (b \leq t_2)] \wedge (b > t_1) \wedge (c > t_2). \tag{2.8}$$

These trigger logics are also pictured in figure 2.6.

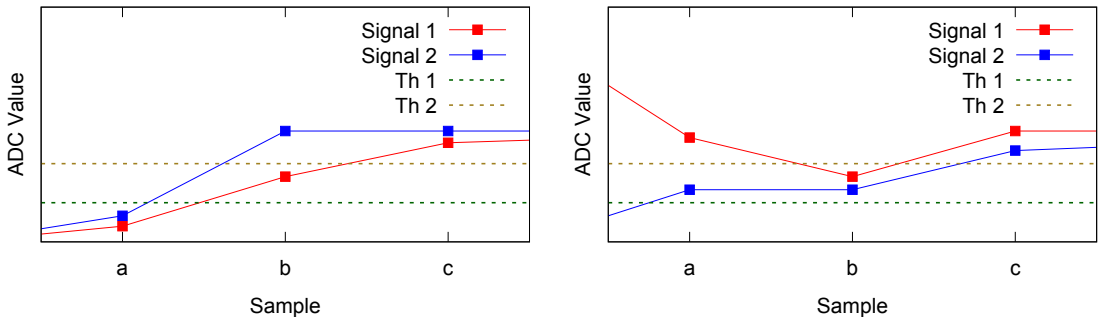

(a) $a \leq t_1$, $b > t_1$, $c > t_2$ (b) $b \leq t_2$, $b > t_1$, $c > t_2$

Figure 2.6.: These two plots present two schemes of the SPADIC trigger condition for absolute thresholds. All signals fulfill the trigger condition. [MA16][edited]

Furthermore, the thresholds can be set to differential mode where not the absolute values of samples are compared to the thresholds but the difference between subsequent samples. The trigger logic stays the same

$$t = [(\Delta_{ab} \leq t_1) \vee (\Delta_{bc} \leq t_2)] \wedge (\Delta_{bc} > t_1) \wedge (\Delta_{cd} > t_2) \tag{2.9}$$

for the sample differences Δ_{ab}, Δ_{bc} and Δ_{cd}. [MA16]
If three subsequent samples fulfill the trigger condition a certain amount of samples is readout. In order to lower the data rate, the read out data is programmable by a mask pattern in the way that individual samples can be chosen to be read out. In the case of this thesis the two samples before and the 30 samples after triggering are read out and stored so 32 samples per hit are read. In addition, every hit is provided with other meta data like the timestamp, the hit type, the stop type etc. Furthermore, the chip contains a neighbor trigger logic in such a way that adjacent channels to the initially triggered channel are read out in the same way. One differentiates between self triggered (STR) and forced neighbor readout (FNR) channels. Programming and controlling the SPADIC takes place via a serial control down link, whereas the collected data is then sent via two high speed serial links to the ROBs.
In the case of this thesis, the most important information about a hit message are:

- **Time:** The timestamp is saved as a 12-Bit value with a time of 62.5 ns (sampling frequency of 16 MHz) per timestamp. Two additional time units, the Epoch (12-Bit) and the SuperEpoch (12-Bit), which are incremented every time the previous time unit is overflowing, are used to reconstruct the total time.
- **TriggerType:** The trigger type or hit type indicates the way the hit was triggered:
  - **1:** The hit was self triggered (STR).
  - **2:** The hit was forced neighbor read out (FNR).
  - **3:** The hit was STR and FNR at the same time.
- **StopType:** The stop type indicates the way the hit stopped:
  - **0:** The hit stopped without any interruption so all samples could be read out.
  - **1:** The readout was aborted due to a filled message buffer.
  - **2:** The readout was aborted due to a full FIFO.
  - **3:** The hit was interrupted by the readout of another hit.
  - **4:** A multihit was detected but the output buffer was full.
  - **5:** A multihit was detected but the FIFO buffer was full.

  In general, stop types 0-2 can be summarized as a single physical hit, whereas 3-5 present a detected multihit.
- **Number of samples:** This value provides the number of samples of the pulse shape, which were read out. [Coled] [spa14]

2.4. Data Analysis

The data analysis flow is illustrated in figure 2.7 as a pipeline of data processing in different tasks. Before the analysis of single hits, the SPADIC raw messages of different types are decoded in the unpacker: hit message, epoch message, buffer overflow message and info message. The resulting SPADIC hit messages are analyzed in the *SimpleDigitizer* regarding their address, time, pad charge, number of samples, stop type, hit type and an additional info type. Afterwards, the resulting digis are handed to the *SimpleClusterizer* looking for valid clusters comparing the time, hit type and pad number of individual digis. The created clusters are investigated in the *ClusterAnalysis*, where processes like the calculation of a PRF or an energy spectrum take place. During the analysis process, all required parameters, the

chamber geometry, the FEE assembly and the sampling frequency, are taken from the *TestBeamTools* class which can be called by every task. [MBF+17]

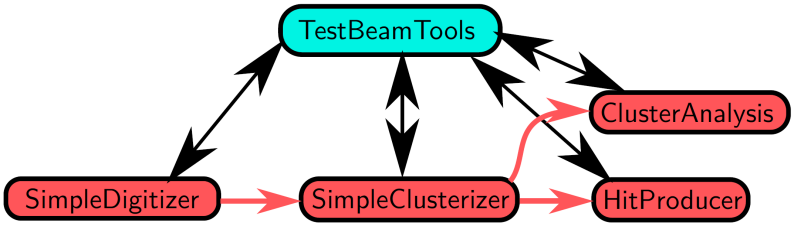

Figure 2.7.: The data flow of the analysis software presents different tasks (red) handling the data. All tasks call the parameters from the *TestBeamTools* class. The *HitProducer* is not used within this thesis. [MBF+17]

2.5. Decay and Spectrum of ^{55}Fe

All following measurements are conducted with a ^{55}Fe source, mainly decaying via electron capture of a 1s electron into ^{55}Mn with a half life of 2.737 years. The filling of this vacant remaining state leads with a probability of 60 % to the emission of a 5.19 keV Auger electron. Due to their short mean free path length, the electrons do not reach the MWPC and thus are not detected.
Other statistical relevant emissions due to the transition in the 1s orbital are a 5.90 keV $K_{\alpha 1}$ (16.22 %), a 5.89 keV $K_{\alpha 2}$ (8.2 %) or a 6.49 keV K_{β} (2.85 %) photon. Due to the small energy difference of the two K_{α} lines, they are often detected as one. [MMB06]
Since argon is used as inert gas inside the MWPC, the argon escape lines are expected to be measured as well. The major expected peak originates from the argon K_{α} photon at 2.96 keV. [Sch08]

3. Measurements and Data Analysis

This chapter provides the execution and analysis of two major measurements, one concerning the anode voltage without any usage of the readout electronics and another one concerning the electronics in order to ensure an appropriate SPADIC ADC gain matching. The analysis of the recorded pulse shapes contains the investigation of the multihit scenario.
The data used for data analysis is taken from one measurement conducted with Sagox (Ar/CO_2 82/18) at an anode voltage of 1850 V, and both thresholds set absolute at -150 ADC. In the following, the unit 'ADC' is used for ADC values.

3.1. Anode Current Measurements

The proper function of the overall setup and DAQ can be investigated by measuring the gas gain in terms of the anode current.
The anode current is measured at anode voltages from 1600 V to 2100 V with several measurements of 5 min, recording the current every 0.5 s. Due to very low and varying currents during one period, the ^{55}Fe source is mounted directly in front of the chamber without any collimator being installed in front of it. The anode current is read out directly from the MPOD crate. Figure 3.1 shows the measured current trend at an anode voltage of $U_A = 1850\,\mathrm{V}$. It reveals slight fluctuations which can result from characteristics inside the MWPC. Oscillations of the gas pressure, density, volume, composition and contamination or the temperature can affect the gas gain and thus the measured anode current. Furthermore, surface currents on the filter board of the readout electronics were observed which can also influence the measurements[1].
The final data points at each operating voltage are determined as the average value of the current in one measurement taking the standard deviation as uncertainty. The individual anode current trends can be found in the appendix in figures A.1 to A.4. Figure 3.2 pictures the anode current as a function of the anode voltage in a linear and a logarithmic presentation with

[1] private communication, P. Kaehler

an exponential fit. This exponential trend indicates that the MWPC operates in the proportional counting regime and provides data for energetically resolved measurements.

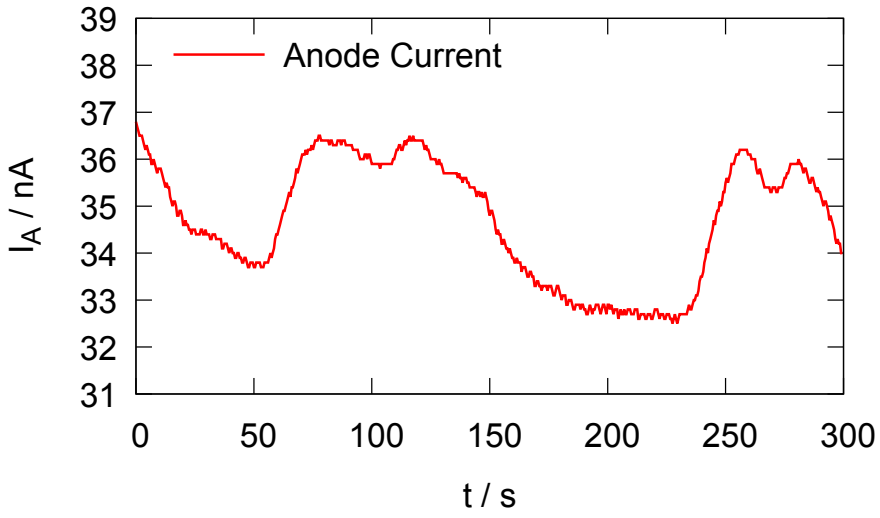

Figure 3.1.: This diagram pictures the anode current as a function of time for an anode voltage of $U_A = 1850\,\mathrm{V}$, measured by the MPOD with a readout frequency of 2 Hz.

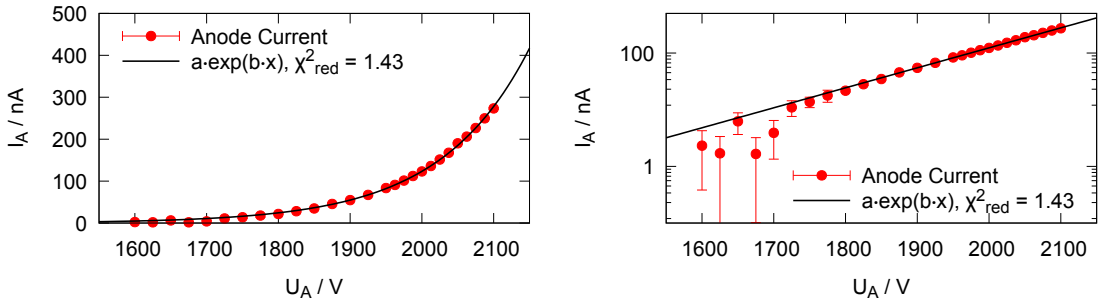

(a) anode current

(b) anode current logarithmic

Figure 3.2.: These two plots show the anode current I_A as a function of the anode voltage U_A in a linear (a) and logarithmic (b) presentation. An exponential function $f(U) = ae^{bU}$ is fit to the data. The fit parameters are $a = (1.1 \pm 0.1) \cdot 10^{-5}$, $b = (8.1 \pm 0.1) \cdot 10^{-3}$.

3.2. Gain Matching Measurements

The gas gain matching of the setup can be confirmed by measuring the height of the SPADIC pulse shapes at different anode voltages to see whether the pulses fit into the ADC range of the SPADIC.
Therefore, measurements with the ^{55}Fe source with a 3 mm collimator are conducted where one single SPADIC is used for the readout. A hitmap of the SPADIC is shown in figure 3.3 presenting all 32 read out channels and the amount of hits (only STR) detected on each of them. Following the hitmap, the iron source is arranged in the way that the radiation is concentrated on the middle of pad 7 in row 1.

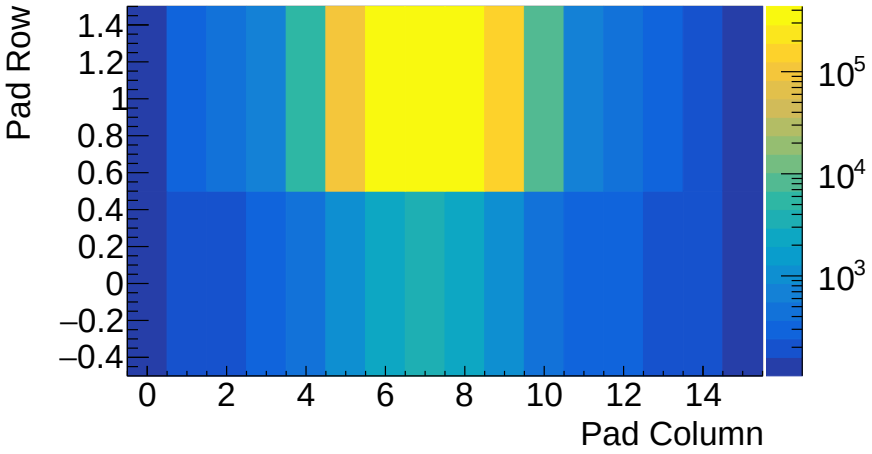

Figure 3.3.: This plot presents the hitmap of the SPADIC in the experimental setup. It pictures the number of STR pulses on every of the 32 channels arranged in two rows with 16 channels each.

All STR pulse shapes of the most frequently hit channel, recorded at an anode voltage of $U_A = 1850$ V with both thresholds set absolute at -150 ADC, are shown in figure 3.4. The pulse shapes reveal two major lines (yellow), probably the one with higher ADC values originating from the ^{55}Fe K_α line and the lower one from the argon escape peak.
In order to obtain information about the dependence of the gas amplification on the anode voltage, the pulse shapes recorded at different anode voltages are analyzed regarding their mean maximum ADC value of the K_α line. This value is later taken as a data point at every high voltage.
Matching the pulses of all expected particle species into the available ADC range is required to achieve good energy resolutions. Therefore, the well known energy loss of MIPs is wished to be shifted to a defined value,

which is related to the energy deposition of the ^{55}Fe K_α particles. Since the ^{55}Fe photons are assumed to deposit their full energy in the MWPC they can be compared to the MIPs energy loss without any further energy loss calculations. Expecting the MIPs to cover a certain percentage of the detectors energy range, the desired ADC coverage of the 5.9 keV ^{55}Fe photons can be calculated.

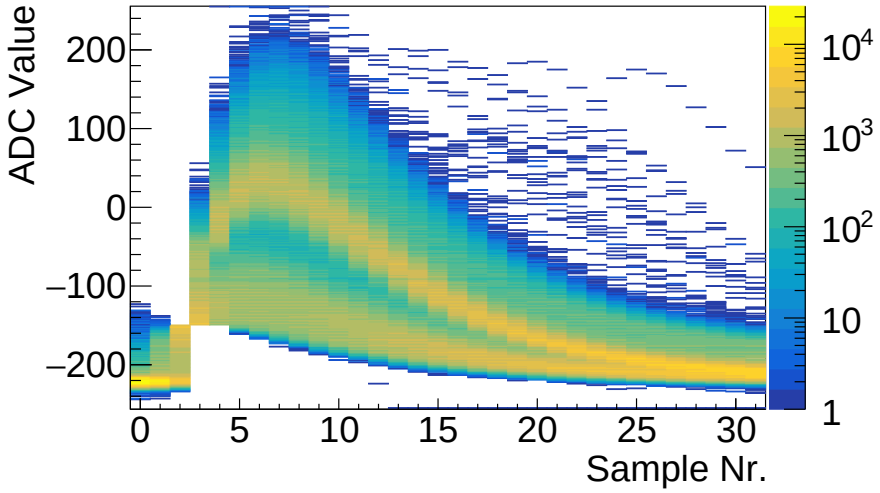

Figure 3.4.: STR pulse shapes (ADC value as a function of the time represented by the sample nr.) of one SPADIC channel at $U_A = 1850\,\mathrm{V}$ are pictured. Both thresholds are set absolute to -150 ADC.

Minimum Ionizing Particles

The energy loss of MIPs in argon is $\left.\frac{\mathrm{dE}}{\mathrm{d}x}\right|_{MIP} = 2.71\,\mathrm{keV\,cm^{-1}}$. In the 12 mm thick MWPC the total energy loss of a MIP is $\Delta \mathrm{E}_{min} = 3.25\,\mathrm{keV}$. However, the measurements include no pure gases but gas mixtures of Ar/CO_2 82/18. The energy loss in the gas mixtures can be calculated via

$$\left.\frac{\mathrm{dE}}{\mathrm{d}x}\right|_{mixture} = \sum_i w_i \left.\frac{\mathrm{d}\epsilon}{\mathrm{d}x}\right|_i$$

where w_i and $\left.\frac{\mathrm{dE}}{\mathrm{d}x}\right|_i$ are the volume percentage and energy loss of one gas in the mixture. [eaP13]
With a MIP's energy loss in carbon dioxide of $\left.\frac{\mathrm{dE}}{\mathrm{d}x}\right|_{MIP,CO_2} = 3.60\,\mathrm{keV\,cm^{-1}}$ the energy deposition in the TRD chamber is $\Delta \mathrm{E}_{min,ArCO_2} = 3.47\,\mathrm{keV}$.

Due to the drift of the electrons inside the MWPC and the associated drift time, the complete collection of the created charge has to be guaranteed. The maximal signal collection time of the readout chamber is 300 ns. The drift velocity of the created electrons in the drift region comes into play comparing the ionization processes of MIPs and photons. MIPs ionize atoms along their whole track resulting in different times of arrival of the drifting electrons. Thus, the whole energy loss of a MIP may result in a longer pulse or the detection of multiple pulses. This effect will not occur in the case of detected photons. Due to the photons' interaction via the photoelectrical absorption one can assume that these photons are interacting once with a gas atom being absorbed and depositing all their energy in one interaction. Thus, the primary electrons in the gas chamber are created highly localized in contrast to traversing particle trajectories with energy loss along their tracks.
Measurements of the drift velocity in argon gas mixtures have been done, pictured in figure 3.5. Comparing these measurements with the CBM TRD setup, the drift velocities are in the area of $v_{drift,Ar} = 5.2\,\mathrm{cm\,\mu s^{-1}}$ assuming the detector operating at atmospheric pressure, the drift voltage $U_{drift} = 500\,\mathrm{V}$ and a drift length of 5 mm resulting in an electric field of $E_{drift}/p = 0.99\,\mathrm{V\,cm^{-1}\,mbar^{-1}}$. Accordingly, the drift time of electrons is $t_{drift,Ar} = 96\,\mathrm{ns}$ and therefore shorter than the signal collection time of 300 ns. Thus, in one event the electronic measures the whole charge that was induced by a MIP on the cathode pads.
In order to ensure proper ^{55}Fe measurements, the MIPs deposited energy is assumed to occupy about 20 % of the ADC range. Thus, the 5.9 keV ^{55}Fe K_α photons should take 34 % of the available ADC range. [GS08] [ABBM+04] [Coled]

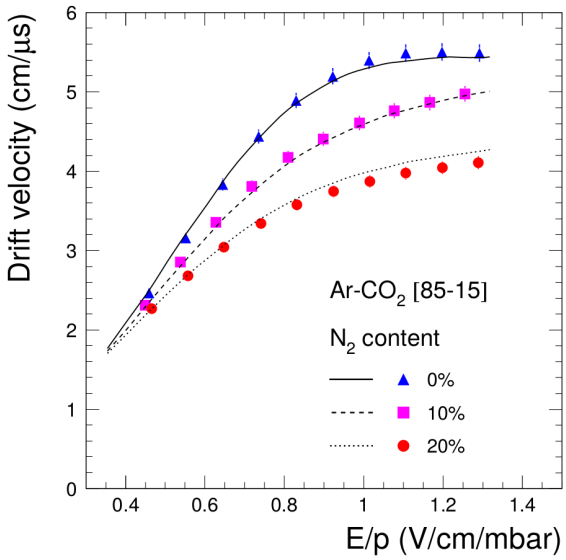

Figure 3.5.: This plot pictures the drift velocity of electrons dependent on the electric field in Ar/CO_2 85/15 with different N_2 content and comparisons with simulations. [ABBM+04]

Measurements

Measurements from 1650 V to 1900 V (figures A.5 and A.6) are conducted with the baseline of the SPADIC set to -220 ADC resulting in a total ADC range of 475. The mean maximum ADC value of the iron K_α line is pictured in figure 3.6 as a function of the anode voltage U_A as well as the covered ADC range. Both data sets are fit by an exponential function.

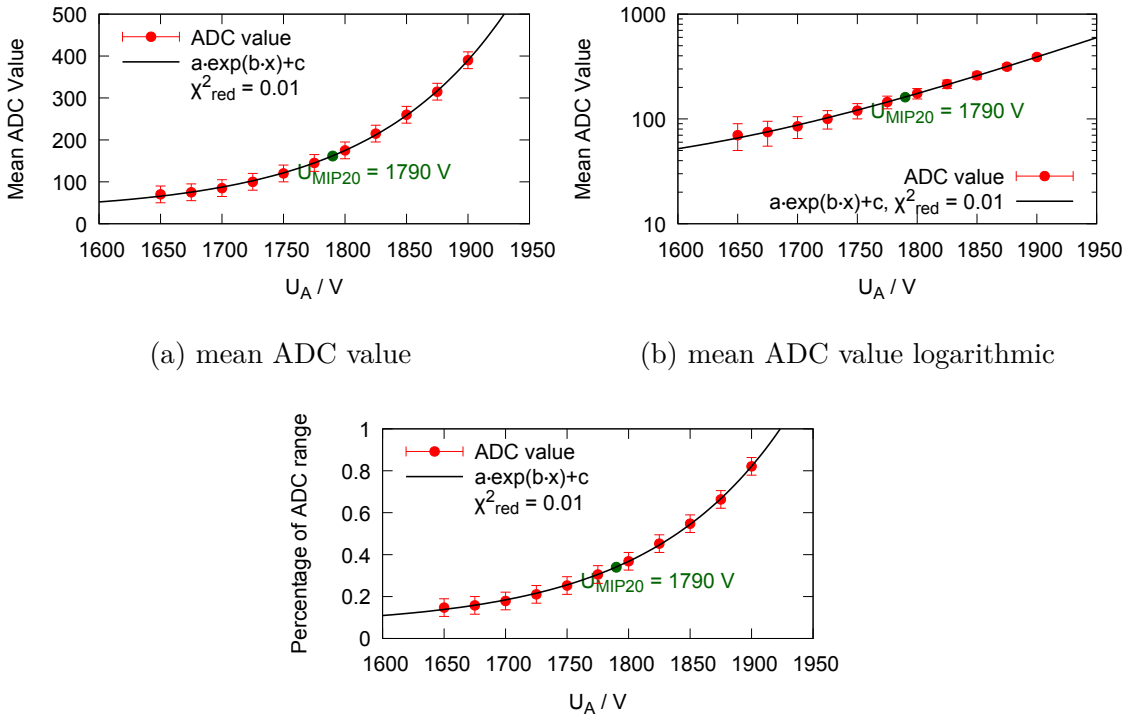

(a) mean ADC value

(b) mean ADC value logarithmic

(c) covered ADC percentage

Figure 3.6.: These diagrams picture the mean maximum ADC value of the iron K_α line as a function of the anode voltage U_A (a), fit by the function $f(U) = ae^{bU} + c$. The optimal voltage of 1789.5 V is determined as the voltage where 34 % of the ADC range is occupied by the mean ADC. (b) has logarithmic y-axis while (c) shows the covered area of the ADC by the mean ADC as a function of the anode voltage. The fit parameters are $a = (1.3 \pm 0.6) \cdot 10^{-5}$, $b = (9.0 \pm 0.2) \cdot 10^{-3}$, $c = (27.8 \pm 3.8)$ ((a) and (b)) or $a = (2.7 \pm 1.2) \cdot 10^{-8}$, $b = (9.0 \pm 0.2) \cdot 10^{-3}$, $c = (5.9 \pm 0.8) \cdot 10^{-2}$ ((c)).

As calculated before, the optimal operating voltage U_{opt} is the voltage at which the 5.9 keV photons cover 34 % of the ADC range. With the obtained

fit function this voltage can be determined as $U_{opt} = 1789.5\,\mathrm{V}$.
Since the gas gain shows an exponential dependency on the operating voltage and U_{opt} fits within this area, the MWPC is working in the proportional counting region. The functionality of the test stand is confirmed as in the anode current measurement before. Therefore, analysis regarding the reconstruction of an energy spectrum can be conducted.

3.3. Multihit Identification

In order to ensure spectrum reconstruction without biasing, the complete recording needs to be analyzed especially regarding fractured pulses resulting from multihits as demonstrated in figure 3.7. Multihits occur if the trigger condition is fulfilled a second time during the recording of a hit. The second trigger has to take place within a time window of 32 timestamps. In this case, the readout of the first hit is interrupted with a stop type ≥ 3 due to the readout of the second hit resulting in an inclompete pulse shape of the first hit and a raised second pulse due to the contribution of the first one.
In order to reconstruct the fractured pulse shapes (predecessors), hits with a stop type ≥ 3 are stored in a multidimensional array depending on the channel it was detected as pictured in table 3.1. A following hit in the same channel is compared to the respective array entry regarding the time. If the time difference is less than 32 timestamps, the hit can be identified as a successor.

Table 3.1.: This table demonstrates the structure of the predecessor array. Each row represents one SPADIC channel involved in the DAQ predecessor array. For every channel different values of the predecessor are saved: the time, the number of samples, the hit type, the baseline and the individual samples.

Channel	Time	Nr. of Samples	Hit Type	Baseline	Samples (32)
0					
1					
. .					
31					

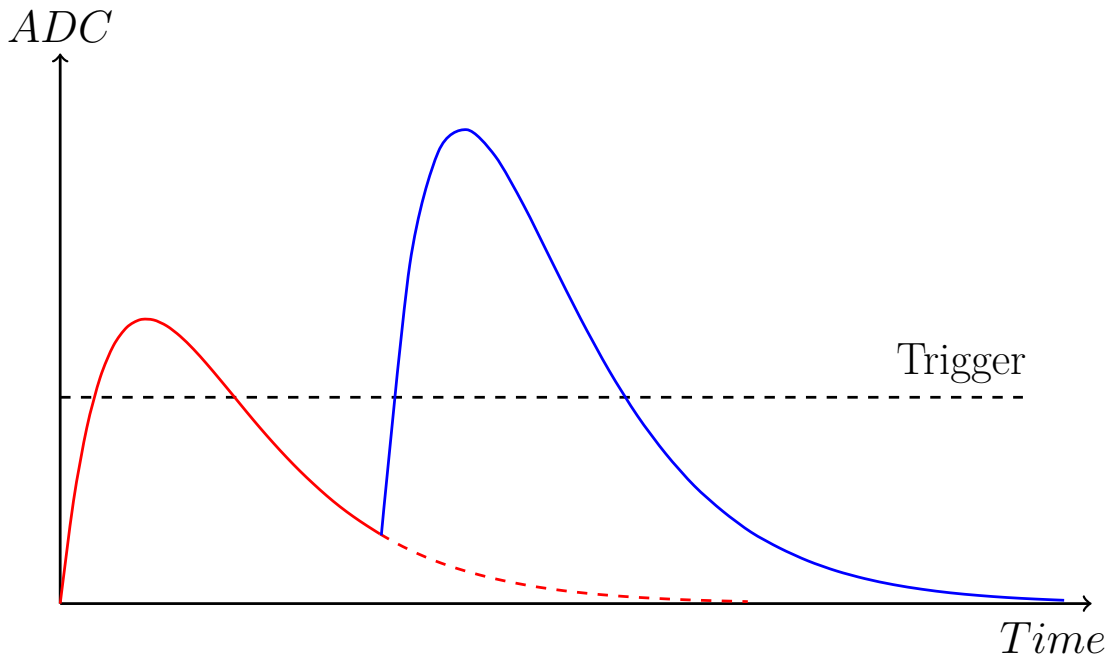

Figure 3.7.: This drawing illustrates the multihit scenario. A second hit occurs within 32 timestamps after a first hit on the same pad. The readout of the first hit is interrupted by the readout of the second one. In this case no sample is lost and every sample is recorded once. [KBF+17][edited]

3.4. Multihit Analysis

Before reconstructing the multihits it is quite interesting to analyze some characteristics of their pulse shapes.
Figure 3.8 pictures the hit type distribution of the identified predecessors and successors. The percentage of STR (hit type = 1) to FNR (hit type = 2) pulses should be about 1:2 ideally, due to the dominantly occurring three pad clusters. However, in the case of predecessors as well as successors it is nearly even.

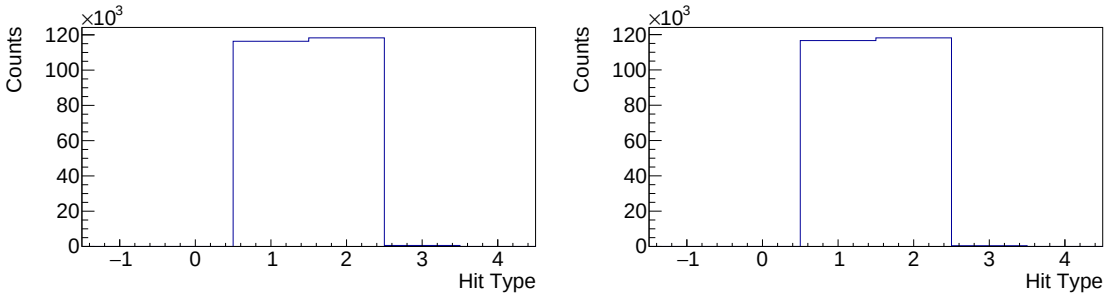

(a) Predecessor hit type

(b) Successor hit type

Figure 3.8.: These plots show the hit type distribution for predecessors (a) and successors (b).

Furthermore, looking at the number of samples (NOS) of the predecessors, as pictured in figure 3.9, the accumulation at small NOS up to four is noticeable, whereas most of the successors have 32 samples and an otherwise equally distributed NOS. The expectation of the average time between two hits depends on the activity and setup of the ^{55}Fe source and can be determined by the measured hit frequency. Figure 3.10 pictures the total amount of clusters, which can be defined as hits, counted in 100 ms. The distribution is Gaussian with a mean hit frequency of 2857 s^{-1} resulting in an average time between two hits of 350 µs, much longer than the time of a 32 sample pulse ($\sim$ 2 µs).

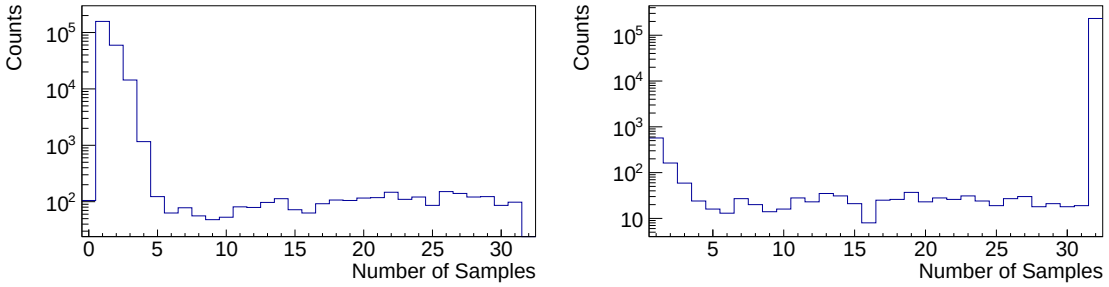

(a) Predecessor number of samples (b) Successor number of samples

Figure 3.9.: These diagrams outline the distribution of the number of samples of the predecessors (a) and successors (b) in a logarithmic presentation.

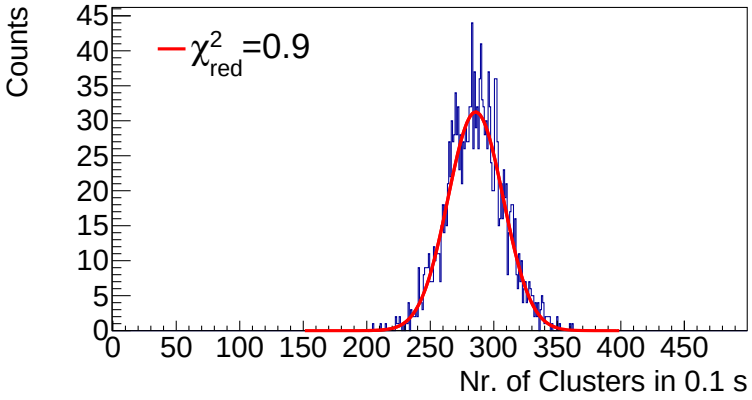

Figure 3.10.: The hit frequency, defined as number of clusters measured in a time period of 0.1 s is fit by a Gaussian function. The fit parameter are $\mu = 285.70 \pm 0.55$ and $\sigma = 21.71 \pm 0.46$.

Therefore, the increasing number of one to four sample predecessors is an unexpected characteristic because most of the detected hits should end without any readout interruption as in the case of successors. Additionally,

immediately retriggering the predecessor should not be possible because the pulse would have to fall below the threshold and pass it again to fulfill the trigger condition a second time. However, the pulse shapes indicate their maxima at the sixth or seventh sample. A physical multihit would just add more charge to the previous pulse, so underrunning the threshold and retriggering should not be achieved in these first samples. Therefore, most of the identified successors appear to be caused by a non physical reason.
Taking the NOS and hit type into one graph can be observed in figure 3.11, picturing the number of samples of the predecessor dependent on the hit type of the successor, where the predecessor was STR in (a) and FNR in (b). In the case of predecessors up to four samples, these two plots show that a STR predecessor leads to a most likely FNR successor, while a FNR predecessor is mainly followed by a STR successor. That indicates the retrigger of one pad occurring due to the triggering of one of its adjacent pads. In more detail: the charge generated by an incoming particle is not measured by only one but spread over several pads why the adjacent pads of a triggered pad are read out as well. However, the charge of a FNR pad can be high enough to pass the trigger condition causing the FNR pad to trigger as STR and its adjacent pad, the initial STR, to be read out as FNR. Due to the lower charge deposition in the primary FNR pad, the resulting pulse shape has a higher rise time and the pad is triggered, shifted in time to the corresponding STR pad, in this case up to four samples later. This scenario, called multimessage from now on, leads to the behavior as observed in figure 3.11 and schematically pictured in figure 3.12.

1. A STR readout is stopped and followed by a FNR readout caused due to a STR in the adjacent pad (picture 3.11(a)).
2. A FNR readout is stopped and followed by a STR readout because the pulse shape reaches the trigger condition (picture 3.11(b)).

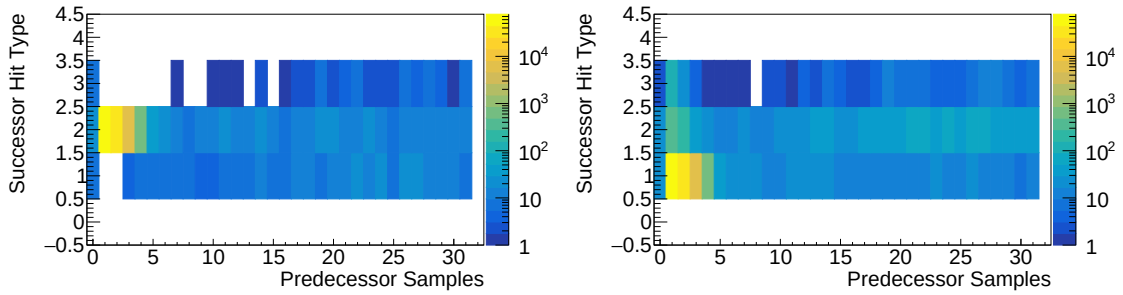

(a) STR predecessor (b) FNR predecessor

Figure 3.11.: Both plots show the number of samples of the predecessor against the successor hit type. In (a) the predecessor was self triggered whereas it was neighbor read out in (b).

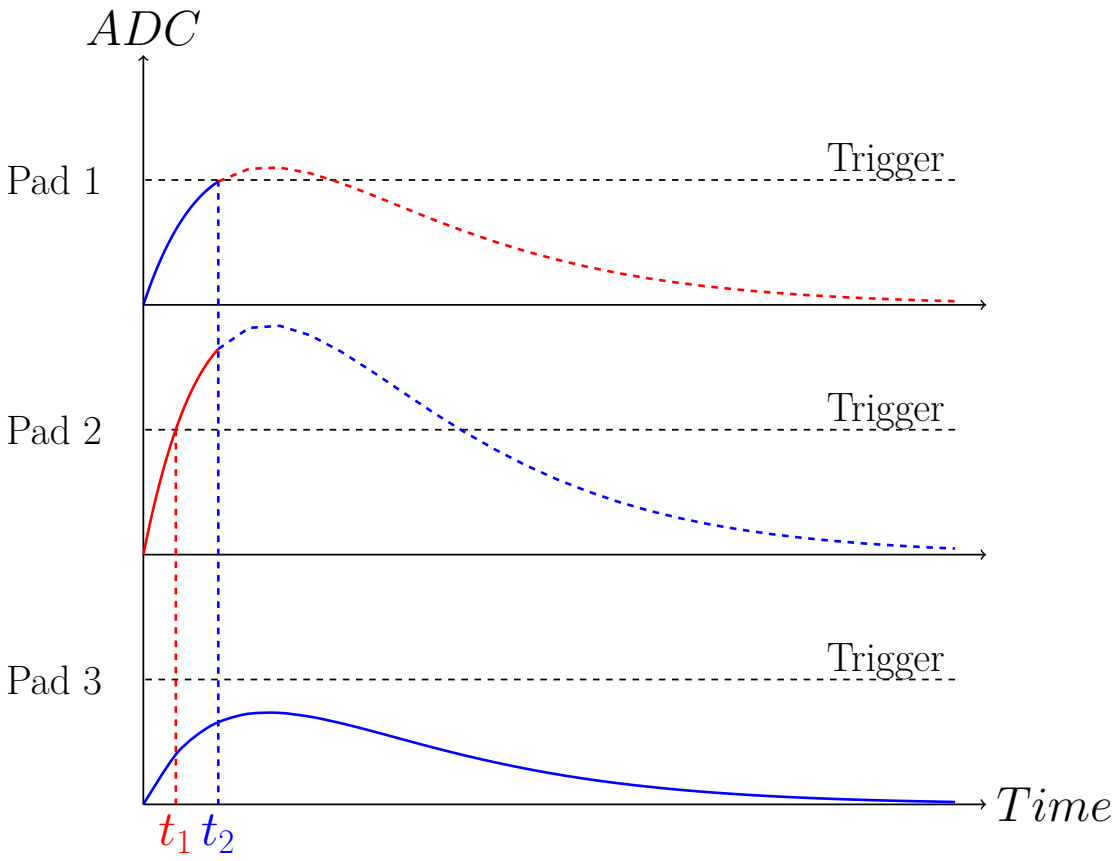

Figure 3.12.: This drawing presents the multimessage scheme in the case of a detected three pad cluster. The ADC value of three pads is shown in dependence of the time. Blue lines indicate the pulse shapes of FNR pads as red lines indicate the STR pads. In this case, the main charge is deposited on pad 2 causing the pulse to exceed the trigger condition at t_1 and the STR trigger of pad 2 and FNR trigger of pad 1 and 3. After a decent time t_2, the pulse of pad 1 also exceeds the trigger threshold whereby the electronics recognize a new event. Hence, the FNR readout of pad 1 is stopped by a STR readout and the adjacent pads, in this case pad 2, are read out as FNR pads. This retrigger usually occurs within a short time window up to four timestamps ($\sim 250\,\mathrm{ns}$).

Multimessage and Multihit Differentiation

Even if most of the detected multihits with less than five samples time difference are multimessages, real physical multihits also can occur in this time window. Therefore, it is reasonable to differentiate these two scenarios in the reconstruction chain.

In both events the two detected hits (predecessor and successor) should initially be composed in the way that the samples are put together. In the case of multimessages, the resulting pulse should show a normal shape of one hit, whereas for physical multihits additional charge is measured leading to an abnormal rise of the pulse shape. The two incidents could be distinguished by the rise of the pulse shape depicting in the difference of the first samples. Figure 3.13 presents several differences of following samples: the difference of the third to second sample in (a), the sum of the differences of the third to second and fourth to third sample in (b) continuing for (c) and (d).

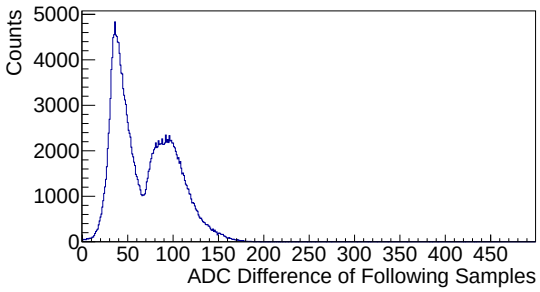

(a) Difference of two samples

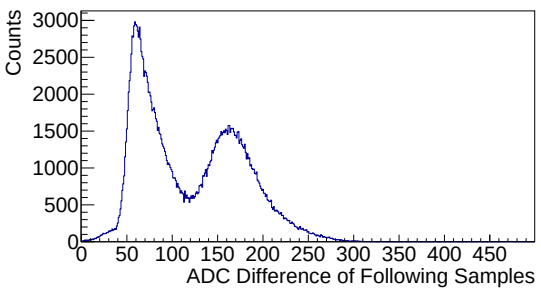

(b) Difference of three samples

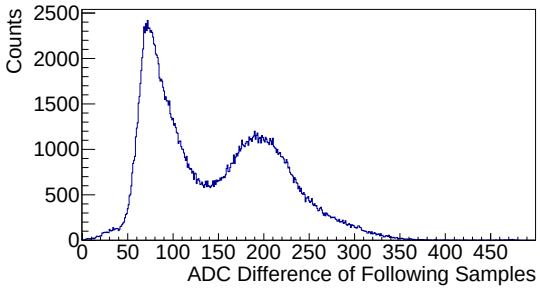

(c) Difference of four samples

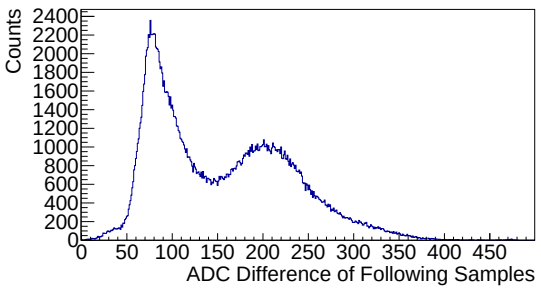

(d) Difference of five samples

Figure 3.13.: These graphs reveal the difference of following samples of composed multihits with a time difference less than 5 timestamps. In (a): difference from 2. to 3. sample. In (b): sum of differences from 2. to 3. and 3. to 4. sample. In (c): sum of 2. to 3., 3. to 4. and 4. to 5. sample. In (d): sum of 2. to 3., 3. to 4., 4. to 5. and 5. to 6. sample.

All four graphs show the same characteristics revealing two peaks, which could belong to multimessages in case of small sample differences and to physical multihits in case of large sample differences. Looking at 3.13 (d), a cut can be applied at about 150 ADC to find out if the pulses with differences below and above this threshold differ in their shape.
The pulse shapes of the compounded multihits are presented in figure 3.14 where (a) shows all composed pulses and (b) and (c) the ones with a sample difference greater and smaller than 150 ADC. (a) reveals a similar structure to normal pulse shapes with two major lines (yellow), corresponding to the argon escape and the iron K_α line, but also very high pulses clipping above the ADC range. The differentiation in (b) and (c) leads to a segmentation of high and low pulses. However, a clear determination of physical multihits and multimessages can not be done since the shapes with high sample differences contain the pulses of the iron K_α X-rays. Identifying all composed multihits with a high rising shape as physical multihits would cause an incorrect identification of many pulses originating from real physical higher energetic particles. Hence, this algorithm does not help to distinguish multimessages from physical multihits.

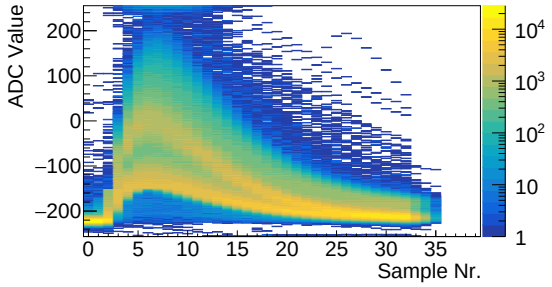

(a) Pulse shapes of all composed multihits

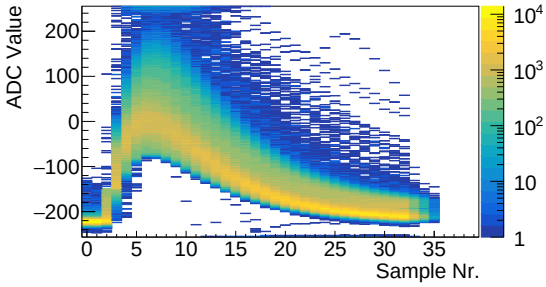

(b) Sample difference > 150 ADC

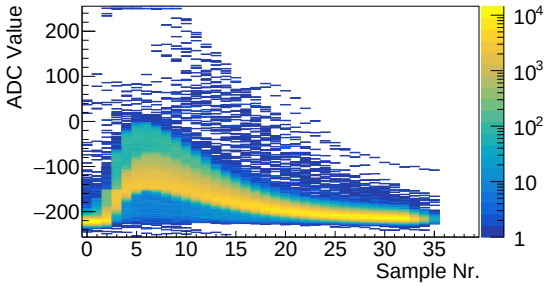

(c) Sample difference < 150 ADC

Figure 3.14.: These plots picture the pulse shapes of composed multihits with a time difference smaller than five timestamps. (a) shows all pulses while (b) and (c) contain only pulses with a sample difference (according to figure 3.13(d)) greater and lower than 150 ADC.

Within later reconstructions, multihits with a time difference of less than five samples are always treated as multimessages so the samples of the predecessor and successor are simply put together.

3.5. Hit Reconstruction

With these investigations and results the reconstruction of multihits can be implemented. Every pulse shape is corrected by the baseline, which is defined as the first recorded sample of a hit. Overall, three different types of hits have to be handled: predecessors, successors and multimessages.

- Predecessors are fit by the ideal pulse shape resulting from the electronics

$$f(t) = A \cdot (t - c) \cdot \exp\left(-\frac{t - c}{\tau}\right) \tag{3.1}$$

  with the free parameter A, c and τ. Due to the readout of the two previous samples of a hit, the first sample of the predecessor is neglected, as it is most likely not influenced by the pulse. Furthermore, in order to guarantee a proper fit quality, the pulse shape should have reached its maximum, which is usually fulfilled for pulses with eight or more samples. Many pulses do not show an appropriate shape but do often look like some kind of noise due to a very low charge deposit on this pad. Thus, fit pulses additionally should have a maximum value greater than 50 ADC (above the baseline).

- Successors are corrected with the calculated samples and the baseline of the predecessor. The first $(32 - t_{diff})$ samples of a successor, occurring after a time of t_{diff} (in units of timestamps) after the predecessor, are corrected by

$$\text{Sample}[i]_{\text{corrected}} = \text{Sample}[i]_{\text{succ}} - \text{Sample}[i + t_{diff}]_{\text{pre}} - \text{Baseline}_{\text{pre}}. \tag{3.2}$$

- Multimessages are identified as multihits with $t_{diff} < 5$. The samples of the predecessor and successor are composed where the successor samples are corrected by the predecessor baseline. The time and hit type of the predecessor is taken for the creation of a digi.

Following these reconstructions, predecessors between five and eight samples and predecessors with a maximum less than 50 ADC, as well as their successors, are lost. Furthermore, clipping pulses, whose pulses exceed the ADC range of the SPADIC, are discarded due to an inaccurate charge reconstruction. The whole reconstruction chain, taking place in the *Digitizer*,

is pictured as a flowchart in figure 3.15. For further analysis a new attribute is attached to a digi, the multihit type:

- **0**: Normal hit with stop type 0 and 32 samples.
- **1**: Predecessor.
- **2**: Successor.
- **3**: Multimessage.
- **4**: Predecessor and Successor.
- **5**: Multimessage and Predecessor.

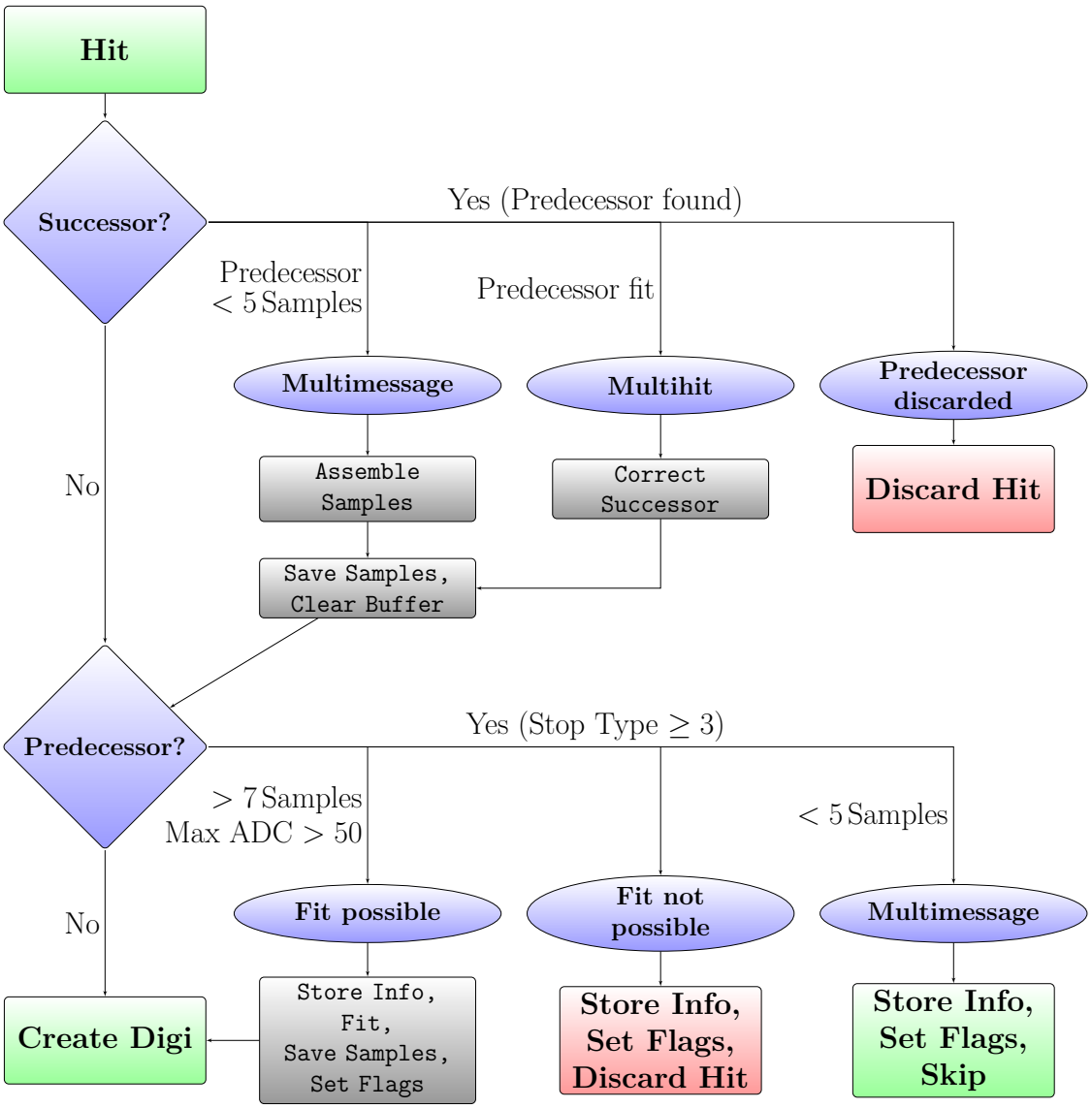

Figure 3.15.: This flowchart depicts the scheme of the multihit reconstruction algorithm implemented in the *Digitizer*. A recognized hit is checked whether its a successor. If a proper predecessor is found, the multihit needs to be characterized: multimessage (in case of a predecessor <5 samples) or physical multihit. In the latter case the successor can only be corrected, if the predecessor is corrected as well, otherwise it has to be discarded. If possible, the successor is corrected, the predecessor buffer of this channel is cleared and it is checked whether the same hit is also a predecessor. In this case, the predecessor correction is additionally applied: the hit is fit and corrected, if it has more than seven samples and a maximum ADC value larger 50 ADC, flagged as multimessage if it has less than five samples or discarded otherwise. Only in the first case a digi is created, while in all other cases the basic hit information is stored in the predecessor buffer.

3.6. Reconstruction Algorithm Validation

Implementing this reconstruction into the *Digitizer* results in the pulse shapes in figure 3.16 picturing all pulses contributing to the clusters which are built in the *Clusterizer*.

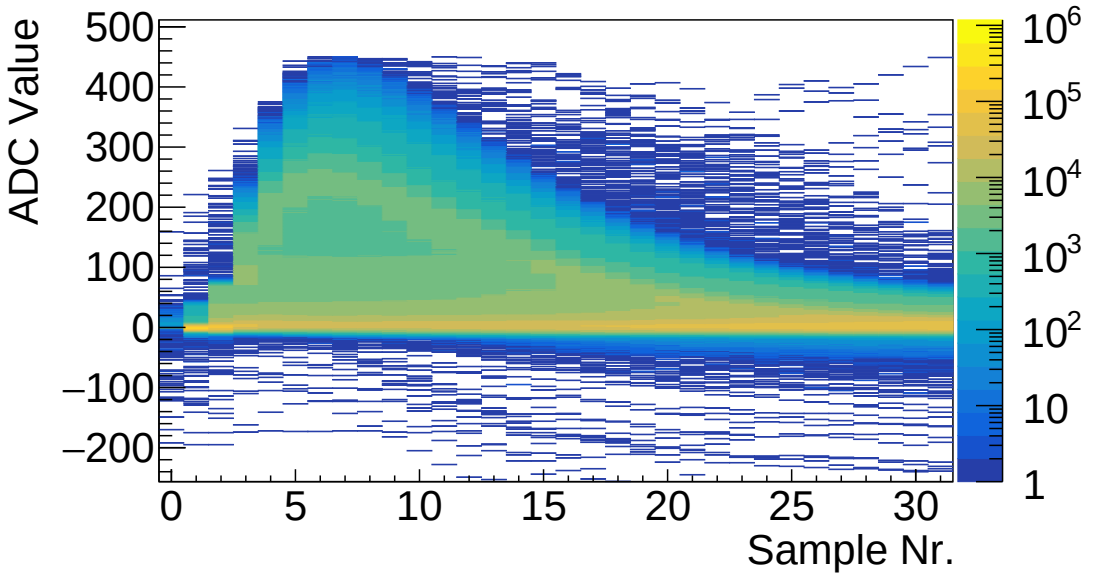

Figure 3.16.: These are all pulse shapes resulting from the reconstruction algorithm in the *Digitizer* which are then handed to the *Clusterizer*.

There are several ways to check if the reconstruction is successful and the digis are created in the correct way. Table 3.2 shows the number of the initially detected, normal (stop type 0), reconstructed and lost hits per individual run. The sum of normal, reconstructed and lost hits is always equal to the detected hits with a percentage of lost hits of $\sim 0.2\,\%$ - $0.3\,\%$.
Furthermore, figure 3.17 shows the multihit type of digis versus the size of the cluster they were associated to. The equal distribution and especially the high amount of 3 pad cluster with multimessages (multihit type 3) indicate a correct creation and handling of reconstructed digis.
In order to check if the predecessor fits have a good quality, the results of the reduced chi square tests are pictured in figure 3.18, with a mean of 0.45 and only a few runaways at higher values. Thus, the fit functions match well to the cut pulse shapes.

Table 3.2.: This list contains the amounts of reconstructed, normal and lost hits as well as the total hits processed in the *Digitizer* for different runs at differing anode voltages. In addition, the percentages of lost hits compared to the total hits are presented.

Run	Reconstructed Hits	Normal Hits	Lost Hits	Total Hits	% Lost
1775V	82911	915910	2141	1000962	0.21
1800V	140636	947719	2542	1090897	0.23
1825V	185025	930976	2468	1118469	0.22
1850V	232234	948035	2627	1182896	0.22
1875V	278268	954140	2462	1234870	0.20
1900V	313966	954594	3606	1272166	0.28

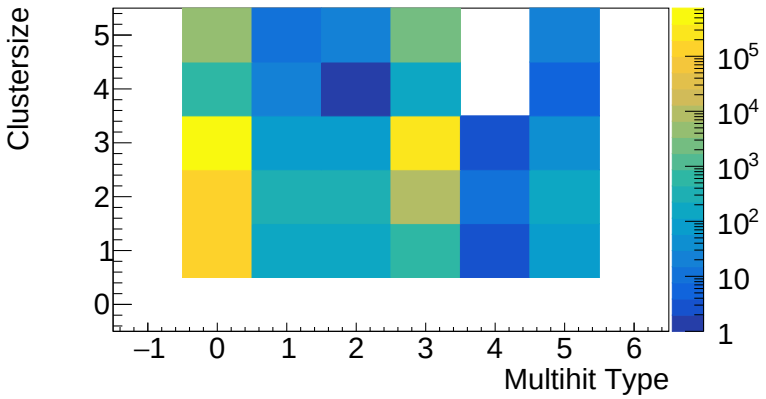

Figure 3.17.: This plot shows the size of clusters including a digi with multihit type.

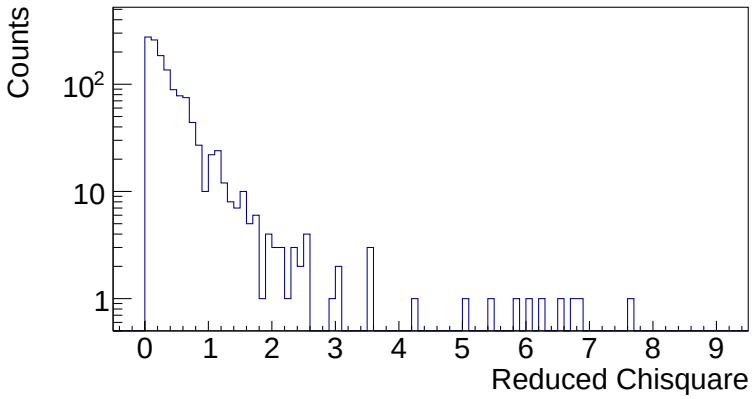

Figure 3.18.: This plot presents the results of the reduced chi square tests of the predecessor fits. The arithmetic mean chi square value is 0.45.

4. Results

In the following, different ^{55}Fe spectra with and without applying the multihit reconstruction are outlined, analyzed and compared with each other.

4.1. ^{55}Fe Spectrum Reconstruction

The recorded pulse shapes provide data for the charge measured by one single cathode pad. The reconstruction of the total charge of one pad can be achieved by integrating over the whole pulse shape, summing up the ADC values of each sample. The complete charge created by one particle is captured in a cluster including at least three adjacent pads. To obtain complete information about the energy of the detected particle the charge of the cluster has to be calculated, e.g. by adding the single pad charges. Applying this reconstruction chain on three pad clusters without the multihit reconstruction results in the spectrum in figure 4.1. It reveals a ^{55}Fe spectrum looking at the two peaks at ~ 2200 ADC and ~ 4000 ADC matching to the argon escape peak and the iron K_α line. Nevertheless, two undesired features, many entries at low ADC values and a tail of the K_α peak to higher ADC values, appear.

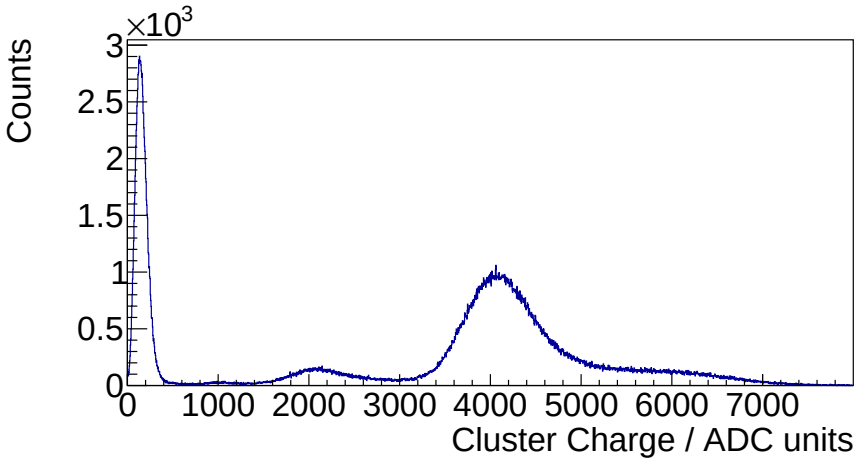

Figure 4.1.: This plot presents the spectrum of ^{55}Fe without the multihit reconstruction. The cluster charge is calculated by adding up the single pad charges of three pad clusters. The pad charge is the sum of the ADC values of every sample.

Spectrum with Multihits

The same spectrum with the multihit reconstruction is pictured in figure 4.2 featuring the argon escape peak (2.96 keV) as well as the ^{55}Fe K$_\alpha$ line (5.9 keV). Even though the great peak at low energies vanishes, the K_α tail still exists.

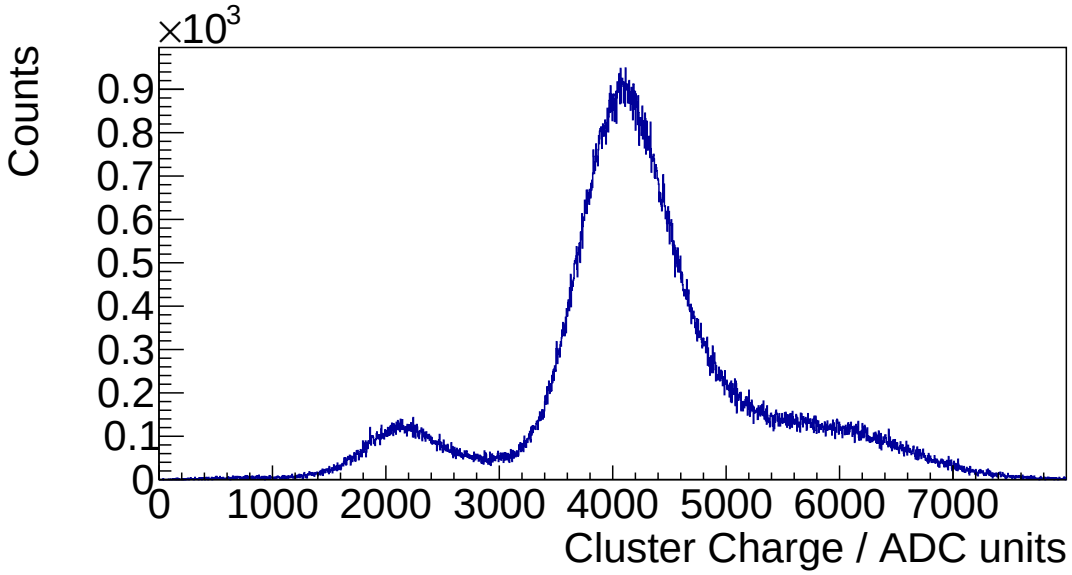

Figure 4.2.: This plot presents the spectrum of ^{55}Fe after the multihit reconstruction. The cluster charge is calculated by adding up the single pad charges of three pad clusters. The pad charge is the sum of the ADC values of every sample.

In order to analyze this branch, the blurring ^{55}Fe peak is fit by the addition of two Gaussian functions. Therefore, the peak as well as the tail are individually fit by Gaussians (red and green) whose parameters are taken for the double Gauss (black) (figure 4.3). The results of the fit parameters are listed in the appendix in table A.1.
The resulting mean of the tail has an ADC value of 5376 corresponding to a converted energy of 7.85 keV. It does not match with the ^{55}Fe K$_\beta$ line (6.4 keV) or any other physical expected particle. In order to understand the origin of the branch, the clusters contributing to the 'normal' spectrum (< 5000 ADC) and cluster contributing to higher ADC values are investigated.
Figure 4.4 pictures the hit types in dependence of the geometrical pads of three pad clusters with an integrated charge > 5000 ADC in (a) and with a charge < 5000 ADC in (b). Both distributions look very similar and do not provide a way to characterize the clusters carrying a high charge.

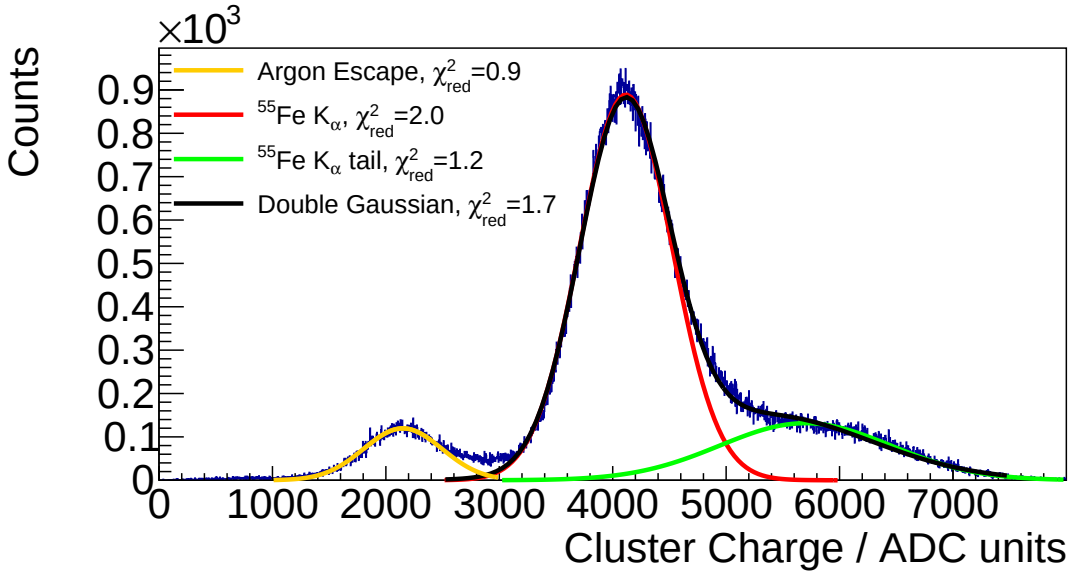

Figure 4.3.: This plot presents the spectrum of ^{55}Fe after the multihit reconstruction. The cluster charge is calculated by adding up the single pad charges of three pad clusters. The pad charge is the sum of the ADC values of every sample. Three individual Gaussians (yellow, red, green) and a double Gaussian (black) are fit. The results of the fit parameters are listed in the appendix in table A.1.

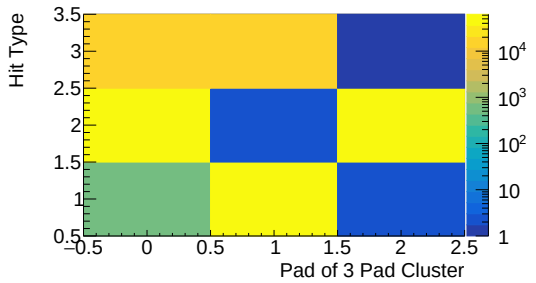

(a) Cluster charge $>$ 5000 ADC

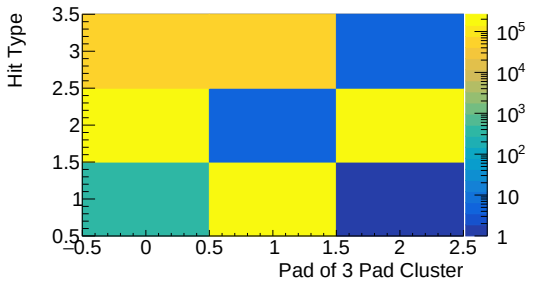

(b) Cluster charge $<$ 5000 ADC

Figure 4.4.: These plots outline the hit types of the pads of three pad clusters with an integrated cluster charge $>$ 5000 ADC (a) or $<$ 5000 ADC (b). On the x-axis 0 is the left pad, 1 the middle pad and 2 the right pad of a cluster.

However, it is unusual that so many constructed three pad clusters contain pads with hit type 3, which means STR and FNR at the same time. A correct constructed three pad cluster should always contain exactly one STR pad in the middle (pad 1) and two FNR pads on the edges (pad 0 and 2), which applies for most of the clusters. A hit type 3 pad is an evidence for a four pad cluster, where the outer pads are FNR and the two inner pads have the hit type 3.
This statement is verified by the PRF of these two different cluster types pictured in figure 4.5. In the case of correct clusters (one STR, two FNR pads) (a) the PRF looks like a normal three pad PRF with two pad borders at -0.5 and 0.5 and the main charge deposit on the middle pad. In contrast to that, the PRF of incorrect clusters (b) appears like a typical four pad PRF with three pad edges at -1, 0 and 1, the main charge between the two middle pads and a missing pad on the right. Thus, these incorrect clusters are cut four pad cluster which were not handled correctly by the *Clusterizer*.

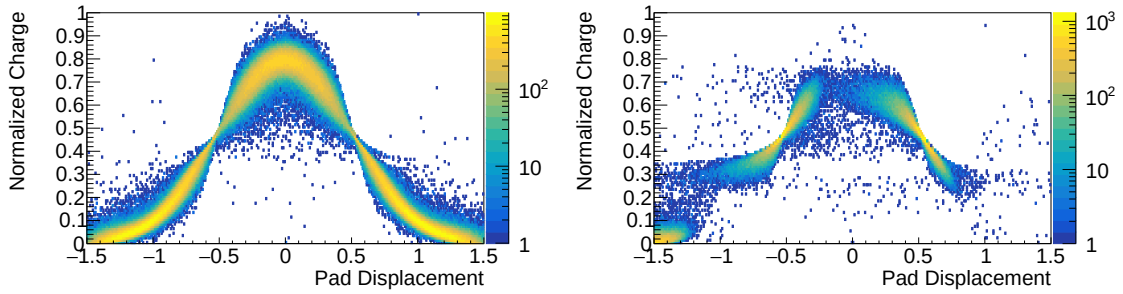

(a) Three pad cluster with one STR and two FNR pads

(b) Other three pad clusters

Figure 4.5.: These plots picture the PRF's of two types of three pad clusters. In (a) the cluster contain two FNR and one STR pad whereas in (b) they consist of any other set of triggered pads.

However, expecting the same particle to hit the detector in the middle of a pad creating a three pad cluster or between two pads creating a four pad cluster, the same charge is distributed over three or four pads. Assuming a fragmented four pad cluster, the remaining three pads contain less charge than a normal three pad cluster. Thus, the identified fragmented four pad clusters do not contribute to the spectrum tail at high ADC units. Instead they should lead to lower charge entries.
Investigations on clusters with different charges can be observed in figure 4.6 where (a) contains all PRF's of clusters with an integrated charge > 5000 ADC and (b) all PRF's of clusters with charges < 5000 ADC. The PRF's shape is almost the same for high and low cluster charges, representing a well defined

three pad PRF with a slight blur on the left pad, resulting from incorrect clusters as in figure 4.5(b).

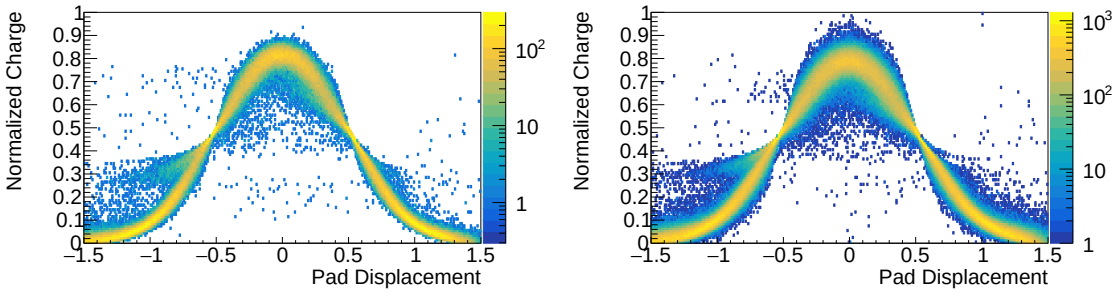

(a) Cluster charge > 5000 ADC (b) Cluster charge < 5000 ADC

Figure 4.6.: The figures present the PRF's of three pad cluster with an integrated cluster charge > 5000 ADC (a) or < 5000 ADC (b).

Even if these results intend that the tail of the constructed spectrum does not originate from any artifacts of the readout electronics or the analysis algorithm, but from real events, the character of the tail changes with different spectrum reconstruction algorithms. Figure 4.7 shows three spectra of the same measurement but with different charge calculations, where the maximum ADC value of each pulse shape, or additionally its two or four adjacent samples, are defined as pad charge.
In all three reconstructions the tail is still existent but its energy varies dependent on the amount of samples used for the charge calculation (table 4.1). A rising number of samples affecting the reconstruction, shifts the tail to higher energies. Thus, every sample of the pulses contributing to high charge clusters, is shifted by a certain ADC value.

Table 4.1.: This table contains the positions of the three peaks of the ^{55}Fe spectrum as well as the resulting energy of the iron K_α tail for different spectrum reconstructions.

Reconstruction	Ar K_α μ [ADC]	^{55}Fe K_α μ [ADC]	Tail μ [ADC]	Tail μ [keV]
MaxADC 1 Sample	171	327	384	7.00
MaxADC 3 Sample	484	962	1147	7.06
MaxADC 5 Sample	776	1534	1838	7.10
Integral	2148	4103	5376	7.85

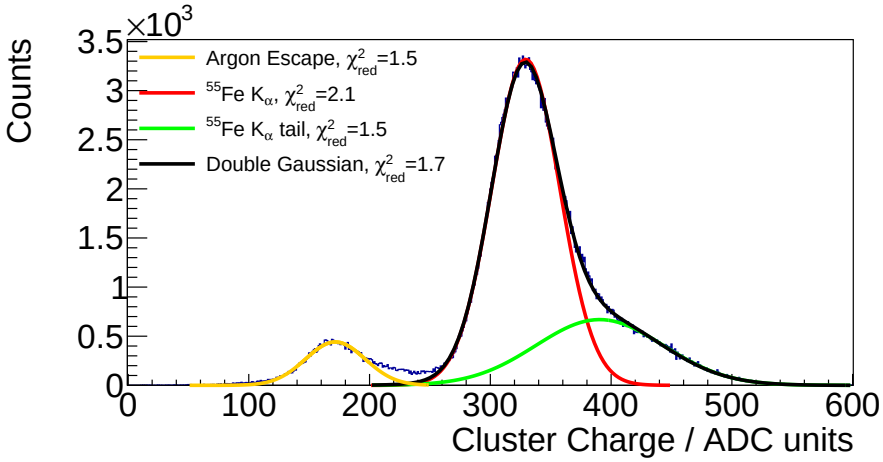

(a) Max. ADC as pad charge

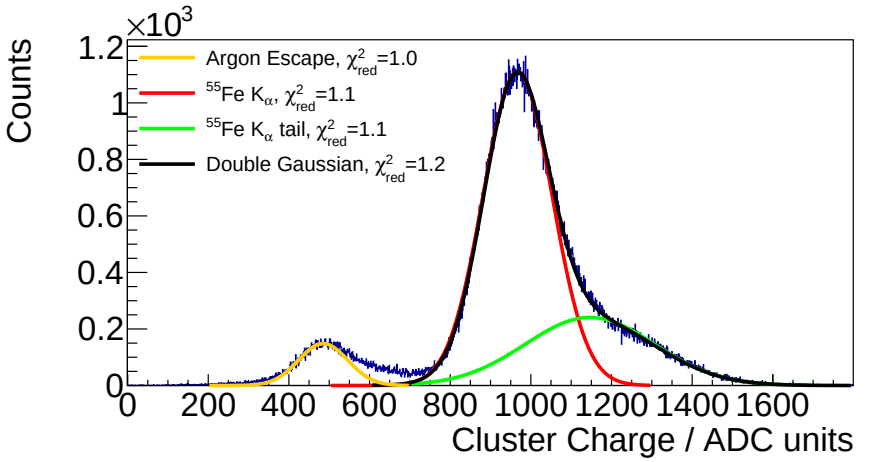

(b) Max. ADC and two adjacent samples

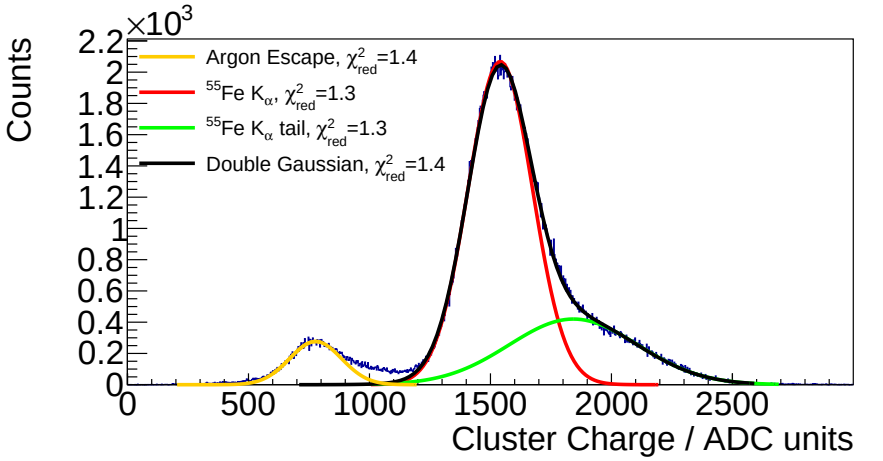

(c) Max. ADC and four adjacent samples

Figure 4.7.: These plots present different spectra of ^{55}Fe after the multihit reconstruction. The cluster charge is calculated by adding up the single pad charges of three pad clusters. The pad charge is calculated in three different ways as mentioned below the graphs. Three individual Gaussians (yellow, red, green) and a double Gaussian (black) are fit. The results of the fit parameters are listed in the appendix in table A.1.

This can also be observed by looking at the corresponding pulse shapes in figure 4.8 picturing the pulse shapes of the clusters with an integral charge higher or lower 5000 ADC. Latter pulses tend to have a longer tail and do often not end in the baseline. They do not end after 32 samples, but take a longer time to fall to the zero level again. Therefore, these pulses influence the spectrum reconstruction based on the amount of samples used for the pad charge calculation: the more samples are taken into account, the bigger the influence and hence the resulting energy of the spectrum blur. Discarding all these pulses leads to a spectrum without the K_α tail as pictured in figure 4.9. In this case a cut was applied, where only pulses ending in the baseline (under the ADC value 20 after baseline correction), contribute to the spectrum.
All pulses should usually end within the 32 samples, so nothing of the generated pulse is lost. However, pulses with a large charge deposition exceed this recording range leading to an inaccurate charge reconstruction.

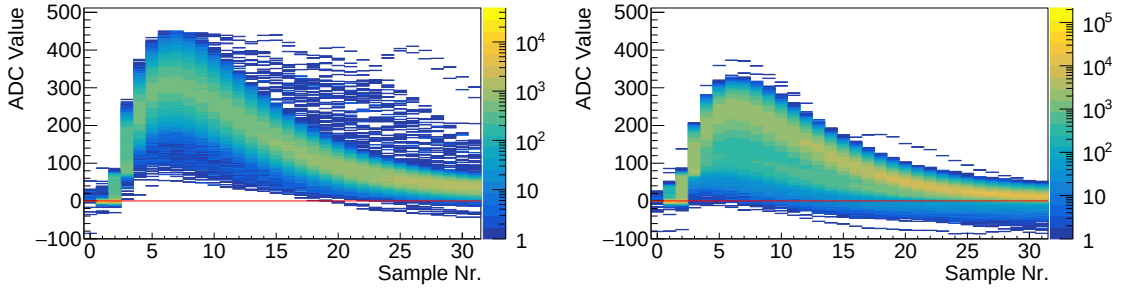

(a) Cluster charge > 5000 ADC (b) Cluster charge < 5000 ADC

Figure 4.8.: The plots reveal all STR pulse shapes of clusters with an integrated cluster charge > 5000 ADC (a) or < 5000 ADC (b).

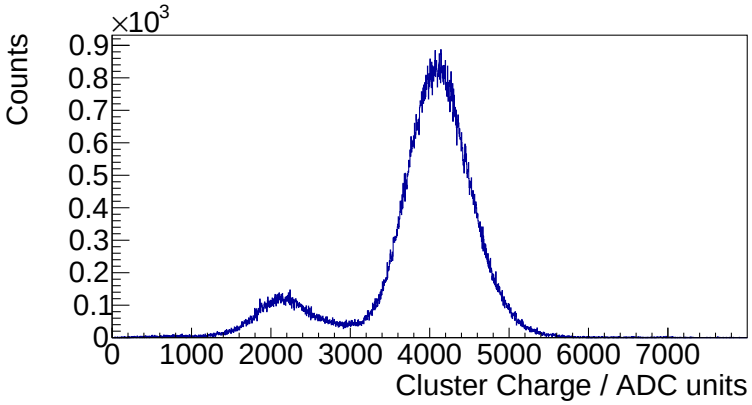

Figure 4.9.: This plot presents the spectrum of ^{55}Fe after the multihit reconstruction. The cluster charge is calculated by adding up the single pad charges of three pad clusters. The pad charge is the sum of the ADC values of every sample. In addition, all pulses not ending in the baseline (under the ADC value 20 after baseline correction) were discarded before the reconstruction.

4.2. ^{55}Fe Energy Resolution Investigations

Measuring the dependency of the energy resolution on the anode voltage, pictured in figure 4.10, provides information about the measurement quality and the optimal operating point of the TRD. Furthermore, in order to minimize the real time data flow of the SPADIC in the experiment it is of interest not to read out every single sample of the pulse shape. Therefore, the energy resolution is additionally investigated dependent on four different spectrum reconstruction algorithms. In all of them the cluster charge is summed over the single pads, while the pad charge is defined via: the sum of all samples, the maximum ADC value or additionally the sum over the maximum ADC value and its two or four adjacent samples.
The measurements providing these data were conducted with the differential thresholds $\mathrm{Th}_1 = \mathrm{Th}_2 = 10$ and a recording time of $\sim 10\,\mathrm{min}$. The resulting spectra are listed in the appendix in figures A.7-A.12. They are fit like the spectra in chapter 4.1, so the addition of two Gauss functions is fit to the K_α peak and its tail. The mean and standard deviation of this double Gaussian regarding the K_α line is used for the energy resolution defined as σ/μ.

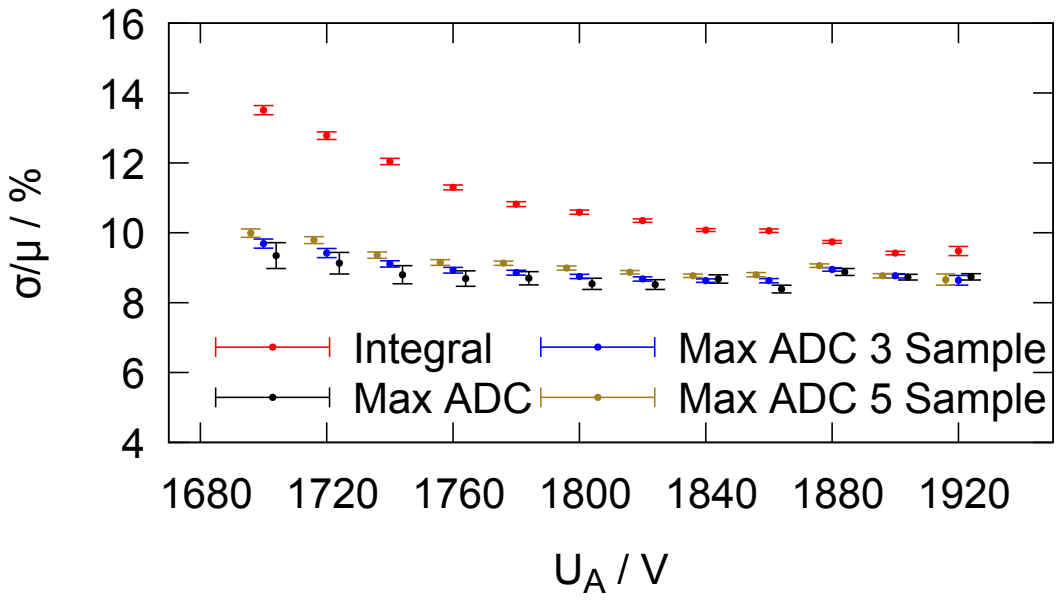

Figure 4.10.: This graph shows the energy resolution σ/μ of the K_α line in depedency of the U_A. Data points for different reconstruction mechanisms are plotted: taking the sample with the highest ADC value of a pulse shape as pad charge; the maximum ADC sample and its two adjacent samples; the maximum ADC sample and its four adjacent samples; the sum of all 32 samples.

In order to estimate the systematical error of the different reconstruction techniques, the electrical noise of the SPADIC has to be investigated. A measurement without any radioactive source is conducted triggering the SPADIC via the external trigger. This leads to the recording of samples in the baseline, whose Gaussian distribution with a deviation of $\sigma = 3.6 \approx 4\,\text{ADC}$ is pictured in figure 4.11. This deviation is defined as the ADC fluctuation so every sample has a systematical error of 2 ADC.

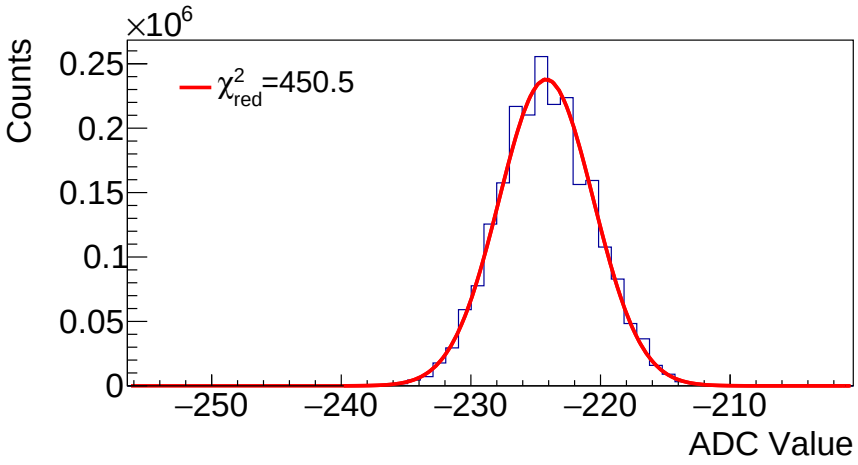

Figure 4.11.: This plot shows the distribution of the SPADIC baseline represented by every recorded sample of a measurement without radioactive source. A Gaussian is fit to the data with the parameters $\mu = -224.19 \pm 0.01$ and $\sigma = 3.64 \pm 0.01$.

If only the highest sample of a pulse is taken as pad charge, the phase shift of a pulse shape has to be considered as well. Since a real physical event happens at any time but the ADC samples are created at discrete timestamps in a time difference of 62.5 ns, a pulse is not always sampled at the same time. Thus, the real maximum of a pulse is not always sampled, so the sample of the highest value can be shifted to the maximum (figure 4.12). The maximal difference of the highest ADC value to the actual amplitude of the pulse can be calculated via the pulse shape

$$\begin{aligned} f(t) &= A \cdot \frac{t}{\tau} \cdot \exp\left(-\frac{t}{\tau}\right) \\ &= 1223 \cdot \frac{t}{240\,\text{ns}} \cdot \exp\left(-\frac{t}{240\,\text{ns}}\right) \end{aligned} \tag{4.1}$$

which is the SPADIC pulse shape with a definite shaping time of 240 ns and A set, so a maximal high pulse with the amplitude $f_{max} = 450\,\text{ADC}$ results. The maximum phaseshift is half a time stamp, 31.25 ns, leading to the sample

values $S_1 = 445.75 \approx 445\,\text{ADC}$ in the case of the sample before the maximum and $S_2 = 446.42 \approx 446\,\text{ADC}$ in the case of the sample after the maximum. Due to the identification of the maximum ADC at 446 ADC, the error of the determination of the maximum ADC sample, due to phase shift, is 4 ADC.
Altogether, the systematical errors for the reconstructed pad charges are calculated by the Gaussian error propagation. Every sample contributing to the pad charge has the uncertainty of half of the ADC fluctuation ($4\,\text{ADC}/2 = 2\,\text{ADC}$) while the phaseshift of 4 ADC additionally comes into play if the maximum ADC sample is defined as pad charge. Thus, the systematical errors are $11.3 \approx 12\,\text{ADC}$ in the case of an integral, $4.5 \approx 5\,\text{ADC}$ for the maximum ADC sample and $3.5 \approx 4\,\text{ADC}$ or $4.5 \approx 5\,\text{ADC}$ for the sum of the three or five maximum ADC samples.
The energy resolution (figure 4.10) shows a falling trend with higher anode voltage for every charge reconstruction. This indicates better energy resolutions with higher operating voltage. However, measurements can not be conducted with any high anode voltage due to the clipping of the measured pulses. The operating point should be chosen in a way that all expected events fit into the ADC range while a higher anode voltage provides better results.
Furthermore, the energy resolution improves with less samples contributing to the pad charge calculation, since the best results are archived by only taking the maximum ADC value of a pulse shape as pad charge.
Overall, energy resolutions in the area of $\frac{\sigma}{\mu} = (8.4 - 13.6)\,\%$ are measured.

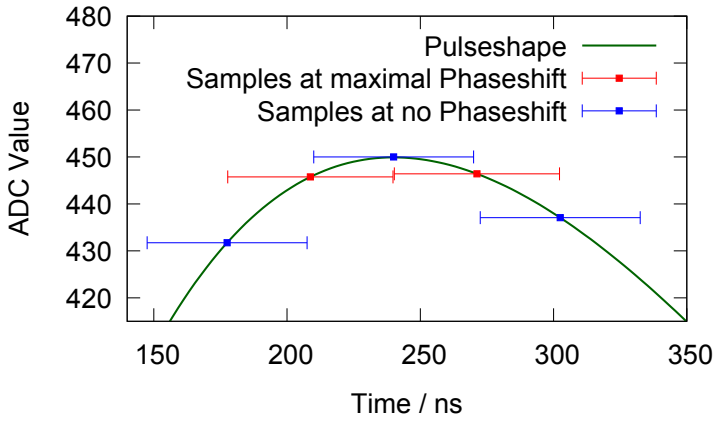

Figure 4.12.: This drawing presents a scheme of the phaseshift of a sampled pulse shape. The green line depicts a maximal high pulse shape (450 ADC) in the area of its maximum while the points picture the samples of two different sampling scenarios. In the blue scenario the maximum ADC value is exactly sampled, so no phaseshift occurs, while the phaseshift is maximal (31.25 ns or 0.5 timestamps) for the red data. In the latter case the maximal sampled ADC value is the right point which is about 4 ADC smaller than the actually pulse amplitude.

5. Conclusions and Outlook

In this elaboration an automated test stand for the CBM-TRD was constructed. The functionality of the whole setup, including a precision table mounted in front of the MWPC installed with its DAQ, was confirmed by several measurements. The gas gain of the MWPC as well as the gain matching was successfully tested enabling energetically resolved measurements in an appropriate ADC regime.
Furthermore, the analysis software of the CBM-TRD was enhanced by the hit reconstruction. Fragmented hits, so called multihits, were analyzed revealing the multimessage characteristics: a single hit can trigger the electronics twice, if a FNR pad has enough charge deposition to fulfill the trigger condition a second time a few timestamps after the STR pad. This leads to a stop of the readout of these two pads followed by a new readout of a three pad cluster with the initial FNR pad as middle STR pad and the initial STR pad as FNR pad. Avoiding the resulting readout of two individual hits can lower the transmitted data rate in later experiments. This can be realized e.g. by a protection time of the SPADIC in such way that a second trigger of the same pad after a short time is prevented.
These analysis lead to the implementation of the multihit reconstruction algorithm including the correction of real physical multihits by fitting the incomplete predecessor and correcting the successor with the predecessor. Multimessages, identified as multihits with less than five samples, are compounded to one pulse.
A spectrum of the ^{55}Fe source was reconstructed by adding up the samples of a single pad to the pad charge and adding up the resulting pad charges to the charge of three pad clusters. Without the implemented multihit reconstruction this spectrum reveals the desired argon escape peak and the ^{55}Fe K_α line but additionally many entries at low ADC values (proportional to energy) and a tail of the K_α peak to higher ADC values. By applying the multihit reconstruction the entries at low energies vanish. However, the branch at high energies remains leading to further analysis. Since the characteristics of this tail vary dependent on the anode voltage and on the spectrum reconstruction, it does not originate from other detected particles apart from the argon escape and the iron K_α photons. The tend to higher energies with a rising amount of samples included in the pad charge reconstruction leads to the conclusion that the tail is an artifact of the reconstruction mechanism or results from characteristics of the readout

electronics. The pulses of clusters contributing to entries at high ADC values are most likely ending above the baseline and do not end within the time window of 32 timestamps. Furthermore, the tail disappears if all pulses not ending in the baseline are discarded. Hence, pulses with a large deposition do not end in the recording time of the electronics, resulting in an incorrect charge reconstruction. One reason for this phenomena can be the long shaping time of the SPADIC 2.0 of 240 ns. Upcoming SPADIC versions are already designed with a shorter shaping time. Nevertheless, more investigations regarding the origins of the long pulses have to be done.
Nevertheless, investigations of the energy resolution were conducted with the branch included in the spectrum. The K_α peak as well as the tail can be described by Gaussian functions such that both of them are fit by a double Gauss. The resulting K_α energy resolution (σ/μ) was calculated for different spectrum reconstructions varying in the amount of samples taken as pad charge. Overall the resolution improves with higher anode voltages. Furthermore, the less samples are involved in the pad charge the better is the energy resolution, down to $\sigma/\mu = 8.4\,\%$. This result was archived by taking the maximum ADC value of a pulse as the pad charge. However, even if a higher anode voltage seems to result in a better measurement quality it can not be adjusted too high due to clipping pulses exceeding the ADC range. Since every expected particle is desired to be reliably measured, it should fit within the ADC range. Thus, the gas gain should be adjusted, so the ^{55}Fe K_α photons cover a certain area of the ADC as calculated in chapter 3.2. At the resulting operating voltage of 1790 V energy resolutions of $\sim 8.5\,\%$ were obtained in this work.
Overall, the MWPC test stand was successfully tested with measurement resulting in satisfying ^{55}Fe spectra.

A. Appendix

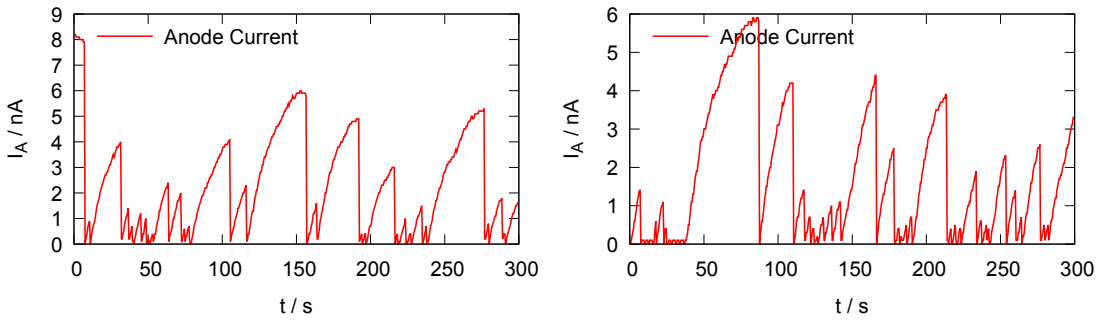

(a) $U_A = 1600\,\mathrm{V}$

(b) $U_A = 1625\,\mathrm{V}$

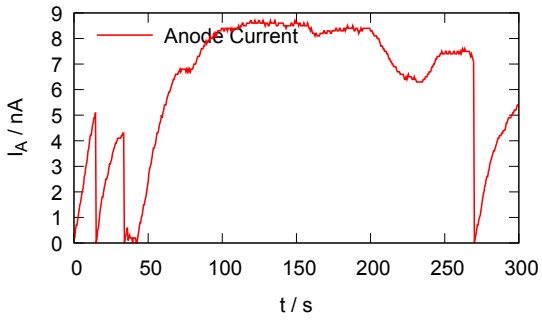

(c) $U_A = 1650\,\mathrm{V}$

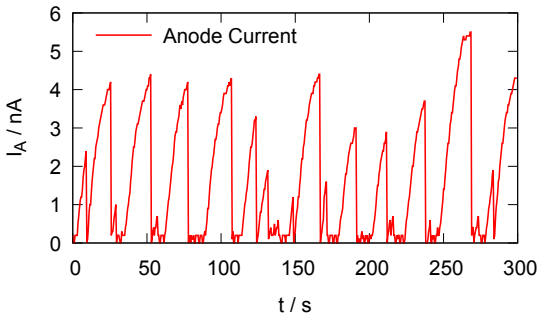

(d) $U_A = 1675\,\mathrm{V}$

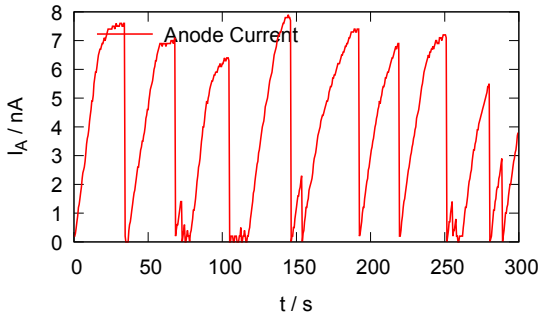

(e) $U_A = 1700\,\mathrm{V}$

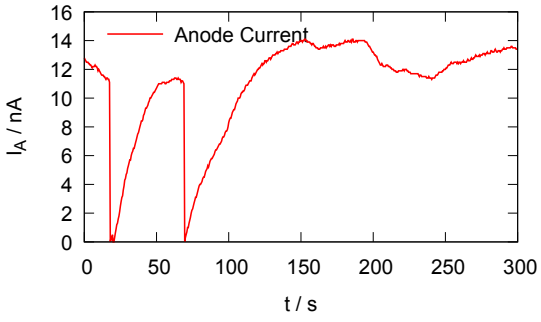

(f) $U_A = 1725\,\mathrm{V}$

Figure A.1.: This diagram pictures the anode current as a function of time for different anode voltages U_A, measured by the MPOD with a readout frequency of 2 Hz.

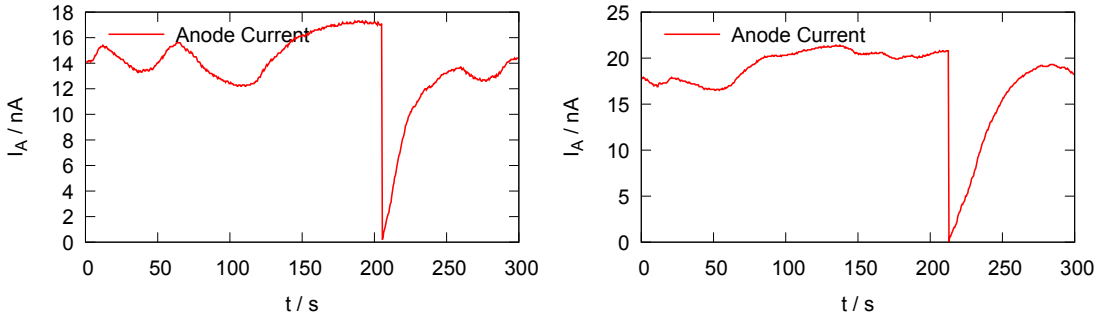

(a) $U_A = 1750\,\mathrm{V}$

(b) $U_A = 1775\,\mathrm{V}$

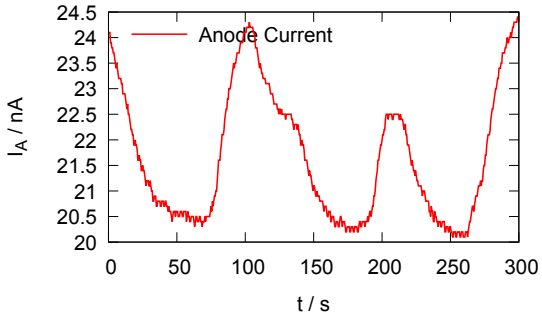

(c) $U_A = 1800\,\mathrm{V}$

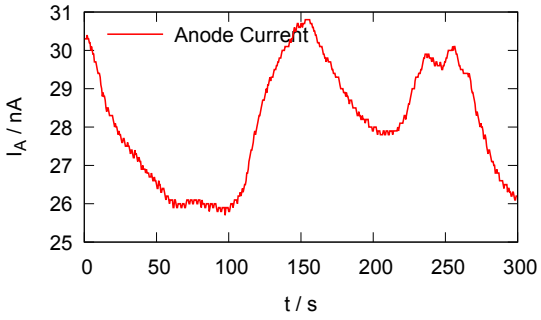

(d) $U_A = 1825\,\mathrm{V}$

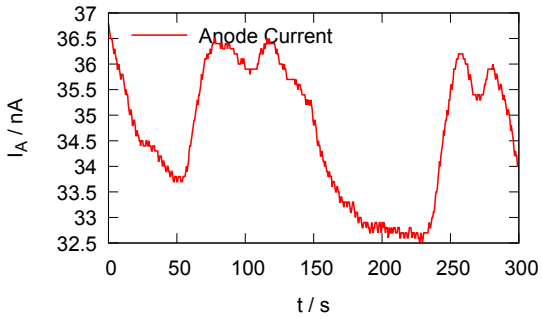

(e) $U_A = 1850\,\mathrm{V}$

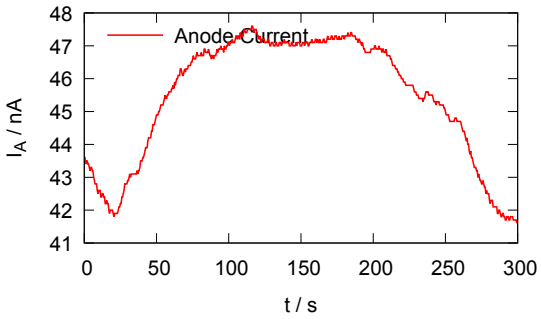

(f) $U_A = 1875\,\mathrm{V}$

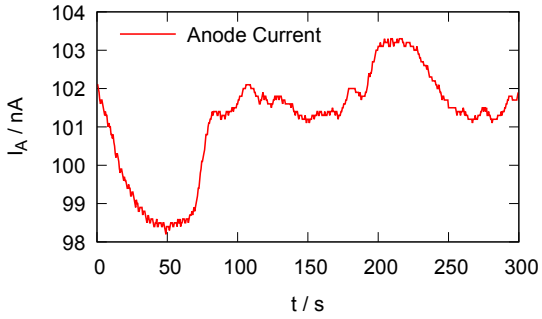

(g) $U_A = 1975\,\mathrm{V}$

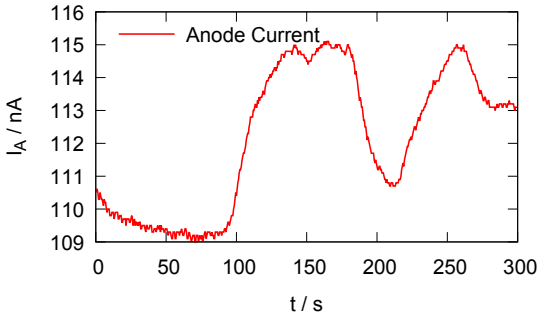

(h) $U_A = 1987\,\mathrm{V}$

Figure A.2.: This diagram pictures the anode current as a function of time for different anode voltages U_A, measured by the MPOD with a readout frequency of 2 Hz.

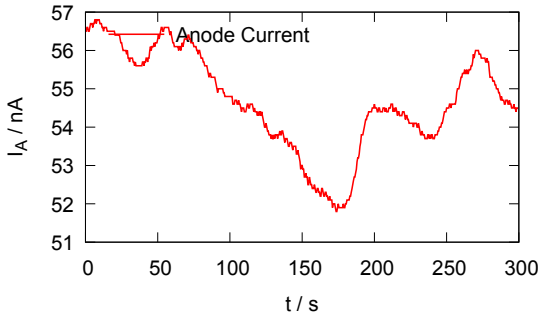

(a) $U_A = 1900\,\mathrm{V}$

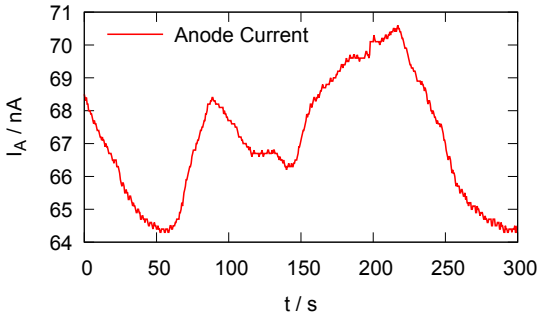

(b) $U_A = 1925\,\mathrm{V}$

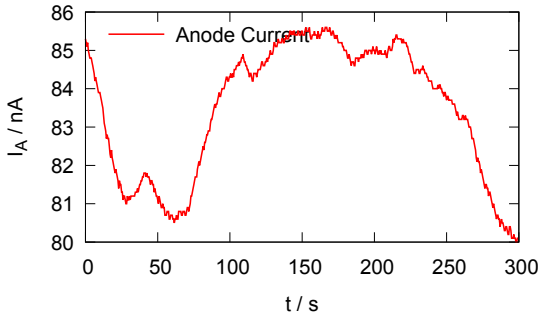

(c) $U_A = 1950\,\mathrm{V}$

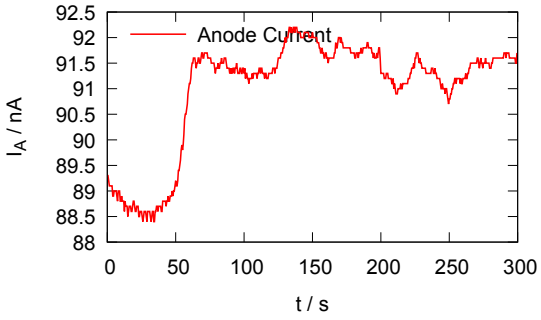

(d) $U_A = 1962\,\mathrm{V}$

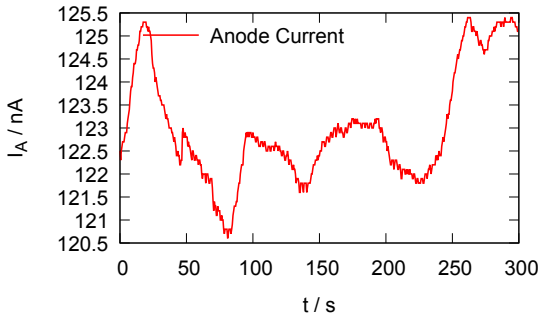

(e) $U_A = 2000\,\mathrm{V}$

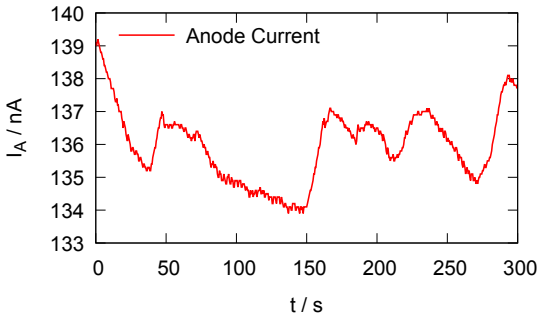

(f) $U_A = 2012\,\mathrm{V}$

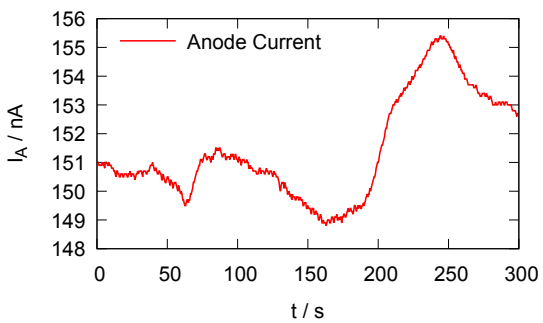

(g) $U_A = 2025\,\mathrm{V}$

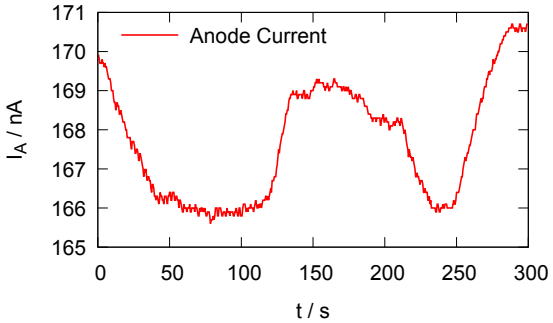

(h) $U_A = 2037\,\mathrm{V}$

Figure A.3.: This diagram pictures the anode current as a function of time for different anode voltages U_A, measured by the MPOD with a readout frequency of 2 Hz.

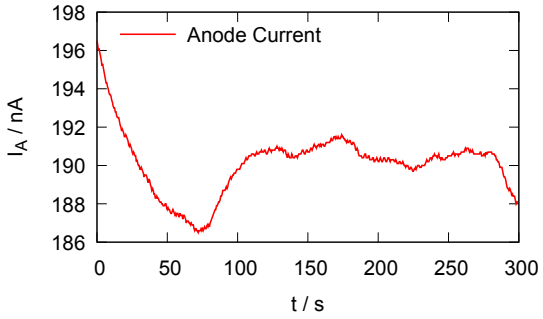

(a) $U_A = 2050\,\mathrm{V}$

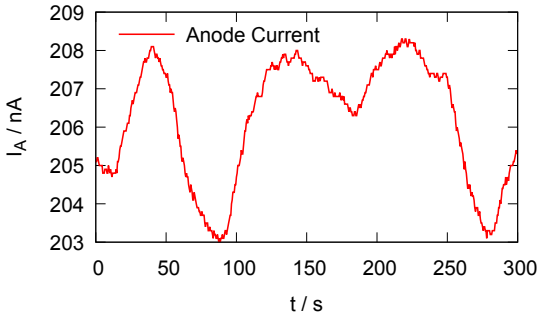

(b) $U_A = 2062\,\mathrm{V}$

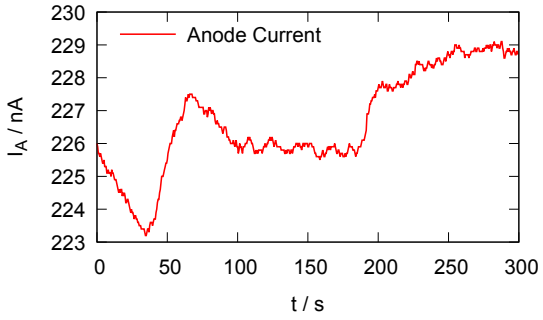

(c) $U_A = 2075\,\mathrm{V}$

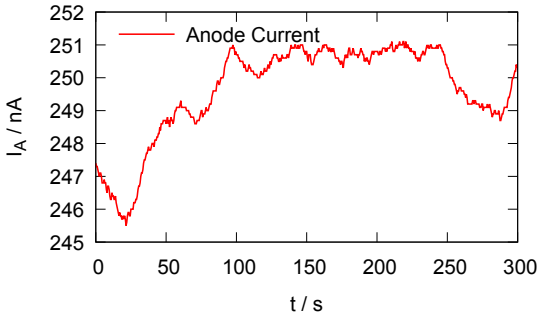

(d) $U_A = 2087\,\mathrm{V}$

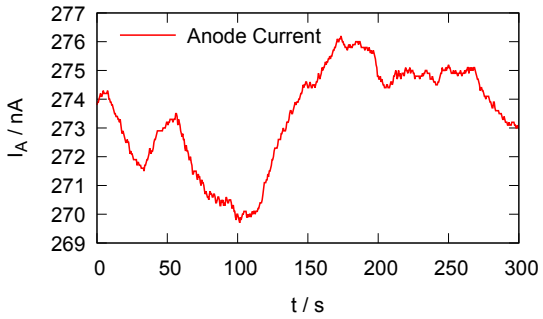

(e) $U_A = 2100\,\mathrm{V}$

Figure A.4.: This diagram pictures the anode current as a function of time for different anode voltages U_A, measured by the MPOD with a readout frequency of 2 Hz.

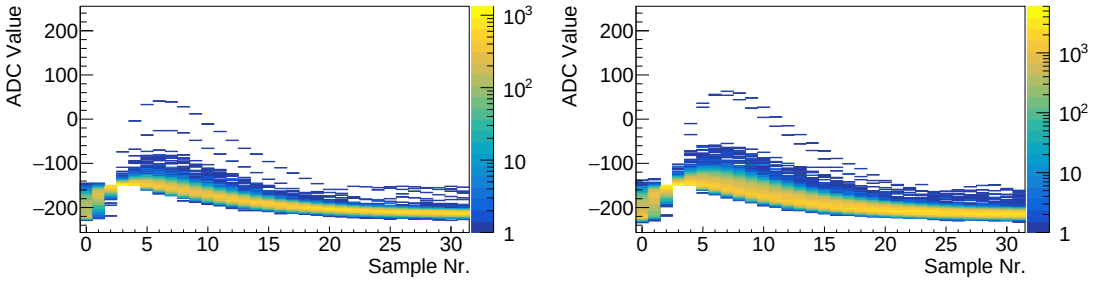

(a) $U_A = 1650\,\mathrm{V}$

(b) $U_A = 1675\,\mathrm{V}$

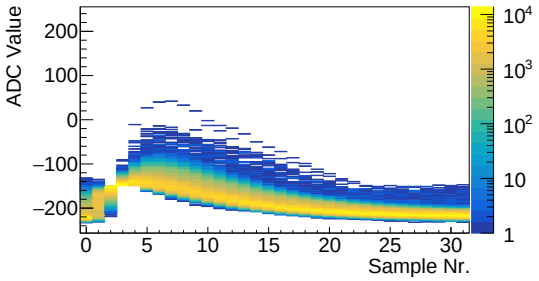

(c) $U_A = 1700\,\mathrm{V}$

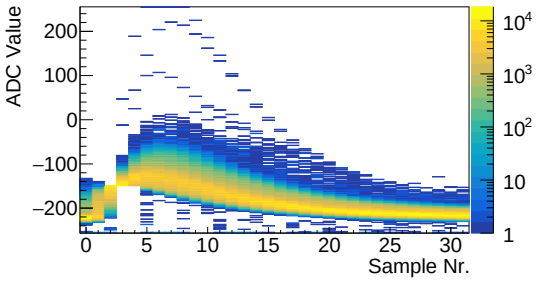

(d) $U_A = 1725\,\mathrm{V}$

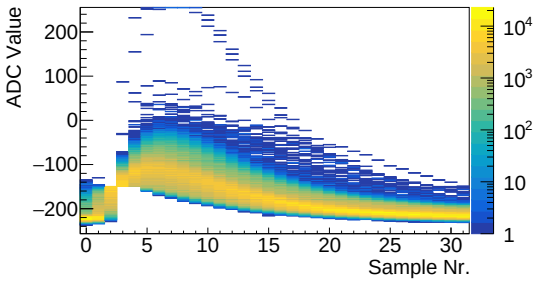

(e) $U_A = 1750\,\mathrm{V}$

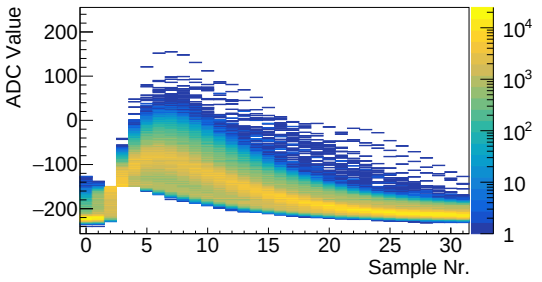

(f) $U_A = 1775\,\mathrm{V}$

Figure A.5.: STR pulse shapes (ADC value as a function of the time represented by the sample nr.) of one SPADIC channel at $U_A = 1850\,\mathrm{V}$ are pictured. Both thresholds are set absolute to -150 ADC.

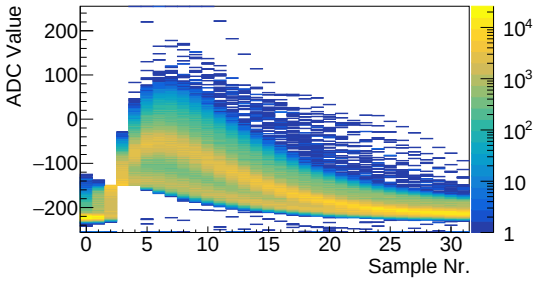

(a) $U_A = 1800\,\mathrm{V}$

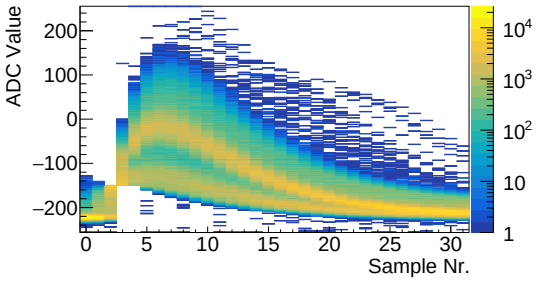

(b) $U_A = 1825\,\mathrm{V}$

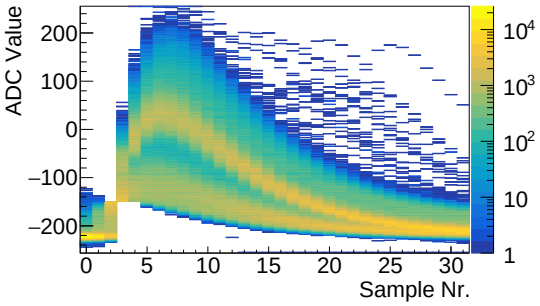

(c) $U_A = 1850\,\mathrm{V}$

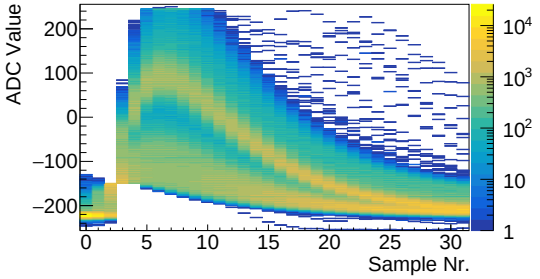

(d) $U_A = 1875\,\mathrm{V}$

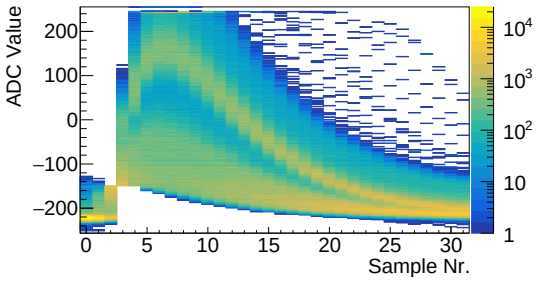

(e) $U_A = 1900\,\mathrm{V}$

Figure A.6.: STR pulse shapes (ADC value as a function of the time represented by the sample nr.) of one SPADIC channel at $U_A = 1850\,\mathrm{V}$ are pictured. Both thresholds are set absolute to -150 ADC.

Table A.1.: This list contains the fit results and energy resolutions of different reconstructed spectra recorded at 1850 V.

	Ar escape		^{55}Fe K_α		^{55}Fe K_α tail	
Reconstruction	μ	σ	μ	σ	μ	σ
Integral	2149.69 ± 6.67	345.08 ± 12.72	4115.93 ± 1.84	406.76 ± 1.44	5698.55 ± 16.97	756.24 ± 9.44
Max ADC	171.67 ± 0.27	24.66 ± 0.41	329.33 ± 0.11	28.14 ± 0.12	390.48 ± 3.50	52.75 ± 1.13
Max ADC 3 Sample	484.99 ± 3.25	60.81 ± 2.91	967.05 ± 0.38	85.51 ± 0.53	1146.40 ± 18.03	160.41 ± 5.14
Max ADC 5 Sample	777.26 ± 5.22	106.83 ± 3.87	1540.55 ± 0.73	133.26 ± 0.70	1842.70 ± 8.71	265.72 ± 3.43

	double, ^{55}Fe K_α		double, ^{55}Fe K_α tail	
Reconstruction	μ	σ	μ	σ
Integral	4102.63 ± 1.67	397.76 ± 2.99	5342.06 ± 38.87	931.24 ± 19.80
Max ADC	327.03 ± 0.10	26.67 ± 0.16	385.26 ± 1.64	54.43 ± 0.61
Max ADC 3 Sample	961.85 ± 0.31	80.18 ± 0.42	1146.47 ± 4.36	161.78 ± 1.69
Max ADC 5 Sample	1534.39 ± 0.51	130.61 ± 0.75	1836.35 ± 7.75	267.95 ± 3.03

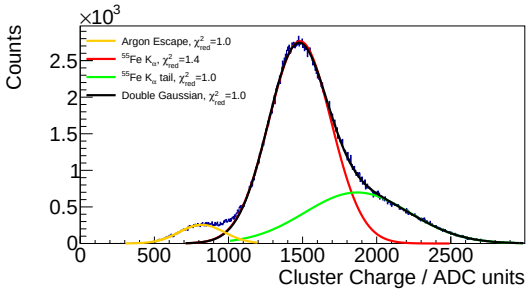

(a) $U_A = 1700\,\mathrm{V}$, integral as pad charge

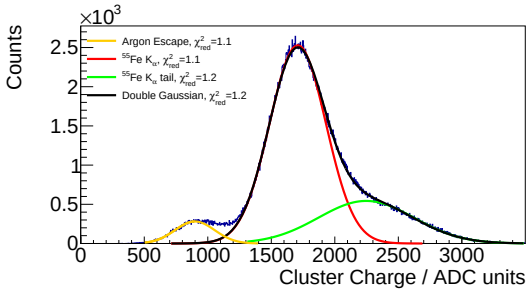

(b) $U_A = 1720\,\mathrm{V}$, integral as pad charge

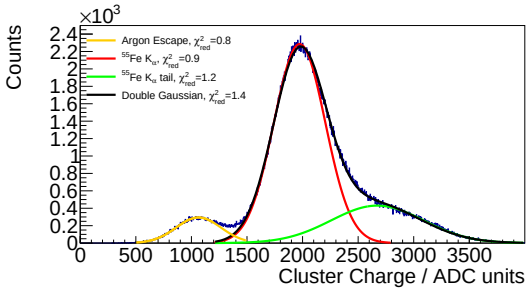

(c) $U_A = 1740\,\mathrm{V}$, integral as pad charge

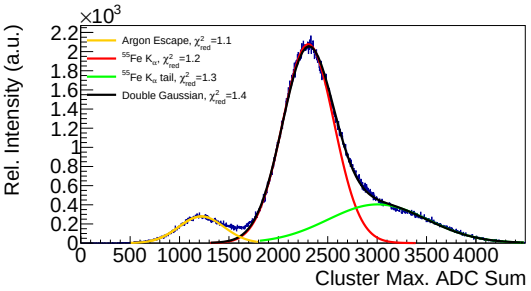

(d) $U_A = 1760\,\mathrm{V}$, integral as pad charge

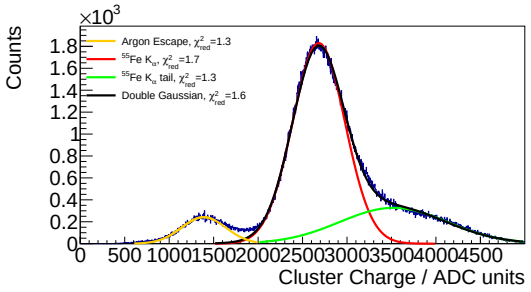

(e) $U_A = 1780\,\mathrm{V}$, integral as pad charge

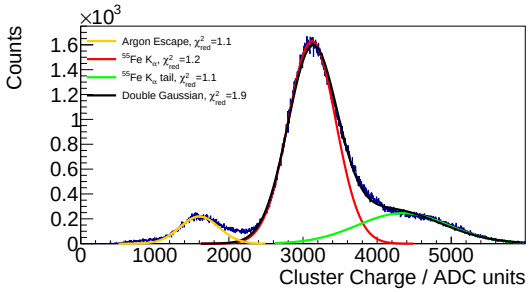

(f) $U_A = 1800\,\mathrm{V}$, integral as pad charge

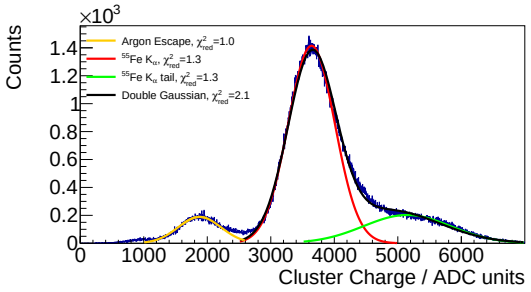

(g) $U_A = 1820\,\mathrm{V}$, integral as pad charge

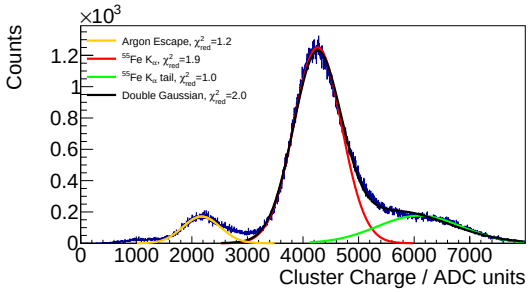

(h) $U_A = 1840\,\mathrm{V}$, integral as pad charge

Figure A.7.: Presented are ^{55}Fe spectra at different anode voltages. The three pad cluster charge is the sum of the pad charge while the pad charge is calculated as explained below the spectra. The fit results can be found in tables A.2 to A.9

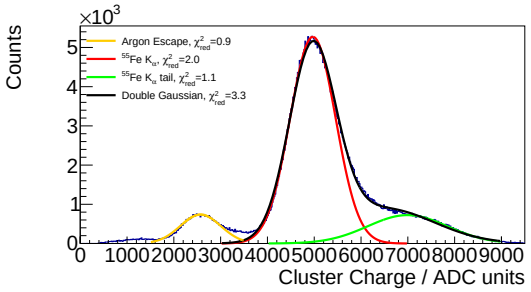

(a) $U_A = 1860\,\mathrm{V}$, integral as pad charge

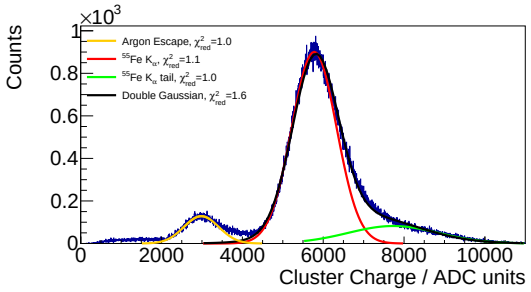

(b) $U_A = 1880\,\mathrm{V}$, integral as pad charge

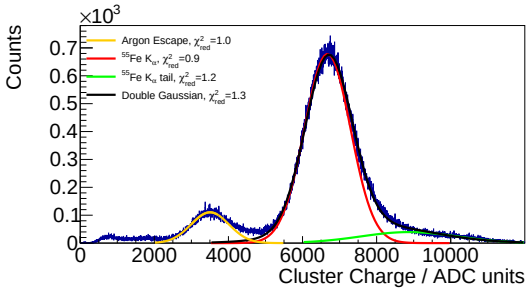

(c) $U_A = 1900\,\mathrm{V}$, integral as pad charge

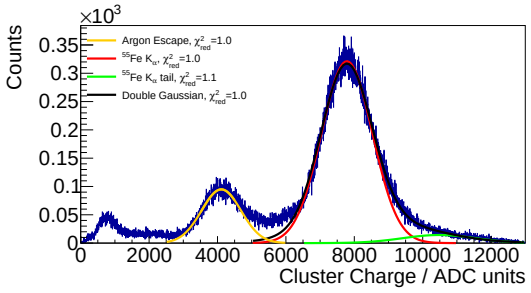

(d) $U_A = 1920\,\mathrm{V}$, integral as pad charge

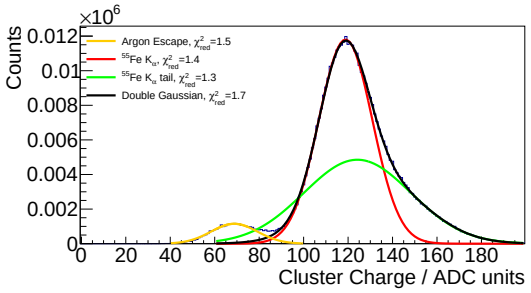

(e) $U_A = 1700\,\mathrm{V}$, max ADC as pad charge

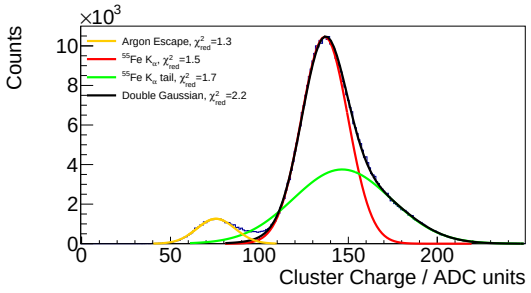

(f) $U_A = 1720\,\mathrm{V}$, max ADC as pad charge

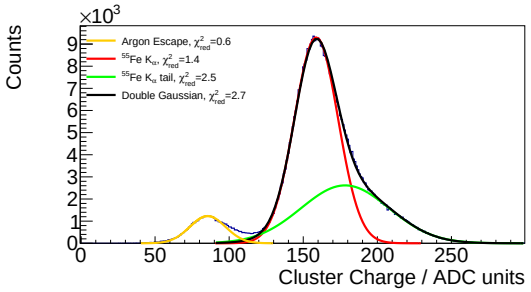

(g) $U_A = 1740\,\mathrm{V}$, max ADC as pad charge

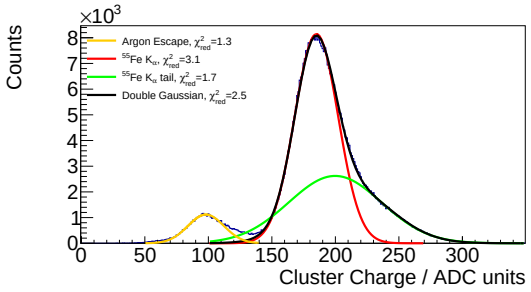

(h) $U_A = 1760\,\mathrm{V}$, max ADC as pad charge

Figure A.8.: Presented are ^{55}Fe spectra at different anode voltages. The three pad cluster charge is the sum of the pad charge while the pad charge is calculated as explained below the spectra. The fit results can be found in tables A.2 to A.9

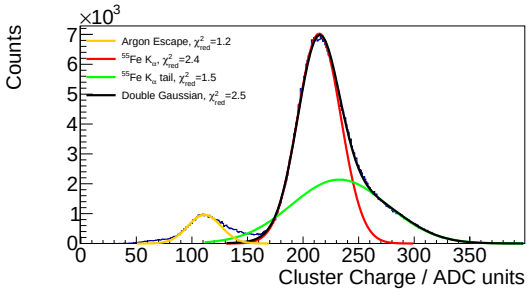

(a) $U_A = 1780\,\mathrm{V}$, max ADC as pad charge

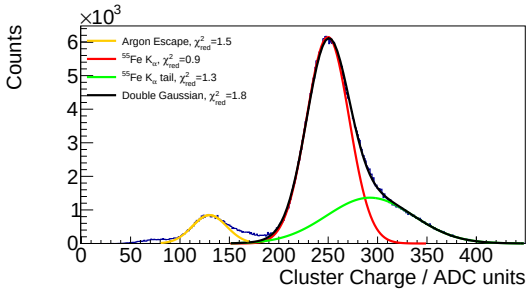

(b) $U_A = 1800\,\mathrm{V}$, max ADC as pad charge

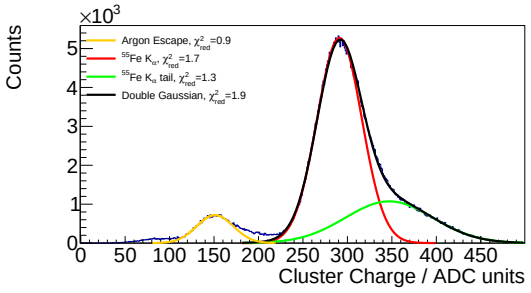

(c) $U_A = 1820\,\mathrm{V}$, max ADC as pad charge

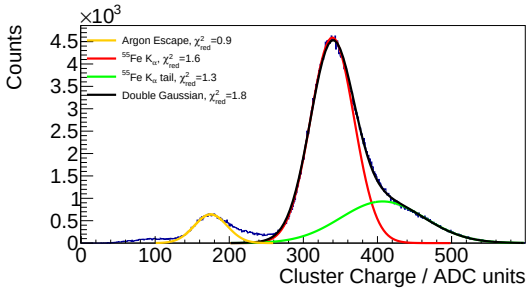

(d) $U_A = 1840\,\mathrm{V}$, max ADC as pad charge

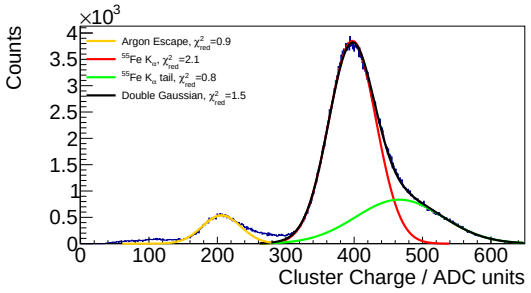

(e) $U_A = 1860\,\mathrm{V}$, max ADC as pad charge

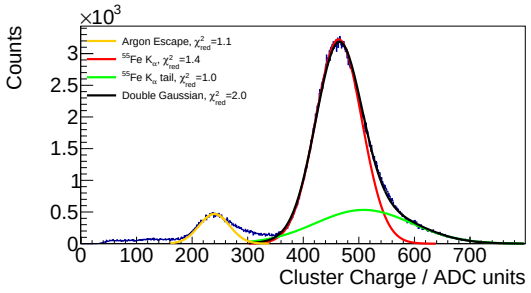

(f) $U_A = 1880\,\mathrm{V}$, max ADC as pad charge

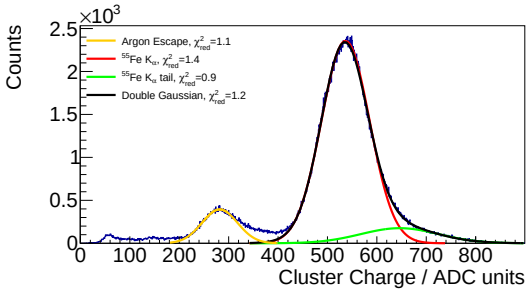

(g) $U_A = 1900\,\mathrm{V}$, max ADC as pad charge

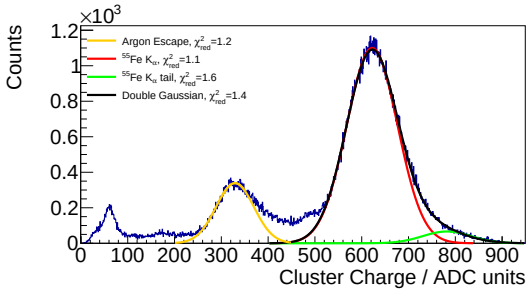

(h) $U_A = 1920\,\mathrm{V}$, max ADC as pad charge

Figure A.9.: Presented are ^{55}Fe spectra at different anode voltages. The three pad cluster charge is the sum of the pad charge while the pad charge is calculated as explained below the spectra. The fit results can be found in tables A.2 to A.9

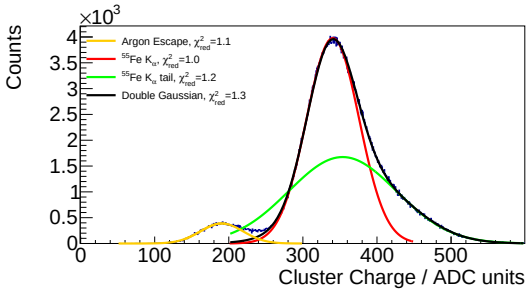

(a) $U_A = 1700\,\mathrm{V}$, max ADC + 2 adjacent samples as pad charge

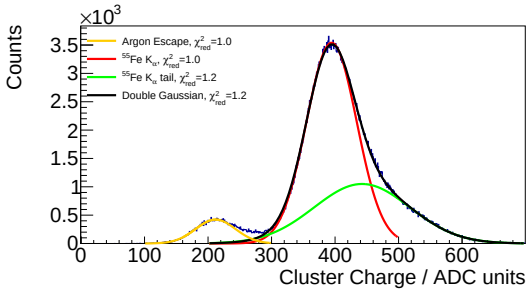

(b) $U_A = 1720\,\mathrm{V}$, max ADC + 2 adjacent samples as pad charge

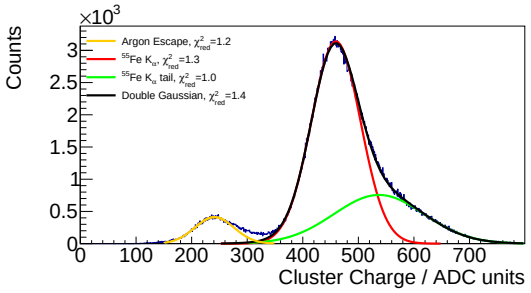

(c) $U_A = 1740\,\mathrm{V}$, max ADC + 2 adjacent samples as pad charge

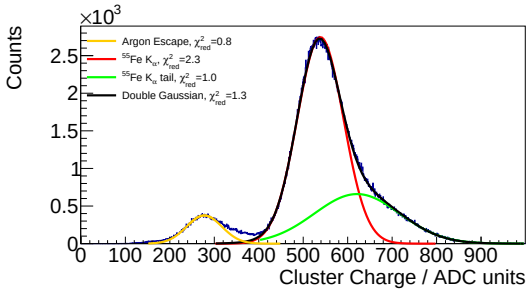

(d) $U_A = 1760\,\mathrm{V}$, max ADC + 2 adjacent samples as pad charge

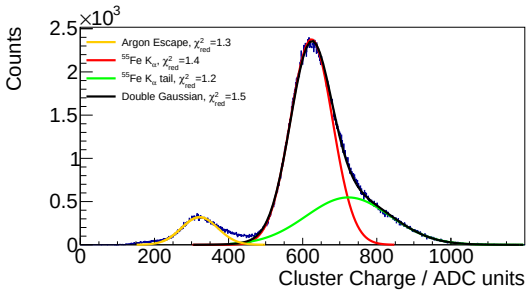

(e) $U_A = 1780\,\mathrm{V}$, max ADC + 2 adjacent samples as pad charge

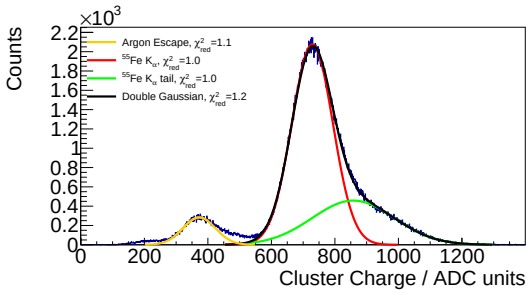

(f) $U_A = 1800\,\mathrm{V}$, max ADC + 2 adjacent samples as pad charge

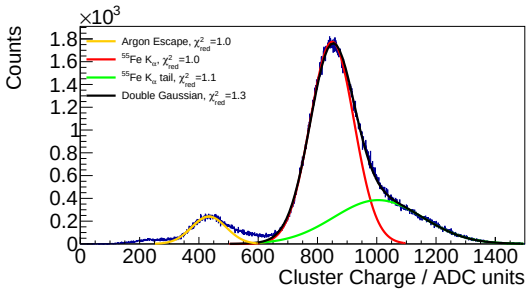

(g) $U_A = 1820\,\mathrm{V}$, max ADC + 2 adjacent samples as pad charge

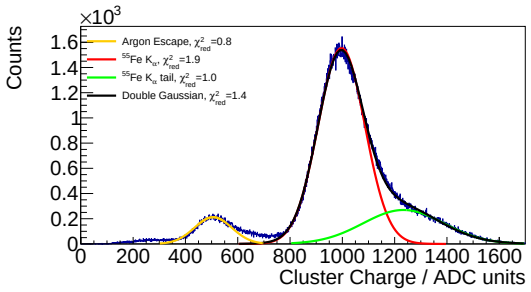

(h) $U_A = 1840\,\mathrm{V}$, max ADC + 2 adjacent samples as pad charge

Figure A.10.: Presented are ^{55}Fe spectra at different anode voltages. The three pad cluster charge is the sum of the pad charge while the pad charge is calculated as explained below the spectra. The fit results can be found in tables A.2 to A.9

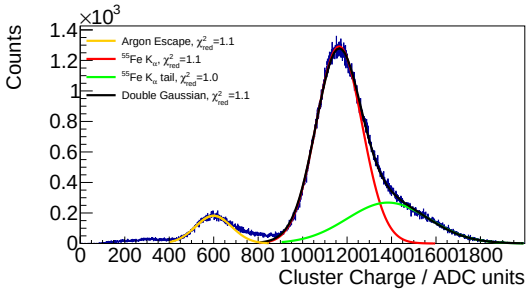

(a) $U_A = 1860\,\mathrm{V}$, max ADC + 2 adjacent samples as pad charge

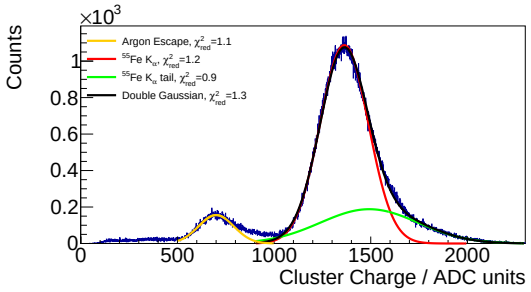

(b) $U_A = 1880\,\mathrm{V}$, max ADC + 2 adjacent samples as pad charge

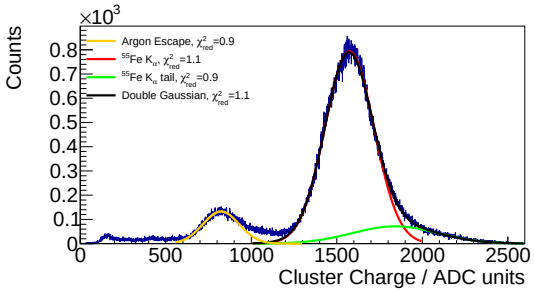

(c) $U_A = 1900\,\mathrm{V}$, max ADC + 2 adjacent samples as pad charge

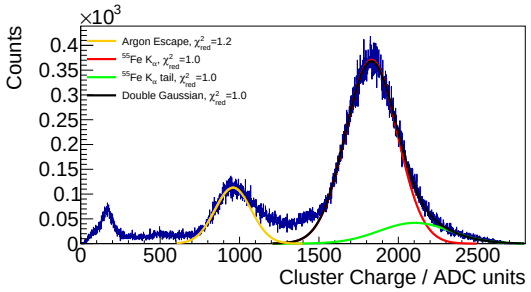

(d) $U_A = 1920\,\mathrm{V}$, max ADC + 2 adjacent samples as pad charge

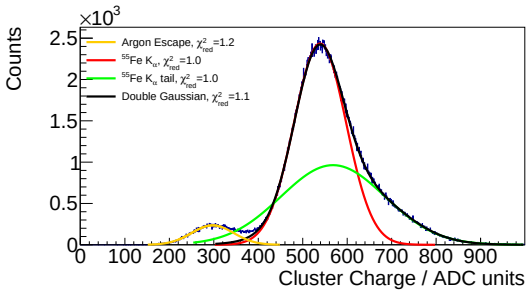

(e) $U_A = 1700\,\mathrm{V}$, max ADC + 4 adjacent samples as pad charge

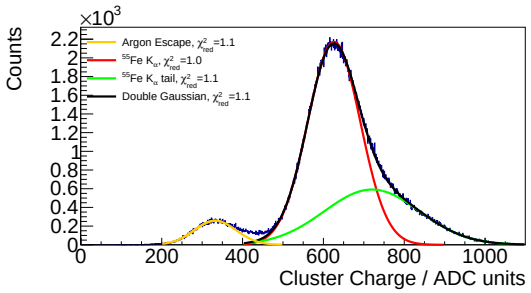

(f) $U_A = 1720\,\mathrm{V}$, max ADC + 4 adjacent samples as pad charge

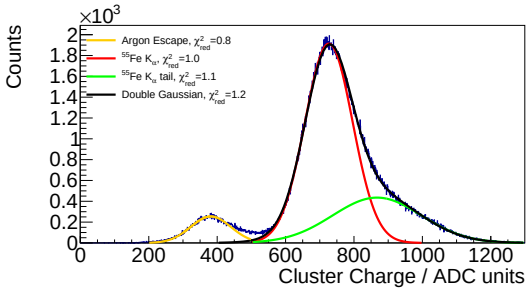

(g) $U_A = 1740\,\mathrm{V}$, max ADC + 4 adjacent samples as pad charge

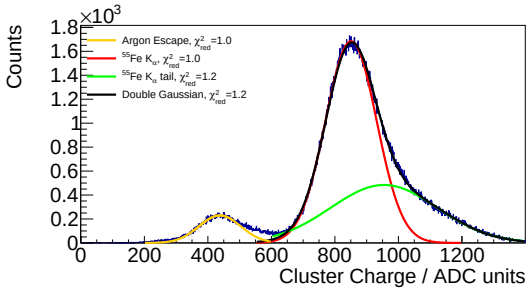

(h) $U_A = 1760\,\mathrm{V}$, max ADC + 4 adjacent samples as pad charge

Figure A.11.: Presented are ^{55}Fe spectra at different anode voltages. The three pad cluster charge is the sum of the pad charge while the pad charge is calculated as explained below the spectra. The fit results can be found in tables A.2 to A.9

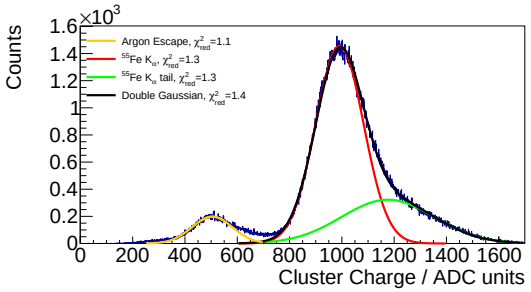

(a) $U_A = 1780\,\mathrm{V}$, max ADC + 4 adjacent samples as pad charge

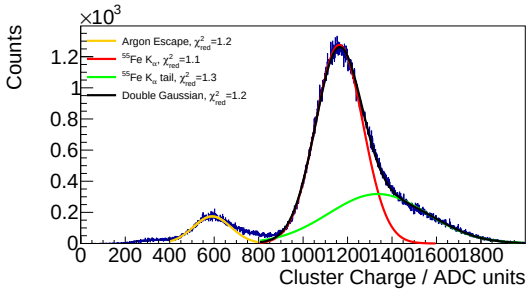

(b) $U_A = 1800\,\mathrm{V}$, max ADC + 4 adjacent samples as pad charge

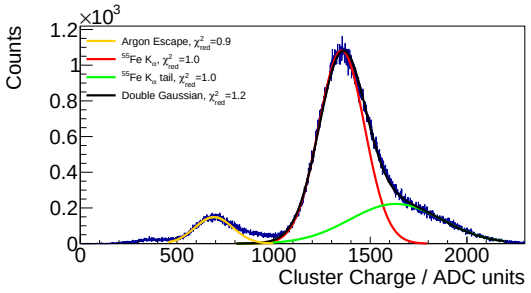

(c) $U_A = 1820\,\mathrm{V}$, max ADC + 4 adjacent samples as pad charge

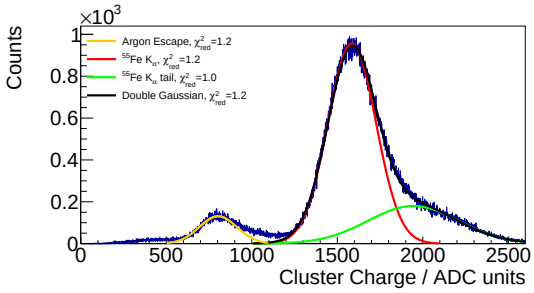

(d) $U_A = 1840\,\mathrm{V}$, max ADC + 4 adjacent samples as pad charge

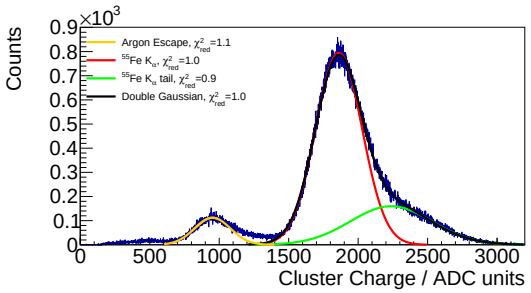

(e) $U_A = 1860\,\mathrm{V}$, max ADC + 4 adjacent samples as pad charge

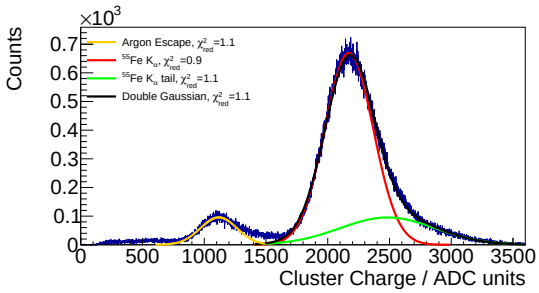

(f) $U_A = 1880\,\mathrm{V}$, max ADC + 4 adjacent samples as pad charge

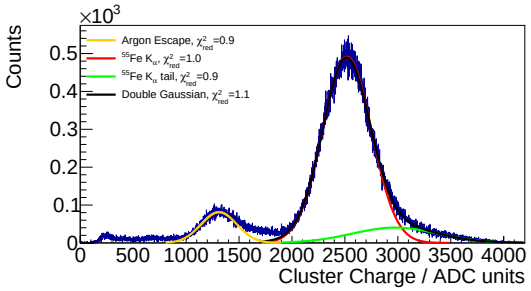

(g) $U_A = 1900\,\mathrm{V}$, max ADC + 4 adjacent samples as pad charge

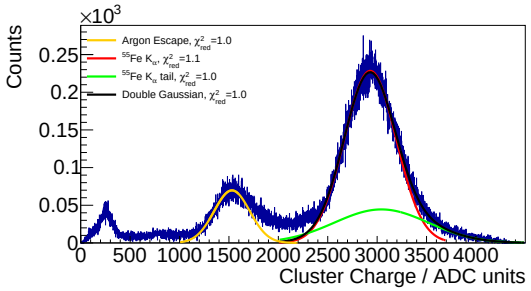

(h) $U_A = 1920\,\mathrm{V}$, max ADC + 4 adjacent samples as pad charge

Figure A.12.: Presented are ^{55}Fe spectra at different anode voltages. The three pad cluster charge is the sum of the pad charge while the pad charge is calculated as explained below the spectra. The fit results can be found in tables A.2 to A.9

Table A.2.: This list contains the fit results and energy resolutions of the spectra reconstructed with the integrated pad charge.

	Ar escape		^{55}Fe K_α		^{55}Fe K_α tail	
U_A [V]	μ	σ	μ	σ	μ	σ
1700	819.22 ± 11.65	152.67 ± 5.77	1482.55 ± 0.70	209.68 ± 0.73	1867.60 ± 11.64	353.29 ± 4.26
1720	897.97 ± 7.36	155.87 ± 3.48	1708.27 ± 0.92	221.57 ± 0.90	2246.30 ± 9.08	375.17 ± 3.64
1740	1064.07 ± 3.08	201.52 ± 2.00	1973.40 ± 1.66	231.09 ± 1.56	2672.38 ± 9.84	414.43 ± 4.14
1760	1220.56 ± 5.72	229.32 ± 3.60	2303.58 ± 1.27	260.08 ± 1.12	3005.91 ± 10.24	504.25 ± 4.49
1780	1388.42 ± 6.51	249.05 ± 5.93	2682.20 ± 0.97	294.48 ± 0.95	3522.97 ± 13.56	603.99 ± 6.56
1800	1601.63 ± 8.28	263.27 ± 7.36	3121.43 ± 1.32	320.35 ± 1.23	4348.05 ± 10.80	613.00 ± 5.54
1820	1878.84 ± 13.54	337.00 ± 24.75	3641.80 ± 1.38	366.58 ± 1.27	5145.00 ± 13.00	683.94 ± 6.57
1840	2174.78 ± 6.15	338.35 ± 10.16	4262.42 ± 1.21	428.45 ± 1.21	6090.71 ± 75.17	757.68 ± 26.27
1860	2570.33 ± 10.40	432.15 ± 21.71	4970.88 ± 2.09	486.72 ± 2.41	6993.54 ± 26.89	852.51 ± 13.36
1880	2984.36 ± 11.70	431.45 ± 16.35	5776.18 ± 3.42	553.36 ± 2.40	7731.42 ± 51.09	1115.74 ± 20.26
1900	3503.42 ± 19.19	510.82 ± 28.62	6673.82 ± 11.84	621.04 ± 7.01	8874.29 ± 73.99	1297.20 ± 33.40
1920	4110.88 ± 10.68	576.07 ± 18.56	7783.87 ± 4.31	742.80 ± 8.07	10482.93 ± 245.63	1067.05 ± 99.46

Table A.3.: This list contains the fit results and energy resolutions of the spectra reconstructed with the integrated pad charge.

	double, ^{55}Fe K_α		double, ^{55}Fe K_α tail		σ/μ [%] ^{55}Fe K_α	σ/μ [%] double, ^{55}Fe K_α
U_A [V]	μ	σ	μ	σ		
1700	1459.43 ± 0.88	197.20 ± 1.04	1887.69 ± 10.31	348.41 ± 3.91	14.14 ± 1.23	13.51 ± 1.20
1720	1693.36 ± 0.89	216.35 ± 0.92	2226.97 ± 8.58	383.21 ± 3.45	12.97 ± 0.98	12.78 ± 0.97
1740	1970.52 ± 0.88	237.26 ± 1.05	2601.55 ± 8.86	441.00 ± 3.71	11.71 ± 0.77	12.04 ± 0.79
1760	2295.36 ± 0.88	259.39 ± 1.03	2982.07 ± 10.39	514.10 ± 4.43	11.29 ± 0.64	11.30 ± 0.64
1780	2669.40 ± 0.87	288.77 ± 1.19	3448.35 ± 13.01	634.08 ± 6.03	10.98 ± 0.53	10.82 ± 0.52
1800	3124.10 ± 1.01	330.72 ± 1.16	4132.82 ± 11.95	704.01 ± 5.66	10.26 ± 0.43	10.59 ± 0.44
1820	3644.23 ± 1.13	377.31 ± 1.23	4841.56 ± 12.66	813.29 ± 6.11	10.07 ± 0.36	10.35 ± 0.37
1840	4251.56 ± 1.23	428.45 ± 1.40	5648.91 ± 14.90	966.43 ± 7.66	10.05 ± 0.31	10.08 ± 0.31
1860	4964.71 ± 1.58	499.46 ± 2.11	6483.80 ± 21.14	1082.32 ± 10.84	9.79 ± 0.26	10.06 ± 0.27
1880	5801.62 ± 1.52	564.83 ± 2.11	6985.94 ± 25.54	1323.66 ± 9.52	9.58 ± 0.22	9.74 ± 0.22
1900	6701.93 ± 1.86	631.65 ± 2.86	7783.65 ± 63.50	1644.00 ± 23.44	9.31 ± 0.22	9.42 ± 0.19
1920	7764.61 ± 6.32	736.40 ± 9.66	8629.05 ± 237.44	1657.39 ± 75.77	9.54 ± 0.19	9.48 ± 0.21

Table A.4.: This list contains the fit results and energy resolutions of the spectra reconstructed with the maximum ADC value taken as pad charge.

	Ar escape		^{55}Fe K_α		^{55}Fe K_α tail	
U_A[V]	μ	σ	μ	σ	μ	σ
1700	68.79 ± 0.22	10.47 ± 0.49	118.87 ± 0.08	12.05 ± 0.08	124.21 ± 3.17	24.05 ± 0.82
1720	75.57 ± 0.29	10.78 ± 0.28	136.75 ± 0.13	13.15 ± 0.08	146.52 ± 1.48	27.43 ± 0.44
1740	85.51 ± 0.36	12.00 ± 0.38	158.76 ± 0.07	14.72 ± 0.06	178.24 ± 1.53	29.68 ± 0.48
1760	98.09 ± 0.74	14.11 ± 0.66	185.09 ± 0.07	17.11 ± 0.06	199.80 ± 3.31	36.56 ± 0.89
1780	111.31 ± 0.31	14.82 ± 0.75	214.54 ± 0.08	19.36 ± 0.06	232.67 ± 1.66	43.02 ± 0.53
1800	129.88 ± 0.36	17.33 ± 0.51	249.68 ± 0.15	21.55 ± 0.12	292.30 ± 1.47	43.97 ± 0.53
1820	151.10 ± 0.53	20.45 ± 0.49	291.08 ± 0.12	25.15 ± 0.10	347.00 ± 2.07	49.39 ± 0.74
1840	174.96 ± 0.37	22.10 ± 0.39	339.14 ± 0.15	29.36 ± 0.15	406.96 ± 1.50	56.63 ± 0.57
1860	206.07 ± 0.72	28.30 ± 1.32	397.56 ± 0.13	34.62 ± 0.11	466.08 ± 3.18	63.86 ± 1.13
1880	240.00 ± 0.50	27.42 ± 1.27	463.79 ± 0.17	41.53 ± 0.15	508.50 ± 17.78	86.57 ± 4.43
1900	281.96 ± 0.91	35.87 ± 1.22	536.61 ± 0.38	48.69 ± 0.28	646.36 ± 9.25	78.93 ± 2.99
1920	329.17 ± 1.05	40.31 ± 2.69	622.29 ± 0.44	54.08 ± 0.49	781.96 ± 7.34	51.62 ± 2.73

Table A.5.: This list contains the fit results and energy resolutions of the spectra reconstructed with the maximum ADC value taken as pad charge.

	double, ^{55}Fe K_α		double, ^{55}Fe K_α tail		σ/μ [%] ^{55}Fe K_α	σ/μ [%] double, ^{55}Fe K_α
U_A [V]	μ	σ	μ	σ		
1700	117.86 ± 0.06	11.02 ± 0.11	132.40 ± 0.78	21.70 ± 0.24	10.14 ± 0.69	9.35 ± 0.65
1720	136.07 ± 0.05	12.42 ± 0.08	155.76 ± 0.58	24.58 ± 0.18	9.62 ± 0.58	9.13 ± 0.54
1740	157.80 ± 0.05	13.89 ± 0.09	181.85 ± 0.68	28.34 ± 0.23	9.27 ± 0.47	8.80 ± 0.45
1760	183.76 ± 0.06	15.97 ± 0.09	211.72 ± 0.68	32.69 ± 0.23	9.24 ± 0.40	8.69 ± 0.38
1780	213.60 ± 0.06	18.59 ± 0.09	249.11 ± 0.70	37.65 ± 0.25	9.02 ± 0.34	8.70 ± 0.33
1800	249.17 ± 0.07	21.29 ± 0.11	292.28 ± 1.12	43.85 ± 0.40	8.63 ± 0.29	8.54 ± 0.28
1820	290.25 ± 0.08	24.73 ± 0.11	343.47 ± 1.15	50.29 ± 0.44	8.64 ± 0.24	8.52 ± 0.24
1840	338.11 ± 0.10	29.33 ± 0.14	404.05 ± 1.43	57.65 ± 0.53	8.66 ± 0.21	8.68 ± 0.21
1860	395.10 ± 0.11	33.13 ± 0.17	462.63 ± 1.55	64.52 ± 0.58	8.71 ± 0.18	8.39 ± 0.18
1880	463.05 ± 0.13	41.11 ± 0.18	525.70 ± 2.24	79.04 ± 0.72	8.95 ± 0.16	8.88 ± 0.16
1900	533.70 ± 0.13	46.58 ± 0.28	610.05 ± 6.40	89.43 ± 2.01	9.07 ± 0.22	8.73 ± 0.21
1920	621.08 ± 0.61	54.30 ± 0.47	735.00 ± 7.93	67.75 ± 2.61	8.69 ± 0.19	8.74 ± 0.19

Table A.6.: This list contains the fit results and energy resolutions of the spectra reconstructed with the the three maximum ADC value samples taken as pad charge.

	Ar escape		^{55}Fe K_α		^{55}Fe K_α tail	
U_A [V]	μ	σ	μ	σ	μ	σ
1700	190.50 ± 0.98	28.87 ± 0.74	340.41 ± 0.23	35.52 ± 0.21	353.65 ± 4.78	72.62 ± 1.35
1720	211.85 ± 1.17	31.41 ± 0.88	394.57 ± 0.23	39.57 ± 0.28	442.51 ± 4.13	75.46 ± 1.28
1740	241.04 ± 0.80	35.10 ± 1.11	459.62 ± 0.17	44.22 ± 0.15	537.18 ± 5.21	81.24 ± 1.61
1760	277.36 ± 0.85	39.59 ± 1.62	538.59 ± 0.15	51.94 ± 0.14	621.15 ± 7.49	96.07 ± 2.34
1780	321.73 ± 1.21	49.06 ± 0.84	623.71 ± 0.25	57.02 ± 0.20	723.08 ± 5.96	113.94 ± 1.89
1800	372.62 ± 1.16	51.08 ± 1.26	728.94 ± 0.37	64.70 ± 0.30	857.71 ± 4.55	129.00 ± 1.80
1820	433.70 ± 2.29	58.48 ± 2.02	849.48 ± 0.40	74.00 ± 0.32	1004.53 ± 5.19	150.07 ± 2.08
1840	505.89 ± 1.39	71.27 ± 3.48	996.81 ± 0.27	89.21 ± 0.24	1233.67 ± 6.84	154.61 ± 2.48
1860	599.28 ± 1.59	81.64 ± 2.20	1164.07 ± 0.46	103.33 ± 0.52	1383.74 ± 10.16	183.92 ± 3.33
1880	700.37 ± 2.15	90.90 ± 3.22	1362.89 ± 0.40	124.61 ± 0.37	1492.27 ± 53.00	253.28 ± 13.74
1900	823.41 ± 5.18	106.14 ± 5.57	1574.07 ± 0.63	142.91 ± 0.57	1841.03 ± 27.25	250.98 ± 9.18
1920	959.06 ± 4.03	113.98 ± 3.94	1830.28 ± 2.23	161.68 ± 2.22	2103.15 ± 66.23	225.65 ± 20.904

Table A.7.: This list contains the fit results and energy resolutions of the spectra reconstructed with the the three maximum ADC value samples taken as pad charge.

	double, ^{55}Fe K_α		double, ^{55}Fe K_α tail			σ/μ [%] double, ^{55}Fe K_α
U_A [V]	μ	σ	μ	σ	σ/μ [%] ^{55}Fe K_α	
1700	337.64 ± 0.16	32.72 ± 0.29	382.32 ± 1.96	64.34 ± 0.60	10.43 ± 0.38	9.69 ± 0.36
1720	391.44 ± 0.16	36.86 ± 0.36	445.84 ± 2.93	74.40 ± 0.93	10.03 ± 0.32	9.42 ± 0.31
1740	455.87 ± 0.13	41.55 ± 0.26	532.30 ± 2.17	82.30 ± 0.74	9.62 ± 0.26	9.11 ± 0.25
1760	532.73 ± 0.16	47.59 ± 0.27	620.71 ± 2.22	94.93 ± 0.79	9.64 ± 0.22	8.93 ± 0.21
1780	620.90 ± 0.18	55.04 ± 0.26	728.34 ± 2.25	110.81 ± 0.80	9.14 ± 0.18	8.86 ± 0.18
1800	726.42 ± 0.21	63.57 ± 0.32	862.81 ± 3.29	126.93 ± 1.30	8.88 ± 0.16	8.75 ± 0.15
1820	847.88 ± 0.24	73.64 ± 0.35	1010.25 ± 3.65	147.67 ± 1.47	8.71 ± 0.13	8.68 ± 0.13
1840	989.97 ± 0.28	85.43 ± 0.35	1187.41 ± 3.56	169.49 ± 1.39	8.95 ± 0.11	8.63 ± 0.11
1860	1156.83 ± 0.35	99.85 ± 0.58	1358.91 ± 5.81	191.81 ± 2.09	8.88 ± 0.11	8.63 ± 0.11
1880	1358.01 ± 0.38	121.50 ± 0.53	1550.03 ± 6.50	230.27 ± 2.10	9.14 ± 0.09	8.95 ± 0.09
1900	1567.29 ± 0.43	137.46 ± 0.94	1780.80 ± 21.49	269.20 ± 6.81	9.08 ± 0.08	8.77 ± 0.09
1920	1820.65 ± 0.97	157.25 ± 2.46	2034.41 ± 56.26	248.66 ± 16.22	8.83 ± 0.14	8.64 ± 0.15

Table A.8.: This list contains the fit results and energy resolutions of the spectra reconstructed with the the five maximum ADC value samples taken as pad charge.

	Ar escape		^{55}Fe K_α		^{55}Fe K_α tail	
U_A [V]	μ	σ	μ	σ	μ	σ
1700	297.38 ± 1.28	47.34 ± 1.14	539.02 ± 0.30	58.60 ± 0.27	568.14 ± 9.78	116.93 ± 2.58
1720	332.40 ± 1.70	51.70 ± 1.41	626.25 ± 0.28	65.11 ± 0.25	720.13 ± 6.11	117.89 ± 1.97
1740	381.19 ± 2.07	58.61 ± 1.95	726.42 ± 0.68	69.73 ± 0.50	867.37 ± 6.82	129.81 ± 2.23
1760	437.77 ± 1.19	65.56 ± 1.49	851.02 ± 0.48	80.40 ± 0.40	954.56 ± 7.90	167.91 ± 2.80
1780	504.52 ± 1.65	77.42 ± 4.61	991.30 ± 0.52	91.66 ± 0.40	1176.01 ± 6.65	177.00 ± 2.41
1800	590.62 ± 1.43	84.78 ± 2.46	1162.75 ± 0.47	106.20 ± 0.41	1336.14 ± 6.02	221.41 ± 2.27
1820	691.23 ± 2.04	98.09 ± 4.03	1352.17 ± 0.97	118.54 ± 0.65	1631.94 ± 9.29	238.09 ± 3.95
1840	803.50 ± 3.68	109.85 ± 6.02	1585.79 ± 0.63	140.21 ± 0.53	1944.68 ± 9.17	265.35 ± 3.98
1860	951.85 ± 4.48	128.61 ± 5.29	1860.78 ± 0.75	167.57 ± 0.87	2237.46 ± 15.04	294.41 ± 5.14
1880	1117.11 ± 3.45	147.81 ± 8.32	2172.23 ± 1.13	195.80 ± 0.95	2484.71 ± 82.87	385.75 ± 23.39
1900	1310.70 ± 4.10	168.55 ± 5.17	2519.79 ± 1.18	230.44 ± 1.11	2975.55 ± 73.24	407.14 ± 23.64
1920	1530.58 ± 6.41	180.07 ± 6.98	2930.01 ± 2.40	262.08 ± 3.27	3042.86 ± 334.66	475.29 ± 86.41

Table A.9.: This list contains the fit results and energy resolutions of the spectra reconstructed with the the five maximum ADC value samples taken as pad charge.

	double, ^{55}Fe K_α		double, ^{55}Fe K_α tail		σ/μ [%] ^{55}Fe K_α	σ/μ [%] double, ^{55}Fe K_α
U_A [V]	μ	σ	μ	σ		
1700	533.76 ± 0.24	53.32 ± 0.44	608.09 ± 2.85	105.21 ± 0.87	10.87 ± 0.33	9.99 ± 0.31
1720	620.14 ± 0.21	60.69 ± 0.45	723.03 ± 3.74	116.72 ± 1.23	10.40 ± 0.27	9.79 ± 0.27
1740	723.50 ± 0.22	67.74 ± 0.43	848.12 ± 3.92	135.09 ± 1.34	9.60 ± 0.23	9.36 ± 0.22
1760	846.88 ± 0.27	77.48 ± 0.50	990.45 ± 4.51	155.45 ± 1.65	9.45 ± 0.19	9.15 ± 0.19
1780	988.09 ± 0.30	90.20 ± 0.43	1174.88 ± 4.16	176.40 ± 1.54	9.25 ± 0.16	9.13 ± 0.16
1800	1157.57 ± 0.35	104.12 ± 0.48	1391.24 ± 4.99	203.49 ± 1.93	9.13 ± 0.13	8.99 ± 0.13
1820	1353.15 ± 0.39	119.96 ± 0.55	1624.12 ± 5.90	240.09 ± 2.51	8.77 ± 0.12	8.87 ± 0.11
1840	1581.18 ± 0.45	138.74 ± 0.62	1901.98 ± 6.62	280.41 ± 2.80	8.84 ± 0.10	8.77 ± 0.10
1860	1849.38 ± 0.60	162.77 ± 0.93	2193.15 ± 9.24	309.16 ± 3.42	9.01 ± 0.09	8.80 ± 0.09
1880	2172.18 ± 0.62	196.90 ± 0.96	2476.71 ± 12.66	377.30 ± 4.13	9.01 ± 0.08	9.06 ± 0.08
1900	2508.93 ± 0.82	219.96 ± 1.50	2816.52 ± 32.14	451.38 ± 10.07	9.15 ± 0.08	8.77 ± 0.08
1920	2917.59 ± 2.91	252.72 ± 4.57	3163.06 ± 86.57	442.16 ± 23.28	8.94 ± 0.13	8.66 ± 0.17

Bibliography

[ABBM+04] A. Andronic, S. Biagi, P. Braun-Munzinger, C. Garabatos, and G. Tsiledakis. Drift velocity and gain in argon- and xenon-based mixtures. *arXiv: physics/0402044*, 2004.

[BRR08] W. Blum, W. Riegler, and L. Rolandi. *Particle Detection with Drift Chambers*. Springer-Verlag Berlin Heidelberg, 2 edition, 2008.

[Coled] The CBM Collaboration. *Technical Design Report for the CBM TRD*. The TRD Working Group and the CBM Collaboration, To be published.

[eaP13] J. Beringer et al. (PDG). Passage of Particles through Matter. `http://pdg.lbl.gov/2013/reviews/rpp2013-rev-passage-particles-matter.pdf`, 2013.

[GS08] Claus Grupen and Boris Shwartz. *Particle Detectors*. Cambridge Univsersity Press, 2 edition, 2008.

[KBF+17] M. Kohn, J. Beckhoff, F. Fidorra, C. de J. García Chávez, P. Kähler, C. Klein-Bösing, M. Kohn, A. Meyer-Ahrens, and P. Munkes. Analysis of the SPADIC multi-hit feature. *CBM Progress Report*, 2017.

[Kle05] Konrad Kleinknecht. *Detektoren für Teilchenstrahlung*. B. G. Teubner Verlag, 4 edition, 2005.

[KW16] Hermann Kolanoski and Norbert Wermes. *Teilchendetektoren, Grundlagen und Anwendungen*. Springer-Verlag Berlin Heidelberg, 2016.

[Leo87] William R. Leo. *Techniques for Nuclear and Particle Physics Experiments*. Springer-Verlag Berlin Heidelberg, 1987.

[MA16] Adrian Meyer-Ahrens. Auslese eines Szintillationszählers mit selbstgetriggerter Elektronik. Bachelor thesis, 2016. IKP, WWU Münster.

[Mat] E. Mathieson. *Induced charge distribution in proportional detectors*.

[MBF+17] P. Munkes, J. Beckhoff, F. Fidorra, C. de J. García Chávez, P. Kähler, C. Klein-Bösing, M. Kohn, and A. Meyer-Ahrens. A new in-beam-test data analysis framework for the CBM-TRD. *CBM Progress Report*, 2017.

[MMB06] V. Chisté M. M. Bé. 55 fe. http://www.nucleide.org/DDEP_WG/Nuclides/Fe-55_tables.pdf, 2006. visited 8.30.2016.

[Mun16] Philipp Munkes. Ereignis-Rekonstruktion für CBM-TRD Testdaten. Bachelor thesis, 2016. IKP, WWU Münster.

[Sau14] Fabio Sauli. *Gaseous Radiation Detectors, Fundamentals and applications*. Cambridge University Press, 2014.

[Sch05] Michael Schmid. Schematic view of a very simple wire chamber. `https://commons.wikimedia.org/wiki/File:Wire_chamber_schematic.svg`, 2005.

[Sch08] Harvard Medival School. X-ray emission lines. `http://www.med.harvard.edu/jpnm/physics/refs/xrayemis.html`, 2008. visited 8.22.2018.

[Sim12] Doug Sim. Detector Regions. `https://commons.wikimedia.org/wiki/File:Detector_regions.gif`, 2012.

[spa14] SPADIC 1.0 Data Sheet. Data sheet, 2014.

[Svj15] Svjo-2. Geiger Muller counter. A detector of radiation levels. `https://commons.wikimedia.org/wiki/File:Geiger-Muller-counter-en.png`, 2015.

[Wes15] Johannes Wessels. Kern- und Teilchenphysik 1. lecture notes, 2014/2015. WWU Münster.

[zN06] Martin zur Nedden. Detektoren in der Elementarteilchenphysik. lecture notes, `http://www-hera-b.desy.de/people/nedden/lectures/05_06/dettph/`, 2006. Humboldt-Universität zu Berlin, Institut für Physik.

List of Figures

List of Tables

Glossary

ADC	Analog Digital Converter (also used as unit)
AFCK	AMC FMC Carrier Kintex
AMC	Advanced Mezzanine Card
CBM	Compressed Baryonic Matter
CRI	Common Readout Interface
CSA	Charge Sensitive Amplifier
DAQ	Data AcQuisition
DPB	Data Processing Board
QCD	Quantum ChromoDynamics
FAIR	Facility for Antiproton and Ion Research
FEB	Front-End Board
FEE	Front-End Electronics
FIFO	First In First Out
FLES	First Level Event Selection
FLIB	FLES Interface Board
FMC	FPGA Mezzanine Card
FNR	Forced Neighbor Readout
FPGA	Free Programmable Gate Array
MIP	Minimum Ionizing Particles
MWPC	Multi Wire Propoortional Chamber
NOS	Number Of Samples
PRF	Pad Response Function
ROB	Read Out Board
SPADIC	Self-Triggered Pulse Amplification and Digitization ASIC
STR	Self Triggered
TRD	Transition Radiation Detector

Acknowledgments

First of all, I would like to thank Prof. Dr. Anton Andronic and PD Dr. Christian Klein-Bösing. They enabled my work on this topic, created a very comfortable working atmosphere and guided me through a lot of questions for over one year.

Most of all, my mentors Philipp Kähler and Martin Kohn supported me whenever they could. They answered each and every arising question and gave a lot of input on many analyses, enabling the completion of this work. Thank you!

In addition, I would like to say thank you to my working group, which never had a place for boredom.

In the end, I owe my family, especially my sister Frederike, their huge support during my whole studies, giving me the opportunity to enjoy five wonderful years in Münster. My friend Johannes accompanied me over those years, making them even more enjoyable. I will miss you, buddy.

Originality Statement

I hereby certify that I am the sole author of this thesis and that no part of this thesis has been published or submitted for publication.

I certify that, to the best of my knowledge, my thesis does not infringe upon anyones copyright nor violate and proprietary rights and that any ideas, techniques, quotations, or any other material from the work of other people included in my thesis, published or otherwise, are fully acknowledged in accordance with the standard referencing practices.

Münster, August 22, 2018

.....
(Johannes Beckhoff)